

Acta Universitatis  
Lappeenrantaensis  
817



Vesa-Ville Hurskainen

**DYNAMIC ANALYSIS OF FLEXIBLE MULTIBODY  
SYSTEMS USING FINITE ELEMENTS  
BASED ON THE ABSOLUTE NODAL  
COORDINATE FORMULATION**

---



Vesa-Ville Hurskainen

**DYNAMIC ANALYSIS OF FLEXIBLE MULTIBODY  
SYSTEMS USING FINITE ELEMENTS  
BASED ON THE ABSOLUTE NODAL  
COORDINATE FORMULATION**

Thesis for the degree of Doctor of Science (Technology) to be presented with due permission for public examination and criticism in the Auditorium 2303 at Lappeenranta University of Technology, Lappeenranta, Finland on the 19<sup>th</sup> of October, 2018, at noon.

Acta Universitatis  
Lappeenrantaensis 817

- Supervisors Professor Aki Mikkola, D.Sc. (Tech.)  
School of Energy Systems  
Lappeenranta University of Technology  
Finland
- Academy Research Fellow Marko Matikainen, D.Sc. (Tech.)  
School of Energy Systems  
Lappeenranta University of Technology  
Finland
- Reviewers Professor Robert Seifried, Dr.-Ing.  
Institute of Mechanics and Ocean Engineering  
Hamburg University of Technology  
Germany
- Univ.-Prof. Johannes Gerstmayr, Dr.  
Department of Mechatronics  
University of Innsbruck  
Austria
- Opponents Professor Robert Seifried, Dr.-Ing.  
Institute of Mechanics and Ocean Engineering  
Hamburg University of Technology  
Germany
- Senior Scientist Radu Serban, Dr.  
Department of Mechanical Engineering  
University of Wisconsin–Madison  
Wisconsin, USA

ISBN 978-952-335-277-3  
ISBN 978-952-335-278-0 (PDF)  
ISSN-L 1456-4491  
ISSN 1456-4491

Lappeenranta University of Technology  
LUT Yliopistopaino 2018

---

*In memory of my grandmother.*



---

## Abstract

Vesa-Ville Hurskainen

### Dynamic analysis of flexible multibody systems using finite elements based on the absolute nodal coordinate formulation

Lappeenranta, 2018

62 pages

Acta Universitatis Lappeenrantaensis 817

Dissertation. Lappeenranta University of Technology

ISBN 978-952-335-277-3

ISBN 978-952-335-278-0 (PDF)

ISSN-L 1456-4491

ISSN 1456-4491

The computational analysis of mechanical systems has a wide array of applications and is therefore essential in many fields of modern industry. This dissertation studies the simulation of mechanical systems using the multibody dynamics approach. Focus is placed on the modeling of flexible bodies using finite elements based on the absolute nodal coordinate formulation (ANCF), the advantages of which are investigated in detail.

The objective of this study is to develop finite elements based on the absolute nodal coordinate formulation and apply them to the static and dynamic simulation of various structures. In the included publications, several ANCF-based beam and plate elements are developed and numerically tested, many of which belong to the category of higher-order elements. These elements provide a way to avoid locking issues via accurate modeling of deformation.

The articles included in the dissertation provide several contributions to the study of ANCF-based finite elements as well as their application to the simulation of mechanical systems. The information thus provided is useful for further research in the field and for computational applications of the elements developed.

Keywords: flexible multibody dynamics, nonlinear finite element methods, absolute nodal coordinate formulation



---

## Acknowledgements

I started the research that led to this thesis in autumn of 2015. In the three years that have passed since then, I've very much enjoyed working in the Laboratory of Machine Design. Although the studies and publications have caused stress at times, as these things always do, it never became unbearable. For this, I owe thanks to everyone involved.

Firstly, I would like to thank my supervisors Aki Mikkola and Marko Matikainen for their guidance during my studies. It's in large part thanks to their efforts that I managed to finish my thesis in such short order. I didn't even believe them when they told me I should finish it up by 2018, and yet here we are.

For their efforts in reviewing this dissertation, I would like to thank Prof. Seifried and Prof. Gerstmayr. Their comments helped greatly in improving the work. I'd also like to extend my thanks to all of my coworkers at the lab for their help and for their contributions into making such a welcoming work environment. I wish you all success in your future endeavors, and I wish we'll see each other from now on as well.

Last, but not least, I would like to thank my parents, grandparents and brother. Even though it might've been difficult to find the time to visit sometimes, your support played a large part in making this possible. Thank you.

Lappeenranta, October 2018

*Vesa-Ville Hurskainen*



<b>1</b>	<b>Introduction</b>	<b>19</b>
1.1	Motivation for the study . . . . .	19
1.2	Multibody dynamics . . . . .	21
1.2.1	Finite element method . . . . .	21
1.2.2	Flexibility in multibody systems . . . . .	23
1.2.3	Dynamic analysis . . . . .	24
1.2.4	Nonlinear phenomena . . . . .	28
1.3	Objective and scope of the dissertation . . . . .	30
1.4	Scientific contribution of the study . . . . .	31
<b>2</b>	<b>The absolute nodal coordinate formulation</b>	<b>33</b>
2.1	Beam element kinematics . . . . .	34
2.2	Higher order element kinematics . . . . .	36
2.3	Equations of motion . . . . .	38
2.4	Formulation of elastic forces . . . . .	39
2.4.1	Continuum mechanics formulation . . . . .	40
2.4.2	Structural mechanics formulation . . . . .	41
<b>3</b>	<b>Summary of the findings</b>	<b>43</b>
<b>4</b>	<b>Conclusions</b>	<b>55</b>
	<b>Bibliography</b>	<b>59</b>



---

LIST OF PUBLICATIONS

---

This dissertation includes a total of five publications. Four of these publications are refereed internationally-published journal articles, while the fifth is an international conference article. The articles are presented below in publication order.

*Publication I*

Hurskainen, V.-V., Matikainen, M.K., Wang, J., Mikkola, A. "A Planar Beam Finite-Element Formulation With Individually Interpolated Shear Deformation." *Journal of Computational and Nonlinear Dynamics*, 12(4), January 2017.

*Publication II*

Ebel, H., Matikainen, M.K., Hurskainen, V.-V., Mikkola, A. "Higher-order beam elements based on the absolute nodal coordinate formulation for three-dimensional elasticity." *Nonlinear Dynamics*, 88(2), April 2017.

*Publication III*

Ebel, H., Matikainen, M.K., Hurskainen, V.-V., Mikkola, A. "Analysis of high-order quadrilateral plate elements based on the absolute nodal coordinate formulation for three-dimensional elasticity." *Advances in Mechanical Engineering*, 9(6), June 2017.

*Publication IV*

Wang, J., Hurskainen, V.-V., Matikainen, M.K., Sopanen, J., Mikkola, A. "On the dynamic analysis of rotating shafts using nonlinear superelement and absolute nodal coordinate formulations." *Advances in Mechanical Engineering*, 9(11), November 2017.

*Publication V*

Hurskainen, V.-V., Bozorgmehri, B., Matikainen, M.K., Mikkola, A. "Dynamic Analysis of High-Speed Rotating Shafts Using the Flexible Multibody Approach." *Proceedings of the ASME 2018 International Design Engineering Technical Conferences & Computers and Information in Engineering Conference*, August 26-29, 2018, Quebec City, Canada.

This section details the contribution of the author in the writing of the included articles. The dissertation and the articles were written under the supervision of Professor Aki Mikkola and Dr. Marko Matikainen at Lappeenranta University of Technology.

*Publication I*

The author was designated as the lead author, and as such was responsible for most of the writing and formatting of the paper. The main part of the work on the element formulation and the numerical tests were done by the author. The co-authors provided guidance and assistance in the writing and editing of the article as well as the construction of the test code and the comparison of the results.

*Publication II*

The author was designated as the second co-author and was responsible for computing reference results for the numerical tests – especially the test based on the Princeton beam experiment. In addition to these tasks, the author provided assistance in the writing and proofreading of the paper as well as the production of the included figures.

*Publication III*

The author was designated as the second co-author. Again, the author was responsible for computing reference results for the numerical tests, especially the test based on the Princeton beam experiment and the time-domain dynamic test. Similarly to the previous paper, the author also provided assistance in the writing and proofreading and the production of the figures.

*Publication IV*

The author was designated as the first co-author and was responsible for the computation of dynamical results using ANCF-based elements as well as for developing the procedure to construct Campbell diagrams using ANCF elements. The author was also largely in charge of the formatting, proofreading and revision of the paper.

*Publication V*

The author was designated as the lead author of the paper and was in charge of the time-domain dynamic computations using higher-order ANCF-based elements. The author was also largely in charge of the final formatting and proofreading of the paper.

---

SYMBOLS AND ABBREVIATIONS

---

ALPHABETICAL SYMBOLS

$\mathbf{A}_e$	Rotation matrix describing the cross-sectional reference frame
$A$	Cross-sectional area
$a_i$	$i$ th polynomial coefficient of 1st interpolation polynomial
$\mathbf{b}$	Vector of body forces
$b_i$	$i$ th polynomial coefficient of 2nd interpolation polynomial
$\mathbf{C}$	Damping matrix
$c_i$	$i$ th polynomial coefficient of 3rd interpolation polynomial
$d$	Disk offset
$\mathbf{E}$	Green–Lagrange strain tensor
$E$	Young’s modulus
$E_{ij}$	Element $i, j$ of the Green–Lagrange strain tensor
$\mathbf{e}_i$	$i$ th base vector of the cross-sectional reference frame
$\mathbf{F}$	Deformation tensor
$\mathbf{F}$	Vector of generalized forces
$\mathbf{F}_b$	Vector of generalized body forces
$\mathbf{F}_e$	Vector of generalized elastic forces
$\mathbf{F}_e^{\text{cm}}$	Vector of gener. elastic forces, continuum mechanics formulation
$\mathbf{F}_e^{\text{sm}}$	Vector of gener. elastic forces, structural mechanics formulation
$F$	Loading force
$\mathbf{G}$	Gyroscopic matrix
$G$	Shear modulus
$g$	Gravitational acceleration
$H$	Height
$\mathbf{I}$	Identity matrix/tensor
$\mathcal{I}$	System action functional
$I_1$	Torsional stiffness parameter
$I_2$	1st bending stiffness parameter
$I_3$	2nd bending stiffness parameter
$\mathbf{K}$	Stiffness matrix
$\mathbf{k}$	Vector of twist and curvature
$k_{s2}$	Shear correction factor
$k_{s3}$	Shear correction factor
$\mathcal{L}$	System Lagrangian
$L$	Length
$\mathbf{M}$	Mass matrix
$P$	Polynomial basis of approximation
$P_h$	Polynomial basis of approximation, higher-order element

$p$	Arbitrary point
$\mathbf{q}$	Nodal coordinate vector
$\mathbf{q}^i$	Nodal coordinate vector for node $i$
$\mathbf{r}$	Position vector
$\mathbf{r}_0$	Initial position vector ( $t = 0$ )
$\dot{\mathbf{r}}$	Velocity vector
$\ddot{\mathbf{r}}$	Acceleration vector
$\mathbf{r}^{(i)}$	Position vector of node $i$
$\mathbf{r}_{,j}$	Abbreviated notation: $\mathbf{r}_{,j} = (\partial\mathbf{r})/(\partial j)$ , with $j \in x, y, z$
$\mathbf{r}_{,jk}$	Abbreviated notation: $\mathbf{r}_{,jk} = (\partial^2\mathbf{r})/(\partial j \partial k)$ , with $j, k \in x, y, z$
$\mathbf{S}$	Second Piola–Kirchhoff stress tensor
$\mathbf{S}_m$	Shape function matrix
$\mathbf{s}$	Shear vector
$S_m^i$	The $i$ th shape function of the element
$\mathbf{t}$	Cross-section orientation vector
$t$	Time
$t_1$	First moment of time (beginning)
$t_2$	Second moment of time (ending)
$V$	Volume
$W_e$	System external potential energy
$W_i$	System internal potential energy
$W_i^{asb}$	Internal potential energy: axial, shear and bending strains
$W_i^c$	Internal potential energy: cross-sectional deformation
$W_k$	System total kinetic energy
$W_p$	System total potential energy
$W$	Width
$\mathbf{x}$	Vector of physical coordinates
$x$	1st physical coordinate
$y$	2nd physical coordinate
$z$	3rd physical coordinate

## GREEK SYMBOLS

$\alpha$	Coordinate scaling factor ( $x$ )
$\beta$	Coordinate scaling factor ( $y$ )
$\Gamma_1$	Axial strain
$\Gamma_1$	1st shear strain
$\Gamma_2$	2nd shear strain
$\gamma$	Coordinate scaling factor ( $z$ )
$\varepsilon$	System perturbation
$\zeta$	3rd element coordinate

---

$\eta$	2nd element coordinate
$\boldsymbol{\kappa}$	Vector of torsional and bending strains
$\kappa_1$	Torsional shear strain
$\kappa_2$	1st bending strain
$\kappa_3$	2nd bending strain
$\lambda$	1st Lamé material parameter
$\mu$	2nd Lamé material parameter
$\boldsymbol{\xi}$	Vector of element coordinates
$\xi$	1st element coordinate
$\rho$	Material density
$\phi$	Force angle in the Princeton beam experiment
$\Psi$	Strain energy density function
$\Omega$	Rotational velocity

#### ABBREVIATIONS

2D	Two-dimensional (planar)
3D	Three-dimensional (spatial)
ANCF	Absolute nodal coordinate formulation
CMF	Continuum mechanics formulation
DOF	Degree of freedom
EOM	Equations of motion
FE	Finite-element
FEM	Finite-element method
FFRF	Floating frame of reference formulation
LRVF	Large rotation vector formulation
ODE	Ordinary differential equation
PDE	Partial differential equation
RPM	Revolutions per minute
SMF	Structural mechanics formulation

#### MATHEMATICAL OPERATORS

$\cdot$	Dot product
$:$	Double dot product
$\times$	Cross product
$\nabla$	Gradient
$\det(\ )$	Determinant
$\text{tr}(\ )$	Trace



## Introduction

The computational simulation of systems is essential in many fields of modern industry. In the field of mechanical systems alone, applications of computational simulation range from design tasks (*e.g.* strength calculation, digital prototyping) to operational monitoring (virtual sensors, "digital twins") and operator training (end-user simulators). As such, computational mechanics is consistently an active area of research in mechanical and computational engineering. Improvements in this area can have a significant impact on the way mechanical systems are designed, manufactured and operated in the future.

### 1.1 Motivation for the study

The first step of any computational simulation is the construction of a mathematical model of the system to be simulated. While technological progress continuously enables the solution of more complex mathematical models, it is also important to consider computational efficiency. As a general rule, the simulation model of a system should never be more complex than necessary for results to be produced with a satisfactory degree of accuracy, considering the application.

A long-standing problem related to the accuracy of physical simulations in computational mechanics is the flexibility of bodies. While many different approaches to take flexibility into account have been developed and studied, each of these approaches comes with its own advantages and disadvantages. Common approaches include simplified lumped-parameter (*e.g.* spring-mass type) models as well as various formulations based on the finite element method. Finite elements, in particular, are often employed due to their ability to adapt to a variety of different applications and due to the multitude of commercial finite element software available on the market. There are, however, disadvantages

or "trade-offs" to many conventional finite element based approaches, such as problems in accuracy or computational efficiency when modeling complex systems with nonlinear phenomena. For these reasons, the continual development of alternative approaches such as finite element models based on the absolute nodal coordinate formulation (ANCF) is justified.

Taking nonlinear effects into account may be crucial for the modeling of different types of mechanical systems (see Fig. 1.1). Examples include machines with large inertial forces or deformations during operation and machine elements constructed from materials with pronounced nonlinear behavior. To name an example, in the field of rotating machines an ongoing trend is the development of high-speed machines, which can offer higher efficiencies than traditional designs. High-speed machines employing direct drive mechanisms may also feature simpler constructions than comparable lower-speed systems equipped with gearboxes. However, since the rotational frequencies of these systems can range from ten thousand to several hundred thousand revolutions per minute, these kinds of systems also set high demands on simulation models due to the magnitude of inertial forces involved in their operation.

This work studies the computational analysis of mechanical systems using the multibody dynamics approach. Focus is placed on the modeling of flexible bodies using finite elements based on the absolute nodal coordinate formulation, the advantages of which are investigated in detail. In many of the included publications, higher order ANCF-based elements are examined as a way to accurately model deformations in the context of beam and plate elements.

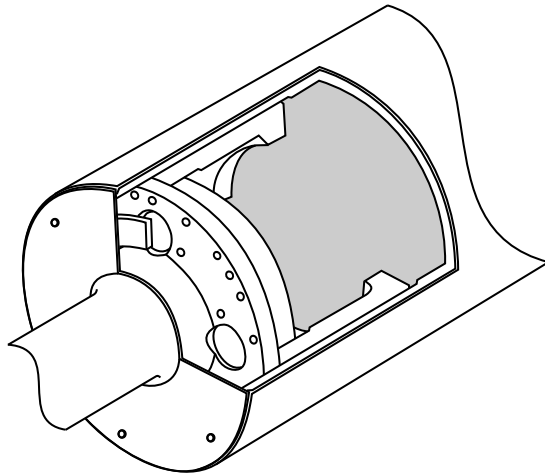


**Figure 1.1.** Motivating example: mechanical system with pronounced nonlinear effects due to rotational inertia. Cutaway drawing of a paper machine roll. Depicted structure property of Valmet Corporation, Finland (<http://www.valmet.com/>).

## 1.2 Multibody dynamics

*Multibody dynamics*, as a term, refers to the study of the dynamic behavior of systems consisting of multiple interconnected bodies undergoing large displacements and/or rotations. The bodies are connected via constraints, such as joints, and are subject to various loads, such as gravitation or contact forces. The computational analysis of such systems, made possible by the continual development of computational tools and computer hardware, has become an important part of machine design. Multibody dynamics can be seen as a comprehensive approach for modeling and analysing the behavior of mechanically complex systems, including *e.g.* the motions, deformations, stresses and vibrational properties of the system. [31]

Multibody models may consist of rigid bodies, flexible bodies, or some combination of both. While systems consisting solely of rigid bodies are (generally speaking) computationally simple and may provide results with an acceptable level of accuracy, they are limited to applications where the deformations of bodies are not significant. In many other cases, the accuracy of simulation can be improved significantly by taking deformations into account for one or more of the bodies in the system. In multibody models, it is also common to employ different flexible formulations for different bodies (depending *e.g.* on the magnitude of their deformations) to achieve an accurate and computationally efficient model. [3]

### 1.2.1 Finite element method

A traditional approach to calculating the deformations of flexible bodies is the use of simple analytical models, such as those constructed following the Euler–Bernoulli or Timoshenko beam theory. However, these beam theories are mainly concerned with lateral deflections of beam-like structures. Therefore, the approach is conceptually simple and has limited applicability to systems with more complex geometries. In such cases, numerical methods must be applied.

Of these numerical methods, the *finite element method* (FE-method, FEM), in particular, is commonly employed today in the analysis of all types of mechanical systems. [2] The method provides a way to transform a complex problem (*e.g.* a system of partial differential equations, PDEs) into one that is simpler to computationally solve (*e.g.* a system of algebraic equations or ordinary differential equations, ODEs) by dividing the structure into smaller subdomains called finite elements. The FEM has a wide variety of applications in engineering, from the modeling of fluid flow and thermal transfer to the modeling of mechanical flexibility. While the FEM is consequently often employed in the modeling of flexibility in multibody systems, some special procedures are usually required to account for the large relative motions that may occur in such applications. [39]

When employing the finite element method for structural modeling, "conventional" spatial (3D) beam, shell and plate finite elements are often employed due to their relative computational simplicity and the fact that they are commonly implemented in commercial finite element software. While these model types are considerably more adaptable than the simplified analytical models, they may still be unable to model complex geometries. To counteract this, many element types are often used in conjunction to model a system with different types of mechanical elements in a computationally efficient manner.

For cases where the geometry to be modeled is too complex, solid finite elements are commonly used. Fig. 1.2 compares a beam-element based and a solid-element based model. These elements are also commonly found in commercial software and can lead to accurate results when appropriately used. Such models can, however, lead to unnecessarily complex mathematical systems with thousands or even millions of variables to be solved. This may lead to severe computational difficulties especially when dynamic behavior is investigated via simulations in the time domain, where these variables have to be solved at each time step of the simulation. For these reasons, less computationally intensive options with the ability to capture complex effects should be investigated.

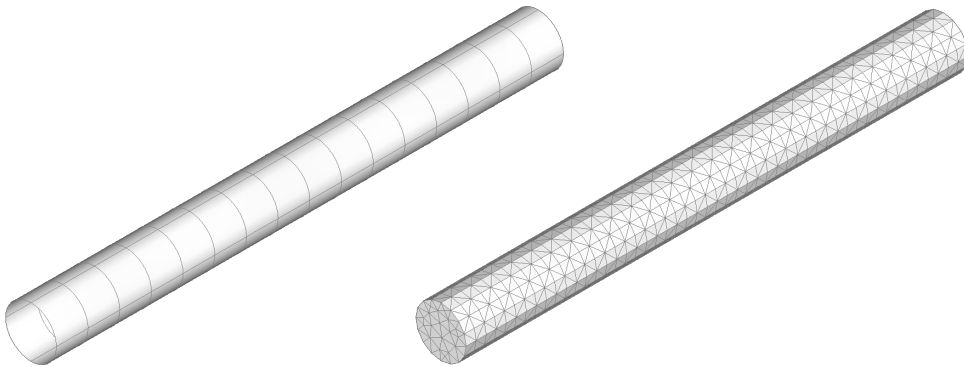


**Figure 1.2.** An example of the finite element modeling of a simple cylindrical shaft. Rough meshes consisting of spatial beam and tetrahedral solid elements.

### 1.2.2 Flexibility in multibody systems

As mentioned above, flexibility in multibody systems is usually modeled using different formulations associated with the finite element method, with some special considerations for taking large displacements and rotations into account. [39] A requirement for use in multibody applications is that when undergoing rigid-body movements, the applied formalism must not exhibit any changes in strain other than those caused by inertial effects. This would lead to problems with strain potential energy in time-domain simulations. Three formulations commonly employed in these applications are the floating frame of reference formulation, the large rotation vector formulation and the absolute nodal coordinate formulation. [30]

The *floating frame of reference formulation* (FFRF) is an often employed finite element based approach, wherein large relative displacements and rotations of a body are described using a moving non-inertial reference frame. [31] The deformations of the finite elements employed to model the flexibility of the body are then described in relation to this reference frame. For example, conventional beam, shell or plate-type finite elements may be employed, although the method is not conceptually limited to them. The chief advantages of the FFRF are the simplicity of the definition of strain energy as well as the ability to reduce the complexity of the model via modal reduction methods, see *e.g.* [9, 41]. However, the definition of kinetic energy may become complex in this approach due to the coupling between the inertial and non-inertial reference frames. In this formulation, inertial force terms as well as the quadratic velocity vector must be separately derived and taken into account in the equations of motion, and the mass matrix of the system is non-constant. In addition, choosing the type of rotational parameters to employ in an FFRF implementation is not trivial due *i.a.* to the possibility of rotational singularities.

The second method mentioned above is the *large rotation vector formulation* (LRVF). [35] Finite elements based on this approach are defined using positions and rotations as the nodal coordinates. LRVF-based elements employ two independent interpolations: one for the position field and a second for the rotation field. This allows them to capture large deformations. Spatial elements based on the LRVF also have a non-constant mass matrices regardless of the choice of rotational parameters, which may make them computationally less than efficient. [23]

The third above-mentioned method is the *absolute nodal coordinate formulation* (ANCF), which is a finite element based formulation developed especially for use in the study of multibody systems. [30] In the ANCF, all generalized coordinates are defined in the global (inertial) reference frame. This fundamental feature leads to several advantages, such as a constant mass matrix and the vanishing of the quadratic velocity vector. [32] In addition, position gradient vectors are used to describe rotations instead of the commonly employed rotation angles, which helps

avoid singularity problems caused by them. These characteristics make the ANCF particularly suitable for multibody applications since they improve the efficiency of computational integrators. Additionally, similarly to solid elements, the ANCF provides a straightforward method to make use of full three-dimensional elasticity in the definition of elastic forces and therefore employ the various material models defined in general continuum mechanics.

Two key issues in the use of ANCF-based elements have previously been identified. The first is that while the description of kinetic energy is simple, the description of elastic forces is highly nonlinear. This stands in contrast to the FFRF and may cause computational issues depending on the application. The other problem is that ANCF-based element formulations employing full three-dimensional elasticity have been known to suffer from locking issues. [37, 29] Here, locking refers to a lowered accuracy or numerical performance in results. Such an effect can be caused *e.g.* by the inability of an element to reproduce the exact deformation shape that a physical structure would have in a particular loading scenario, causing the structure to behave in an unrealistically stiff manner. Several approaches have previously been investigated to avoid these issues. [16, 24]

One of the approaches developed to avoid locking-related problems is the use of higher order derivatives as additional nodal coordinates, enabling the element to reproduce more complex deformation shapes. Elements with an enriched polynomial basis were first introduced by Gerstmayr and Shabana [14], who employed them in the longitudinal direction to avoid shear locking. Consequently, Matikainen et al. [18, 19] employed higher order components in cross-sectional directions for the purpose of improving the description of cross-sectional deformations. In these publications, it was shown that these *higher order* elements help in overcoming the Poisson locking phenomenon. They do, however, introduce more computational complexity into the model by increasing the number of its degrees of freedom. Higher order elements were further investigated in *Publication II* and *Publication III*. The results show that they produce more accurate results in cases where the modeled structure is subject to complex multiaxial loading.

### 1.2.3 Dynamic analysis

When studying the dynamic behavior of a mechanical system, two types of dynamic analyses are commonly considered. The first of these is frequency-domain dynamic analysis, also known as *modal analysis*, while the second is time-domain dynamic analysis, sometimes also known as *transient analysis*. Of these, focus is often placed on modal analysis in the study of systems where the natural frequencies and mode shapes of the system are of special interest, such as rotating systems. On the other hand, time-domain analysis provides a way to study complex transient

(short-term) effects and simulate in detail the behavior of the system in operation, making it important in various applications, such as the design of mobile vehicles.

#### FREQUENCY-DOMAIN ANALYSIS

In frequency-domain analysis, the vibrational properties of the system are investigated. Common problems include determining the natural frequencies and vibrational mode shapes (see Fig. 1.3) of mechanical systems. From a mathematical point of view, frequency-domain problems in mechanics usually consist of systems of algebraic equations, derived from the system's equations of motion, which are solved numerically. It should be noted that modal analysis is a linear analysis type, and therefore, the linearized form of the equations of motion is employed.

The analysis of a system's vibrational properties is often especially crucial in systems with rotating parts. This is due to the fact that any rotational imbalances in a system, impossible to completely avoid in a physical machine, will perpetually

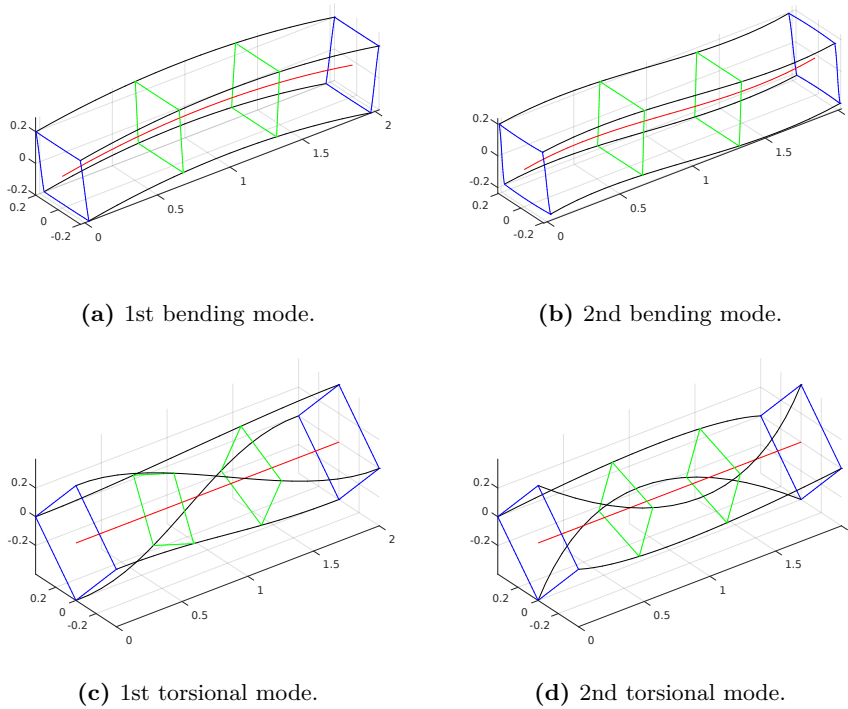


**Figure 1.3.** Examples of deformation mode shapes for a simply supported rectangular beam, modeled using a higher order ANCF-based beam element. First and second bending and torsional deformation modes.

provide an excitation at the current rotational frequency. Consequently, if a natural frequency of the system lies near this excitation frequency, a resonance will occur. This may lead to a variety of undesired effects, possibly even damage to the system. These resonant rotational speeds are called the *critical speeds* of the system, and they should be avoided during operation, if possible. However, the critical speeds are not trivial to determine, since inertial effects cause a shift in the natural frequencies of the system in relation to its rotational speed. [12]

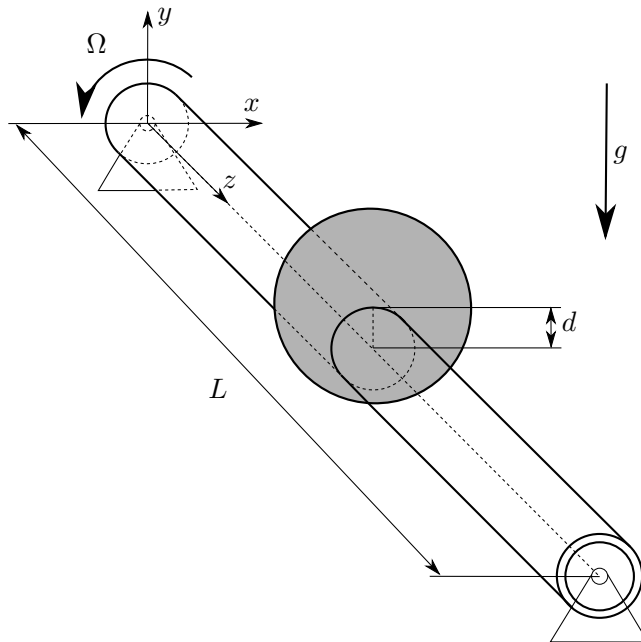
One of the applications of modal analysis in the field of rotordynamics is the *Campbell diagram*, also referred to as the *frequency interference diagram* or *whirl speed map*, which is a commonly employed tool in the analysis of a rotating system's critical speeds. Fig. 1.4 presents an example. The diagram presents the natural frequencies of the system in relation to its rotational speed, making it simple to determine the critical speeds of the system. Graphically, this can be done by drawing a diagonal and finding its intersection points with the natural frequency curves.

Although rotordynamics is commonly concerned only with small displacements, it can be advantageous to construct models that can also take into account large deformations. This permits the use of the same model in multiple types of analysis. Furthermore, the use of formulations which include rotational inertial effects in a straightforward manner can be advantageous. This is expanded upon in the context of the ANCF in *Publication IV*, wherein the construction of Campbell diagrams for ANCF-based models is studied.

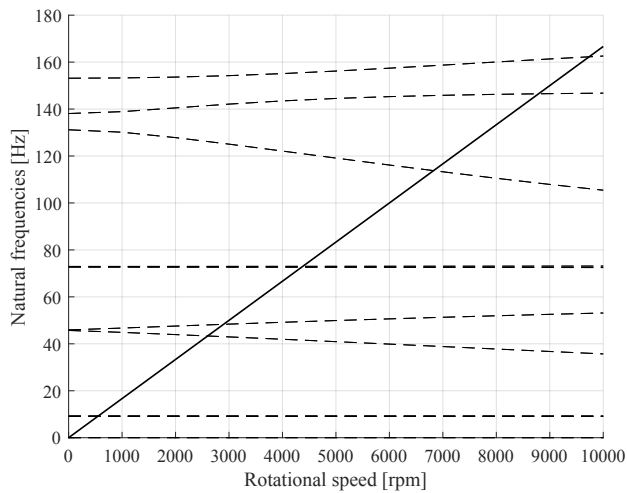
#### TIME-DOMAIN ANALYSIS

When designing mechanical systems, time-domain analysis is useful in predicting complex transient behavior that occurs when the system's operational conditions change. In rotating systems, for example, these scenarios include situations such as running up, shutting down, changing gears or component malfunctions. If the time-domain simulation model is suitably efficient to be run in real-time, in addition to design-phase analysis it may also be employed *e.g.* in simulators. Fig. 1.5 presents an example of a time-domain simulation for an FE model of a simple shaft.

To produce results that correspond to reality with acceptable accuracy, this type of analysis places high requirements on the mathematical models employed to simulate the various components of the system as well as on the numerical methods employed. This is due to the fact that any error produced at each step of the simulation will accumulate over the simulated time span. In addition, the computational complexity of the model is critical especially in real-time applications where a significantly limited amount of computational time is available for determining each time step of the simulation.



(a) A drawing of the system, consisting of a tubular shaft (length  $L$ ) with a rigid disk attached at the middle. The disk is eccentric, with offset  $d$  between disk center and shaft centerline.



(b) Campbell diagram of the system for the speed range  $0 \dots 10000$  RPM. The diagonal line describes the first spin excitation frequency.

**Figure 1.4.** Drawing and Campbell diagram of a rotating shaft with a hollow cross-section and a mass imbalance caused by an eccentric rigid disk.

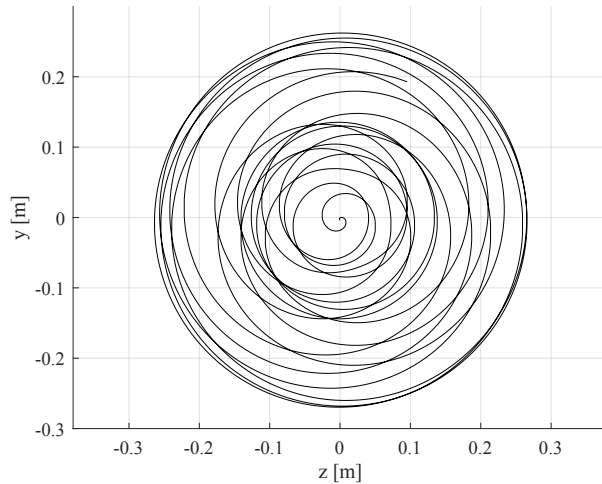


**Figure 1.5.** An example of a time-domain (transient) simulation of a rotating shaft with mass imbalance (see Fig. 1.4). Transverse trajectory of shaft midpoint during running-up, with a total simulation time of 2.5 seconds.

Mathematically speaking, time-domain simulation models commonly consist of systems of ordinary differential equations (ODEs) derived from the system's equations of motion, which need to be numerically solved at each time step to advance the simulation. A large variety of solution algorithms can be found in the literature to accomplish this task. [8] Programmatic implementations of these solution algorithms ("solvers") are also widely available either as parts of commercial software or as separate packages and libraries – some under free license.

#### 1.2.4 Nonlinear phenomena

As previously stated, real-world systems always include a number of nonlinear effects. Taking one or more of these phenomena into account will complicate the model, but may be critical for accuracy when *e.g.* large strains are involved. Such phenomena include material and geometric nonlinearity. [3]

*Material nonlinearity* refers to a nonlinear relationship between the stresses and strains of a body. This type of nonlinearity is present in all real-world materials. However, modeling it is not always required when simulating structures consisting of many "traditional" engineering materials, such as steel, which can be assumed to behave in an ideally linear manner (according to Hooke's

law) in the small deformation regime. When using more complex materials (*e.g.* with pronounced viscoelastic or elasto-plastic behavior) or considering large deformations, nonlinearity of the stress-strain relation should be taken into account. While the modeling of material nonlinearity is therefore certainly important, it is a complex topic and lies outside the scope of this study. Instead, linear elasticity and the hyperelastic Saint Venant–Kirchhoff material law is employed in the included publications. More information about material nonlinearity can be found in the literature, *e.g.* [5].

*Geometric nonlinearity* refers to a nonlinear relationship between displacements and strains. In a geometrically linear analysis, the change in a body’s geometry caused by deformations is ignored, and forces and strains are described in relation to the original undeformed geometry. This is a simplification that may be employed if the strains of the body are assumed to be infinitesimal, which is often sufficiently accurate. Consequently, modeling of geometric nonlinearity is required when the elastic displacements or rotations of the body (or both) are significant, as Fig. 1.6 illustrates. When using continuum mechanics based formulations, whether or not geometric nonlinearity is included in the model is dependent on the choice of strain measure. In the equations in the following chapter, the Green–Lagrange finite strain tensor is employed for this purpose.

An example of a large deformation static case where the modeling of nonlinearity is crucial for accuracy is the Princeton beam experiment, originally conducted physically at Princeton University in the 1970s. [11] This experiment, illustrated in Fig. 1.7, consists of a cantilevered beam attached to a rotating base and loaded at the tip. By altering the angle of the base, a range of nonlinear problems is produced due to the coupling between torsion and bending strains. This problem has been used as a benchmark problem in the literature and is also used to test many of the element formulations in *Publication II* and *Publication III*.

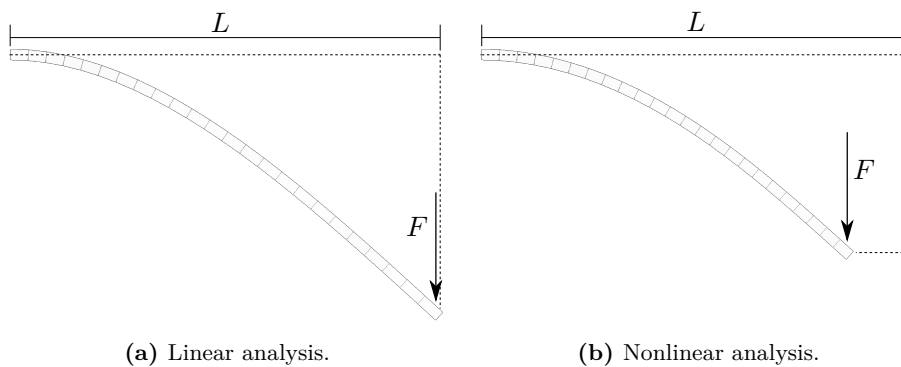


**Figure 1.6.** Simplified illustration of the effect of geometric nonlinearity in a large deformation cantilever beam case with tip load.

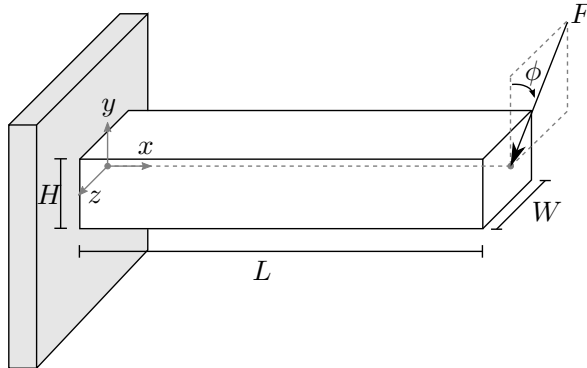


**Figure 1.7.** The Princeton beam experiment: simplified diagram of the experimental setup. In the physical experiment, the force angle  $\phi$  is changed by rotating the structure. [11]

As the numerical results of the Princeton beam experiment presented in *Publication II* and *Publication III* show, in the highest load case the flapwise ( $y$ -directional) displacement of the beam tip grows when the force angle is increased from zero, reaching a peak at  $\phi = 30^\circ$ . This counter-intuitive behavior is nonlinear, and cannot therefore be described using linear theory. The ability of element formulations to reproduce this phenomenon can be used as a criterion to judge their ability to capture nonlinear effects.

### 1.3 Objective and scope of the dissertation

The objective of this study is to develop finite elements based on the absolute nodal coordinate formulation and apply them to the static and dynamic simulation of various structures. This can be divided into two sub-objectives: 1) the development of ANCF-based elements and 2) the applications. Of the included publications, *Publication I*, *Publication II* and *Publication III* chiefly focus on the first objective. They introduce and numerically test element formulations based on the ANCF. On the other hand, *Publication IV* and *Publication V* focus on the second objective. In these publications, previously proposed elements are applied to the simulation of rotating shafts, and the produced results are compared with other formulations.

The dissertation is organized as follows. Chapter 2 presents the theoretical background of the study: the absolute nodal coordinate formulation is clarified by introducing a fully-parameterized ANCF-based beam element and its higher order counterpart. Consequently, the formulations of element equations of motion and elastic forces are presented. Following this, Chapter 3 presents a summary of the findings and conclusions of each publication included in the dissertation. Finally, Chapter 4 presents the conclusions of the study.

## 1.4 Scientific contribution of the study

The articles included in the dissertation provide several contributions to the study of ANCF-based finite elements as well as their application to the simulation of mechanical systems. *Publication I* introduces a novel kind of planar (2D) element formulation based on the ANCF, displaying high accuracy and rates of convergence in comparison to other comparable elements. *Publication II* and *Publication III* analyze several spatial (3D) ANCF-based higher order beam and plate elements with different polynomial bases and make observations on their performance in various numerical tests. This information is useful for further research in the field as well as for computational applications of the elements. *Publication IV* compares the performance of an ANCF-based beam element to that of a nonlinear superelement formulation in a rotating structure application. This verifies the use of the ANCF in rotating applications. The publication also introduces a method of computing Campbell diagrams for ANCF-based models. Finally, *Publication V* applies the higher order beam element to the simulation of a rotating system and makes remarks based on the results of numerical experiments. These results help advance the application of the ANCF to the field of rotating structures.

The scientific contributions of the study can be summarized as follows:

- Development and numerical testing of a planar shear-deformable beam element formulation with individually interpolated shear parameters.
- Development and numerical testing of spatial ANCF-based higher order beam element formulations.
- Development and numerical testing of spatial ANCF-based higher order plate element formulations.
- Testing of lower and higher order spatial ANCF-based beam elements in rotating applications.



---

## The absolute nodal coordinate formulation

---

The absolute nodal coordinate formulation (ANCF) is a finite element based formulation developed for modeling applications in multibody dynamics, wherein all nodal coordinates are defined in the global (inertial) frame of reference. The coordinates consist of global positions and components of the position gradient, also called slope vectors. [30] This kind of formulation has several advantages over "classical" beam and plate finite element formulations, such as a constant mass matrix, which improves the performance of the element when used in conjunction with numerical solvers. ANCF-based elements also avoid the singularity problems that may arise from using angles to define rotation. A further advantage in dynamic applications is that the quadratic velocity vector, which describes centrifugal and Coriolis effects in the equations of motion, does not appear in ANCF-based models. [32] These effects are, however, still included in the description of inertia.

ANCF-based elements can be divided into two categories by their kinematics description: those defined using the conventional midline (or midplane) parameterization (see e.g. [29]) and those defined using continuum parameterization (fully-parameterized elements). For the second category, strains can be defined using three-dimensional elasticity based on continuum mechanics. However, elements that employ full three-dimensional elasticity have been known to suffer from various locking problems. This has previously limited the use of the formulation, although several methods have been developed to mitigate or avoid these problems, including *i.a.* reduced integration schemes [13].

One of the methods previously investigated to avoid locking-related issues is the concept of higher order elements, which has been further studied in the publications included in this work. In this approach, the polynomial basis of the element is enriched with higher order terms, and higher order derivatives are employed as additional nodal coordinates. These changes enable the element

to reproduce more complex deformation shapes. This, however, also introduces more computational complexity into the element by increasing the number of its degrees of freedom.

Elements with an enriched polynomial basis in the lengthwise direction to avoid shear locking were first proposed by Gerstmayr and Shabana [14]. Following this, Matikainen et al. [18, 19] introduced elements with higher-order polynomials in cross-sectional directions to alleviate Poisson locking. Higher order beam elements have consequently been studied in several articles, *e.g.* three-dimensional two-node beams in [34] and two-dimensional beams in [38]. In addition, a three-dimensional plate element following this principle was proposed and investigated in [21].

In this chapter, the theoretical background of the ANCF is clarified by presenting the formulation of a fully-parameterized beam element, including the formulation of its equations of motion. Also, the element's vector of elastic forces is formulated via two conceptually different approaches. In addition, the concept of higher order elements is illustrated by comparing the kinematics description of a lower order element with that of a higher order element.

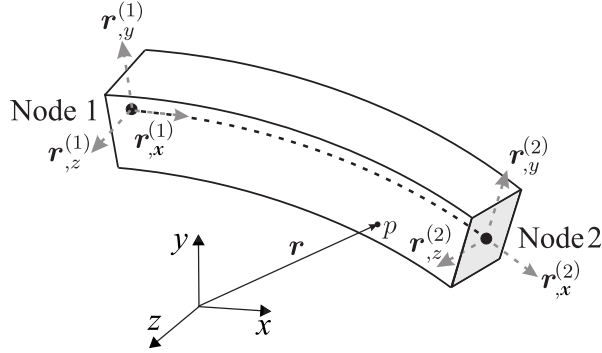
## 2.1 Beam element kinematics

Fig. 2.1 presents a conceptual diagram of a two-noded fully-parameterized spatial beam element based on the ANCF, as originally introduced by Shabana and Yakoub [33, 40]. The element being described as *fully-parameterized* implies that the full deformation gradient is represented in the chosen nodal coordinates, i.e. the element employs all three spatial slope vectors at each nodal location. This leads to a total of 24 nodal coordinates for the two-noded element.

Positions in the ANCF can be defined using spatial shape functions. The position  $\mathbf{r}$  of an arbitrary particle  $p$  within the element can therefore be defined as:

$$\mathbf{r}(\mathbf{x}, t) = \mathbf{S}_m(\mathbf{x})\mathbf{q}(t) = \mathbf{S}_m(\boldsymbol{\xi})\mathbf{q}(t) , \quad (2.1)$$

where  $\mathbf{S}_m$  is the shape function matrix,  $\mathbf{q}$  is the total vector of nodal coordinates and  $\mathbf{x}$  defines the physical coordinates of particle  $p$ . For an isoparametric element, the shape functions can be defined equivalently using physical coordinates  $\{x, y, z\}$  or local coordinates  $\{\xi, \eta, \zeta\}$ . Local coordinates can be scaled so that  $-1 \leq \xi, \eta, \zeta \leq 1$  to simplify the use of numerical integration algorithms. Fig. 2.2 illustrates the difference between the element's physical and local coordinate systems.



**Figure 2.1.** A fully-parameterized two-noded beam element based on the absolute nodal coordinate formulation. The element has a total of 24 nodal coordinates.

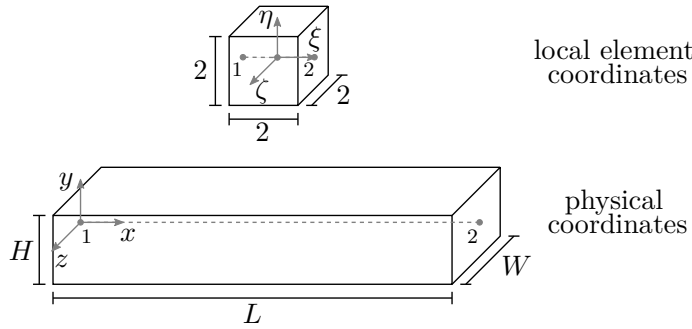


**Figure 2.2.** Physical and local element coordinate systems of the beam element.

As Fig. 2.1 illustrates, the nodal coordinate vector for node  $i$  can be written as:

$$\mathbf{q}^{(i)} = \begin{Bmatrix} \mathbf{r}^{(i)} \\ \mathbf{r}_{,x}^{(i)} \\ \mathbf{r}_{,y}^{(i)} \\ \mathbf{r}_{,z}^{(i)} \end{Bmatrix}, \quad (2.2)$$

where slope vectors are denoted using the following abbreviated notation:

$$\mathbf{r}_{,j}^{(i)} = \frac{\partial \mathbf{r}^{(i)}}{\partial j}, \quad j \in \{x, y, z\}. \quad (2.3)$$

The shape functions of the element can be derived using polynomial interpolation functions. The polynomial basis of the fully-parameterized element is chosen as:

$$P = \{1, x, y, z, xy, xz, x^2, x^3\}, \quad (2.4)$$

which leads to the following interpolation of position:

$$\mathbf{r} = \begin{Bmatrix} a_0 + a_1x + a_2y + a_3z + a_4xy + a_5xz + a_6x^2 + a_7x^3 \\ b_0 + b_1x + b_2y + b_3z + b_4xy + b_5xz + b_6x^2 + b_7x^3 \\ c_0 + c_1x + c_2y + c_3z + c_4xy + c_5xz + c_6x^2 + c_7x^3 \end{Bmatrix}, \quad (2.5)$$

where  $a_k$ ,  $b_k$  and  $c_k$  are polynomial coefficients, with  $k \in \{1, 2, 3, \dots, 7\}$ . Substituting the interpolation into Eq. (2.2) and constructing the total vector of nodal coordinates  $\mathbf{q}$ , the polynomial coefficients can be solved from the coordinates of the initial undeformed configuration. After factorization, this leads to the following set of spatial shape functions:

$$\begin{aligned} S_m^1 &= 1 - 3\alpha^2 + 2\alpha^3, & S_m^5 &= 3\alpha^2 - 2\alpha^3, \\ S_m^2 &= l(\alpha - 2\alpha^2 + \alpha^3), & S_m^6 &= l(-\alpha^2 + \alpha^3), \\ S_m^3 &= l(\beta - \alpha\beta), & S_m^7 &= l\alpha\beta, \\ S_m^4 &= l(\gamma - \alpha\gamma), & S_m^8 &= l\alpha\gamma, \end{aligned} \quad (2.6)$$

where  $\alpha = x/L$ ,  $\beta = y/L$ ,  $\gamma = z/L$ . The shape function matrix can then be constructed from the individual shape functions as follows:

$$\mathbf{S}_m = \begin{bmatrix} S_m^1 \mathbf{I} & S_m^2 \mathbf{I} & S_m^3 \mathbf{I} & S_m^4 \mathbf{I} & S_m^5 \mathbf{I} & S_m^6 \mathbf{I} & S_m^7 \mathbf{I} & S_m^8 \mathbf{I} \end{bmatrix}, \quad (2.7)$$

where  $\mathbf{I}$  is a  $3 \times 3$  identity matrix.

## 2.2 Higher order element kinematics

To alleviate the locking problems prevalent in ANCF-based elements using full three-dimensional elasticity, several approaches have previously been investigated. One of these methods is based on enriching the polynomial basis of the element and introducing higher positional derivatives to the nodal coordinates. [15, 20] Elements based on this approach have thus been called *higher order* elements. In this section, differences between the previously introduced "classical" ANCF element and a higher order element are presented.

For example, let us consider the two-node higher order ANCF-based beam element illustrated in Fig. 2.3, originally introduced by Shen et al. [34]. A two-noded element is presented here in order to retain parity with the previously presented element. As Fig. 2.3 shows, the element employs three additional slope vectors in the transverse directions. Therefore, the element has a total of 42 nodal coordinates.

The nodal coordinate vector of the element can be written as:

$$\mathbf{q}^{(i)} = \left\{ \mathbf{r}^{(i)\text{T}} \quad \mathbf{r}_{,x}^{(i)\text{T}} \quad \mathbf{r}_{,y}^{(i)\text{T}} \quad \mathbf{r}_{,z}^{(i)\text{T}} \quad \mathbf{r}_{,yz}^{(i)\text{T}} \quad \mathbf{r}_{,yy}^{(i)\text{T}} \quad \mathbf{r}_{,zz}^{(i)\text{T}} \right\}^{\text{T}}. \quad (2.8)$$

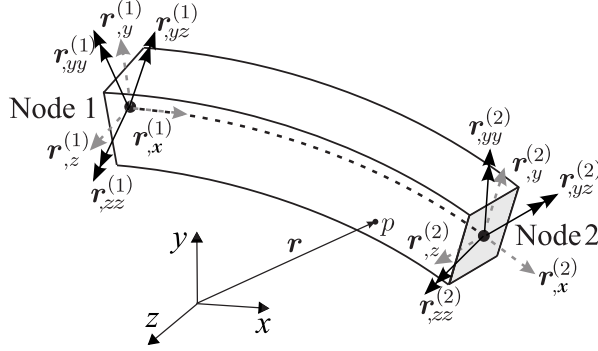


**Figure 2.3.** A two-noded higher order ANCF-based element with 42 DOF.

The polynomial basis chosen for the element is:

$$P_h = P \cup \{yz, y^2, z^2, xyz, xy^2, xz^2\}, \quad (2.9)$$

where  $P$  is the polynomial basis of the previously-presented fully-parameterized element, as defined in Eq. (2.4). It can be seen that the main difference between this higher order element and the fully parameterized element is the quadratic interpolation employed in the transverse directions. This choice of polynomial basis, in conjunction with the choice of coordinates, leads to the following set of shape functions:

$$\begin{aligned} S_m^1 &= 1 - 3\alpha^2 + 2\alpha^3, & S_m^8 &= 3\alpha^2 - 2\alpha^3, \\ S_m^2 &= l(\alpha - 2\alpha^2 + \alpha^3), & S_m^9 &= l(-\alpha^2 + \alpha^3), \\ S_m^3 &= l(\beta - \alpha\beta), & S_m^{10} &= l\alpha\beta, \\ S_m^4 &= l(\gamma - \alpha\gamma), & S_m^{11} &= l\alpha\gamma, \\ S_m^5 &= l^2(\beta\gamma - \alpha\beta\gamma), & S_m^{12} &= l^2\alpha\beta\gamma, \\ S_m^6 &= \frac{l^2}{2}(\beta^2 - \alpha\beta^2), & S_m^{13} &= \frac{l^2}{2}\alpha\beta^2, \\ S_m^7 &= \frac{l^2}{2}(\gamma^2 - \alpha\gamma^2), & S_m^{14} &= \frac{l^2}{2}\alpha\gamma^2. \end{aligned} \quad (2.10)$$

The total shape function matrix can be constructed in the same manner as above:

$$\mathbf{S}_m = \begin{bmatrix} S_m^1 \mathbf{I} & S_m^2 \mathbf{I} & S_m^3 \mathbf{I} & \dots & S_m^{14} \mathbf{I} \end{bmatrix}. \quad (2.11)$$

It is notable that the shape functions corresponding to nodal positions and gradients of the higher order element are identical to those of the previously presented fully-parameterized element. This element therefore serves as an example of a higher order element formulation because it can be considered an extension

of the fully-parameterized element. However, this specific element formulation has been previously shown to suffer from locking issues due to its inclusion of in-slope vectors (i.e. slope vectors in the longitudinal direction) in the nodal coordinates. [28] *Publication II* further illustrates this fact.

### 2.3 Equations of motion

The weak form of the equations of motion for the element can be derived using the principle of virtual work. The system's Lagrangian can be written as follows:

$$\mathcal{L} = W_k - W_p , \quad (2.12)$$

where  $W_k$  and  $W_p$  are the kinetic and potential energies of the element, respectively. The potential energy can be further divided into two components as follows:

$$W_p = W_i - W_e , \quad (2.13)$$

where  $W_i$  consists of the internal (strain) energy, while  $W_e$  comprises the potential energies of external forces. If the strain energy is defined via the continuum mechanics based approach, further detailed in the following section, and nonconservative forces are disregarded, the variations of the system's energy components with regard to  $\mathbf{q}(t)$  can be written as:

$$\delta W_k = \int_V \rho \dot{\mathbf{r}} \cdot \delta \dot{\mathbf{r}} \, dV , \quad (2.14)$$

$$\delta W_i = \int_V \mathbf{S} : \delta \mathbf{E} \, dV , \quad (2.15)$$

$$\delta W_e = \int_V \mathbf{b} \cdot \delta \mathbf{r} \, dV , \quad (2.16)$$

where  $\mathbf{S}$  is the second Piola–Kirchhoff stress tensor,  $\mathbf{E}$  is the Green–Lagrange strain tensor and  $\mathbf{b}$  is the vector of body forces (*e.g.* gravity). The operator  $:$  designates a double dot product. Using the rule of partial integration, the time integral of the variation of kinetic energy can alternatively be written as:

$$\begin{aligned} \int_{t_1}^{t_2} \delta W_k \, dt &= \int_{t_1}^{t_2} \int_V \rho \dot{\mathbf{r}} \cdot \delta \dot{\mathbf{r}} \, dV \, dt \\ &= \left[ \int_V \rho \dot{\mathbf{r}} \cdot \delta \mathbf{r} \, dV \right]_{t_1}^{t_2} - \int_{t_1}^{t_2} \int_V \rho \ddot{\mathbf{r}} \cdot \delta \mathbf{r} \, dV \, dt . \end{aligned} \quad (2.17)$$

From the Lagrangian, Hamilton's principle gives the equation:

$$\delta \mathcal{I} = \delta \int_{t_1}^{t_2} \mathcal{L} \, dt = \delta \int_{t_1}^{t_2} (W_k - W_i + W_e) \, dt = 0 , \quad (2.18)$$

where  $\mathcal{I}$  is the system's action functional and  $t_1 < t_2$  are endpoints in time. Defining that system perturbation  $\varepsilon(t)$  is zero at the endpoints gives the boundary conditions  $\varepsilon(t_1) = \varepsilon(t_2) = 0$ , which causes the first term of Eq. (2.17) to vanish. Finally, Hamilton's principle requires that  $\delta\mathcal{I} = 0$  for all perturbations  $\varepsilon(t)$ , leading to the weak form of equations of motion written as follows:

$$\int_V \rho \ddot{\mathbf{r}} \cdot \delta \mathbf{r} \, dV + \int_V \mathbf{S} : \delta \mathbf{E} \, dV - \int_V \mathbf{b} \cdot \delta \mathbf{r} \, dV = 0 . \quad (2.19)$$

As previously defined in Eq. (2.1), position  $\mathbf{r}$  is defined using shape functions and nodal coordinates. Therefore, it is possible to present the terms of Eq. (2.19) as functions of the total nodal coordinate vector  $\mathbf{q}$ . They can thus be written as:

$$\delta W_k = \ddot{\mathbf{q}}^T \int_V \rho \mathbf{S}_m^T \mathbf{S}_m \, dV \cdot \delta \mathbf{q} = \ddot{\mathbf{q}}^T \mathbf{M} \cdot \delta \mathbf{q} , \quad (2.20)$$

$$\delta W_i = \int_V \mathbf{S} : \frac{\partial \mathbf{E}}{\partial \mathbf{q}} \, dV \cdot \delta \mathbf{q} = \mathbf{F}_e \cdot \delta \mathbf{q} , \quad (2.21)$$

$$\delta W_e = \int_V \mathbf{b}^T \mathbf{S}_m \, dV \cdot \delta \mathbf{q} = \mathbf{F}_b \cdot \delta \mathbf{q} , \quad (2.22)$$

where  $\mathbf{M}$  can be identified as the mass matrix,  $\mathbf{F}_e$  as the vector of elastic forces and  $\mathbf{F}_b$  as the vector of body forces.

By examining Eq. (2.20), it can be concluded that the mass matrix of the ANCF-based element is not dependent on the nodal coordinates and is therefore indeed constant, as previously stated. This is highly desirable for computational purposes. However, Eq. (2.21) also indicates that the elastic force vector is defined via partial differentiation of the strain tensor with regard to the nodal coordinate vector. Therefore, it is dependent on the nodal coordinates and may be highly nonlinear.

## 2.4 Formulation of elastic forces

In the publications included in this work, two different approaches to the definition of the elastic force vector of an ANCF-based element have been employed. These are the approach based on general three-dimensional elasticity – the *continuum mechanics formulation* – and the approach based on generalized strains – the *structural mechanics formulation*. Both approaches are briefly introduced below by highlighting their conceptual differences.

### 2.4.1 Continuum mechanics formulation

In the continuum mechanics based formulation, which employs three-dimensional elasticity, the relationship between stresses and strains is defined by a *constitutive model*, alternatively known as a material model. Many different models can be found in the literature and be employed to define the elastic forces for ANCF-based elements. [24]

One of the models used most widely in the context of the ANCF is the Saint Venant–Kirchhoff (hyperelastic) material model, which is a simple model for three-dimensional elasticity and enforces a linear relationship between stresses and strains. The model employs the second Piola–Kirchhoff stress tensor as its stress measure and the Green–Lagrange strain tensor as its strain measure. While the St. Venant–Kirchhoff model is simple to implement due to its simple strain energy density function, it is inaccurate in cases where effects related to material nonlinearity are significant.

Other constitutive models may be used to model more complex material behavior. In the context of hyperelastic materials, well-known models with nonlinear stress-strain relations include *i.a.* the Neo-Hookean and Mooney–Rivlin models, which have previously been applied in the ANCF (see e.g. [17]). Different models are employed in the modeling of different types of materials: the Mooney–Rivlin model, for example, is commonly used for incompressible materials, such as rubber. In addition to hyperelastic models, models with plastic and viscoelastic behavior have also been studied in the context of the ANCF; see *e.g.* [16] for a summary.

The St. Venant–Kirchhoff (hyperelastic) material model is employed to compute the elastic forces of the previously-presented ANCF-based element. The St. Venant–Kirchhoff model is defined by the following strain energy density function:

$$\Psi(\mathbf{E}) = \frac{1}{2}\lambda(\text{tr}\mathbf{E})^2 + \mu \text{tr}(\mathbf{E}^2) , \quad (2.23)$$

where  $\lambda$  and  $\mu$  are Lamé material constants. Assuming an elastic isotropic material yields the following relation between the strain and stress tensors:

$$\mathbf{S} = \frac{\partial\Psi}{\partial\mathbf{E}} = \lambda \text{tr}(\mathbf{E})\mathbf{I} + 2\mu\mathbf{E} , \quad (2.24)$$

where  $\mathbf{I}$  is the identity tensor. The Green strain tensor  $\mathbf{E}$  can be derived from the deformation gradient  $\mathbf{F}$  as follows:

$$\mathbf{E} = \frac{1}{2}(\mathbf{F}^T\mathbf{F} - \mathbf{I}) . \quad (2.25)$$

The deformation gradient tensor can, in turn, be defined as follows:

$$\mathbf{F} = \frac{\partial\mathbf{r}}{\partial\mathbf{r}_0} = \frac{\partial\mathbf{r}}{\partial\mathbf{x}} \left( \frac{\partial\mathbf{r}_0}{\partial\mathbf{x}} \right)^{-1} , \quad (2.26)$$

where  $\mathbf{r}$  and  $\mathbf{r}_0$  are defined in the current and initial configurations of the element, respectively, and  $\mathbf{x} = \{x \ y \ z\}^T$ . Finally, substituting Eq. (2.26) and Eq. (2.25) into Eq. (2.24) allows the solution of both stress and strain tensors, and consequently the solution of the elastic force vector in Eq. (2.20) as:

$$\mathbf{F}_e^{\text{cm}} = \int_V \mathbf{S} : \frac{\partial \mathbf{E}}{\partial \mathbf{q}} dV . \quad (2.27)$$

### 2.4.2 Structural mechanics formulation

To avoid the locking problems that can arise from three-dimensional elasticity, elastic forces can alternatively be defined using a structural mechanics based approach. [6] In this approach, strain components such as shear and bending strains are handled independently of each other. Despite the fact that the structural mechanics formulation has been shown to produce accurate results, it can be cumbersome to use in the case of advanced material models, which are considerably simpler to implement when using the continuum mechanics approach. Let the internal (strain) energy component be redefined as follows:

$$W_i = W_i^{\text{asb}} + W_i^c , \quad (2.28)$$

where the first term  $W_i^{\text{asb}}$  consists of axial, shear and bending strain components while the second term  $W_i^c$  consists of the strains caused by cross-sectional deformation. Using generalized strains, the first term can be written as: [25, 26]

$$W_i^{\text{asb}} = \frac{1}{2} \int_0^L (EA\Gamma_1^2 + GA\Gamma_2^2 k_{s2} + GA\Gamma_3^2 k_{s3} + GI_1\kappa_1^2 + EI_2\kappa_2^2 + EI_3\kappa_3^2) \Big|_{y,z=0} dx , \quad (2.29)$$

where  $l$  is the element length,  $A$  is the element cross-sectional area,  $E$  is Young's modulus,  $G$  is the shear modulus,  $I_1$ ,  $I_2$  and  $I_3$  are sectional stiffness parameters, and  $k_{s2}$  and  $k_{s3}$  are shear correction factors. Here, the strains consist of six components: axial strain  $\Gamma_1$ , transverse shear strains  $\Gamma_2$  and  $\Gamma_3$ , torsional shear strain  $\kappa_1$ , and bending strains  $\kappa_2$  and  $\kappa_3$ . These strain components can be defined using a cross-sectional reference frame, which defines the orientation of the cross-section in the deformed configuration. The base vectors  $\mathbf{e}_1$ ,  $\mathbf{e}_2$  and  $\mathbf{e}_3$  of the cross-sectional frame can be defined using the element's slope vectors. For example:

$$\begin{aligned} \mathbf{e}_1 &= \frac{\bar{\mathbf{e}}_1}{|\bar{\mathbf{e}}_1|}, \quad \bar{\mathbf{e}}_1 = \mathbf{r}_{,y} \times \mathbf{r}_{,z} , \\ \mathbf{e}_3 &= \frac{\bar{\mathbf{e}}_3}{|\bar{\mathbf{e}}_3|}, \quad \bar{\mathbf{e}}_3 = \mathbf{r}_{,z} , \\ \mathbf{e}_2 &= \frac{\bar{\mathbf{e}}_2}{|\bar{\mathbf{e}}_2|}, \quad \bar{\mathbf{e}}_2 = \bar{\mathbf{e}}_3 \times \bar{\mathbf{e}}_1 . \end{aligned} \quad (2.30)$$

Consequently, the axial strain and transverse shear strains can be written as:

$$\begin{aligned}\Gamma_1 &= \mathbf{e}_1^T \mathbf{r}_{,x} - 1 , \\ \Gamma_2 &= \mathbf{e}_2^T \mathbf{r}_{,x} , \\ \Gamma_3 &= \mathbf{e}_3^T \mathbf{r}_{,x} ,\end{aligned}\tag{2.31}$$

and the remaining strains can be defined using the vector of twist and curvature  $\mathbf{k}$ , which can be written as:

$$\mathbf{k} = \frac{1}{2} \sum_{i=1}^3 \mathbf{e}_i \times \mathbf{e}_{i,x} = \frac{1}{2} (\mathbf{e}_1 \times \mathbf{e}_{1,x} + \mathbf{e}_2 \times \mathbf{e}_{2,x} + \mathbf{e}_3 \times \mathbf{e}_{3,x}) .\tag{2.32}$$

Finally, the torsion shear strain and the bending strains can be gained from the corresponding elements of the vector:

$$\boldsymbol{\kappa} = \mathbf{A}_e^T \mathbf{k} ,\tag{2.33}$$

where  $\mathbf{A}_e = [\mathbf{e}_1 \ \mathbf{e}_2 \ \mathbf{e}_3]$  is a rotation matrix describing the cross-sectional frame.

Eq. (2.29) demonstrates that bending and torsional strains are only considered here in terms of the centerline of the element, which is characteristic to this type of strain formulation. This attribute makes structural mechanics based strain formulation incompatible in principle with higher order elements due to the fact that the higher order terms have the value of zero on the central axis.

The second strain energy term can be defined as follows:

$$W_i^c = \frac{1}{2} \int_0^L \left( EA(E_{22}^2 + E_{33}^2) + 2GAE_{23}^2 \right) dx ,\tag{2.34}$$

where  $E_{ij}$  are elements of the Green strain tensor, defined in Eq. (2.25).

Once again, the principle of virtual work can be employed to derive the equations of motion. The variations of the strain energy terms can be written in terms of the nodal coordinates  $\mathbf{q}$  as follows:

$$\begin{aligned}\delta W_i^{asb} &= \left( \frac{1}{2} \nabla_q \int_0^L (EA\Gamma_1^2 + GA\Gamma_2^2 k_{s2} + GA\Gamma_3^2 k_{s3} \right. \\ &\quad \left. + GI_1 \kappa_1^2 + EI_2 \kappa_2^2 + EI_3 \kappa_3^2) \Big|_{y,z=0} dx \right) \cdot \delta \mathbf{q} ,\end{aligned}\tag{2.35}$$

$$\delta W_i^c = \left( \frac{1}{2} \nabla_q \int_0^L \left( (EA(E_{22}^2 + E_{33}^2) + 2GAE_{23}^2) dx \right) \right) \cdot \delta \mathbf{q} .\tag{2.36}$$

Finally, using the same approach as above, the elastic force vector can be derived from the variation of strain energy as follows:

$$\mathbf{F}_e^{\text{sm}} = \nabla_q \left( W_i^{asb} + W_i^c \right) .\tag{2.37}$$

## Summary of the findings

The objective of this dissertation was to develop ANCF-based finite elements and apply them to the dynamical modeling of flexible multibody systems. This can be divided into two sub-objectives: 1) developing element formulations and 2) applying the developed formulations into the simulation of mechanical systems.

Of the included publications, *Publication I*, *Publication II* and *Publication III* chiefly focus on the first of the above-mentioned sub-objectives. In these publications, element formulations based on the ANCF are introduced and tested via numerical experiments. On the other hand, *Publication IV* and *Publication V* focus on the second objective. In these publications, the previously proposed elements are applied to the simulation of rotating systems, and the produced results are compared with other formulations.

This chapter summarizes the main findings and conclusions of the five included publications. The findings are introduced below by publication.

### PUBLICATION I

The first publication proposed a new planar gradient deficient beam finite element based on the absolute nodal coordinate formulation. In this formulation, the position of the beam centerline is interpolated using cubic polynomials. The most important addition of the element is that shear deformation along the length of the element is taken into account via independently interpolated terms. A structural mechanics based formulation is used to define the strain energy. It can be stated that the element is based on the ANCF since all nodal coordinates are defined in the inertial reference frame. However, due to the addition of separate interpolation polynomials for shear deformation, the mass matrix of the element

is not explicitly constant. However, this is compensated by an added penalty term for the length of vector  $\mathbf{t}$  in the strain energy, which ensures that the mass matrix can be approximated with a constant matrix without significant loss in accuracy.

The significant kinematic difference between the proposed element and other planar element formulations can be illustrated as follows. The element consists of two nodes. Identically to the planar gradient deficient ANCF-based beam element presented in [22], the position of the element centerline  $\mathbf{r}$  is interpolated using cubic polynomials. The polynomial expression can be written as follows:

$$\mathbf{r} = \begin{Bmatrix} a_0 + a_1x + a_2x^2 + a_3x^3 \\ b_0 + b_1x + b_2x^2 + b_3x^3 \end{Bmatrix}, \quad (3.1)$$

where  $x = 0 \dots l$  is the arc coordinate along the centerline, and  $a$  and  $b$  are polynomial coefficients. However, in addition to this position interpolation, a separate "shear deformation vector"  $\mathbf{s}$  is defined using linear interpolation as follows:

$$\mathbf{s} = \begin{Bmatrix} c_0 + c_1x \\ d_0 + d_1x \end{Bmatrix}. \quad (3.2)$$

As Fig. 3.1 shows, cross-section orientation vector  $\mathbf{t}$  can be defined as a sum of the directional derivative of the position vector and the shear deformation vector  $\mathbf{s}$ . In the proposed element, both the shear deformation vector and the cross-section orientation vector are represented in the nodal coordinates, leading to a total of 12 degrees of freedom. This can be represented as follows:

$$\mathbf{q}^{(i)} = \begin{Bmatrix} \mathbf{r}^{(i)} \\ \mathbf{t}^{(i)} \\ \mathbf{s}^{(i)} \end{Bmatrix} \quad (3.3)$$

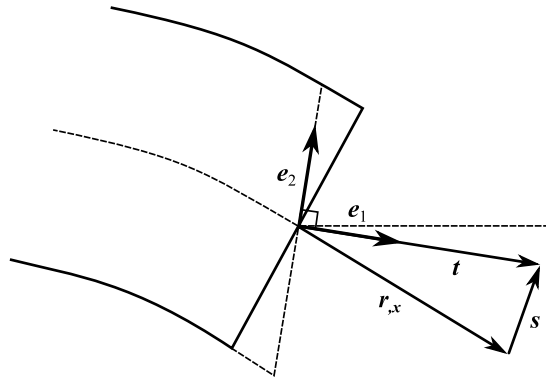


**Figure 3.1.** Description of shear in the element proposed in *Publication I*.

The publication examined the accuracy and convergence properties of the element through static and dynamic tests taken from literature. In the static test (large displacement cantilever), the proposed element displayed a higher rate of convergence than the reference results computed using BEAM188 elements in the commercial software ANSYS [1]. In addition, the convergence rate of the proposed formulation was comparable to that of the planar ANCF-based element proposed by Nachbagauer et al. [27], while consistently displaying a lower error when using the reduced integration scheme. Fig. 3.2 illustrates these results. The converged results were also accurate compared to results computed using the geometrically exact beam formulation proposed by Simo and Vu-Quoc [36].

Two dynamic tests were performed on the proposed element. The first was a modal analysis on the lower eigenfrequencies of a simply supported beam. For all of the studied frequencies, the proposed element produced results corresponding to six significant digits of analytically calculated values using 32 elements. In the dynamic time-domain test, the response of a highly flexible beam was studied. The response was found to follow the reference set closely. It was also found that the computational effort spent to compute the dynamic response was smaller than that of the compared element formulation.

After examining the results of the numerical tests, the proposed element can be said to perform well. However, to take full advantage of the element, the formulation should be extended to a spatial (three-dimensional) case. At present, while the element has advantages compared to other planar element formulations, it has limited applications in the simulation of mechanical systems.

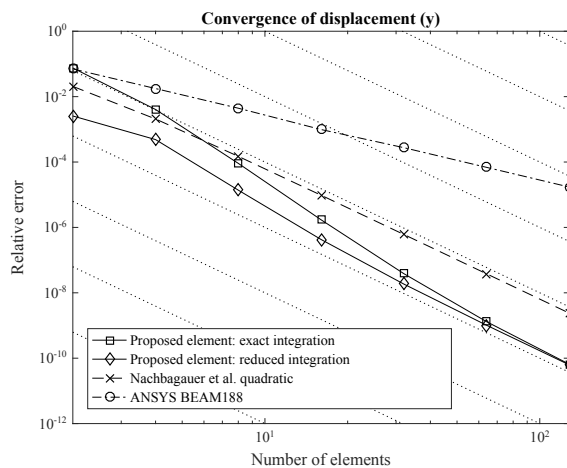


**Figure 3.2.** *Publication I:* comparison of convergence rates in terms of the number of elements. Dotted diagonal lines illustrate a fourth order rate of convergence.

## PUBLICATION II

The second publication studied a number of higher order beam elements based on the absolute nodal coordinate formulation. The studied element formulations consist of three- or four-noded beam elements with no in-slope vectors (*i.e.* longitudinal slope vectors are not represented in the nodal coordinates). The publication focuses especially on the effect of the enriched polynomial basis on the Poisson locking phenomenon, which often manifests in lower order elements employing three-dimensional elasticity.

The studied elements can be considered as extensions of the lower order three-node ANCF-based beam element proposed by Nachbagauer et al. [26], designated with the number 3333 in the paper. This designation follows the four-digit naming scheme by Dmitrochenko and Mikkola in [10]. The nodal coordinate vector of this element is defined as:

$$\mathbf{q}^{(i)} = \begin{Bmatrix} \mathbf{r}^{(i)} \\ \mathbf{r}_{,x}^{(i)} \\ \mathbf{r}_{,y}^{(i)} \end{Bmatrix}. \quad (3.4)$$

It is observed that the original element only includes two slope vectors – one in each transverse direction. The publication proposed higher order elements are with three, four, five or nine slope vectors included in the nodal coordinates. The most complex considered element (designated 34X4, illustrated in Fig. 3.3) therefore consists of four nodes and has a total of ten spatial vectors per node, amounting to 120 DOF. The nodal coordinate vector of this element is as follows:

$$\mathbf{q}^{(i)} = \left\{ \begin{array}{cccccc} \mathbf{r}^{(i)\text{T}} & \mathbf{r}_{,y}^{(i)\text{T}} & \mathbf{r}_{,z}^{(i)\text{T}} & \mathbf{r}_{,yz}^{(i)\text{T}} & \mathbf{r}_{,yy}^{(i)\text{T}} & \\ & \mathbf{r}_{,zz}^{(i)\text{T}} & \mathbf{r}_{,yyz}^{(i)\text{T}} & \mathbf{r}_{,yzz}^{(i)\text{T}} & \mathbf{r}_{,yyy}^{(i)\text{T}} & \mathbf{r}_{,zzz}^{(i)\text{T}} \end{array} \right\}^{\text{T}}. \quad (3.5)$$

The continuum mechanics based elastic force formulation with the St. Venant–Kirchhoff material model is employed for all of the examined elements. However, both continuum mechanics and structural mechanics based formulations are employed for the original element to compare performance in the numerical tests.

Several numerical tests are performed to analyze the performance of the proposed elements. The tests were composed of three different static problems (small and large displacement cantilever problems as well as the Princeton beam experiment) and two modal analysis problems (simply supported and unconstrained beam). Finally, a convergence analysis was performed. In the tests, the proposed elements were compared with the original element (3333) and the two-node higher order ANCF beam element with a longitudinal slope vector (designated 3273 in the publication, see section 2.2). In addition, the numerical test results were compared with those computed using beam and solid elements in the commercial finite element software ANSYS.

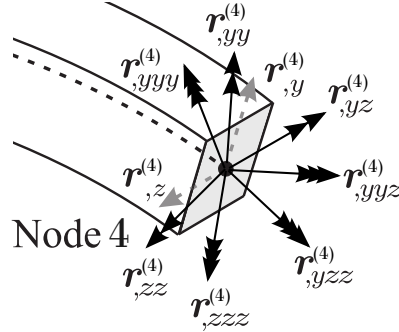


**Figure 3.3.** Nodal vectors of the four-node element 34X3 proposed in *Publication II*.

In the small displacement cantilever tests, it was found that of the proposed higher order elements, those with three or four slope vectors still suffered from locking due to the inadequate approximation of cross-sectional deformation. For this reason, these elements were disqualified from further study. On the other hand, the elements with five and nine slopes were found to perform adequately. In the modal analyses, the element with the highest order of approximation in transversal directions was found to perform closest to the reference. Finally, in the large displacement static problems, the remaining higher order elements were found to produce accurate results. Especially in the Princeton beam experiment, which involves pronounced nonlinear behavior, they displayed considerably higher accuracy than the lower order ANCF-based elements.

In conclusion, the paper demonstrates that accurate results in complex multiaxial load cases can be produced using higher order ANCF-based beam elements employing full three-dimensional elasticity. Although the rate of convergence for the higher order elements was lower than that of the compared lower order element, the conceptual differences between the elements meant that the results gained using the proposed elements were judged to be more accurate. This is best displayed in the Princeton beam experiment results shown in Fig. 3.4.

### PUBLICATION III

The second publication studied the usage of a high polynomial order in all three directions without the use of in-plane slopes in the context of 3D beam elements. Consequently, the focus of *Publication III* was on extending this to spatial plate element formulations. The paper considers seven different quadrilateral ANCF-based plate elements with different polynomial bases. The number of degrees of freedom ranges from a minimum of 24 per element to a maximum of 81 per element, at maximum. The examined elements consist of four, eight or nine

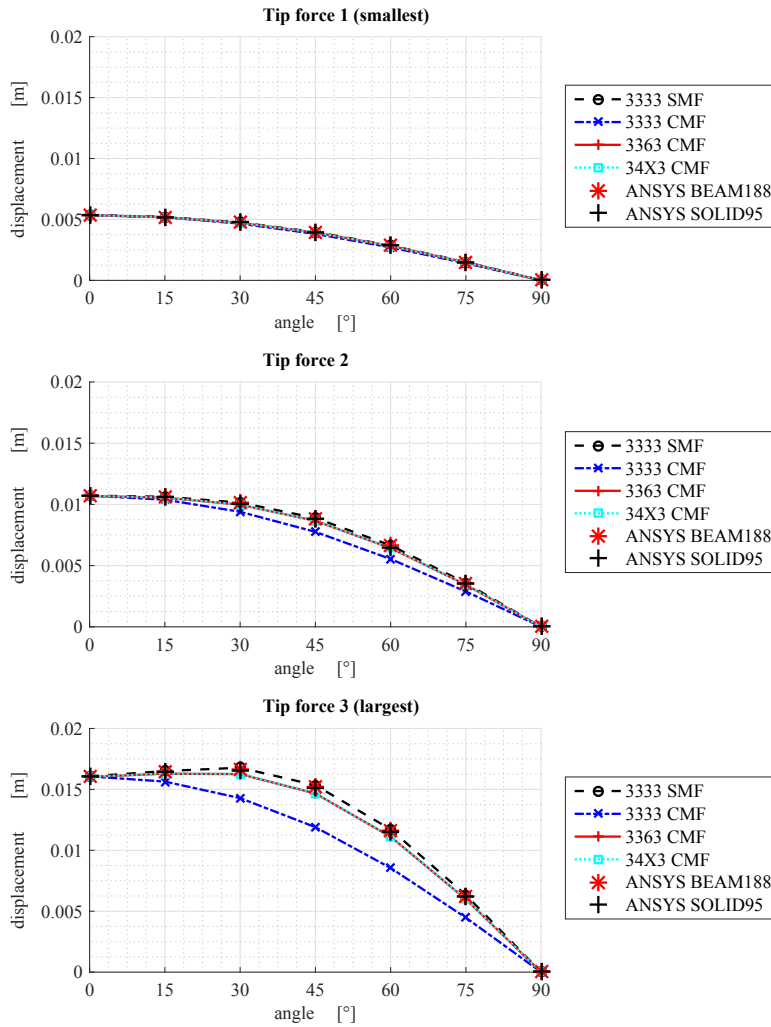


**Figure 3.4.** *Publication II:* Princeton beam experiment – flapwise displacement as a function of the force angle with three different (constant) tip force values. 3363 and 34X3 are higher order elements proposed in the publication, while 3333 is a lower order element.

nodes. All elements make use of the St. Venant–Kirchhoff material model for the calculation of elastic forces, and Gaussian quadrature in all three dimensions for integration over volume. Fig. 3.5 presents a diagram of a nine-node spatial plate element.

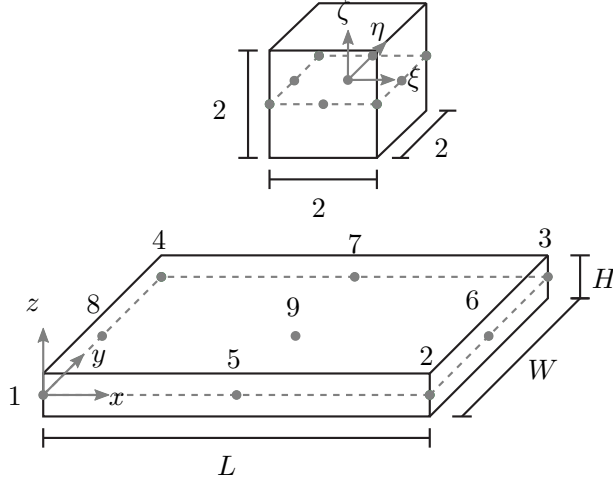


**Figure 3.5.** *Publication III*: diagram of the nine-node spatial plate element.

The elements were tested using several numerical experiments to gain information about their convergence rates and the accuracy of the produced results. The tests were chosen from the literature and consist of four different static displacement experiments (small and large displacement cantilever plate experiment, simply supported plate experiment with body load and the Princeton beam experiment) and a dynamic experiment (a free-flying flexible plate example). In these tests, the performance of the studied formulations is compared against that of various elements in the commercial finite element software ANSYS.

When examining the results of the cantilever and simply supported beam tests, it was found that of the studied elements, those four without at least an approximation order of two produce inaccurate results when Poisson's ratio is not zero. Therefore, it is judged that they suffer from locking. Consequently, these elements were removed from further study and the investigation focused on the remaining three better-performing elements.

Of the three element formulations that performed well in the small-displacement tests, all were found to perform adequately in the large displacement cantilever test. However, the eight- and nine-node elements (designated 3833 and 3933, respectively) were found to produce an advantage in accuracy when compared with the remaining four-noded element (designated 3453, originally proposed by Matikainen et al. [21]) in the test based on the Princeton beam experiment. This is illustrated in Fig. 3.6. The eight- and nine-noded elements were also shown to be reasonably accurate in the time-domain simulation test compared with results computed using ANSYS.

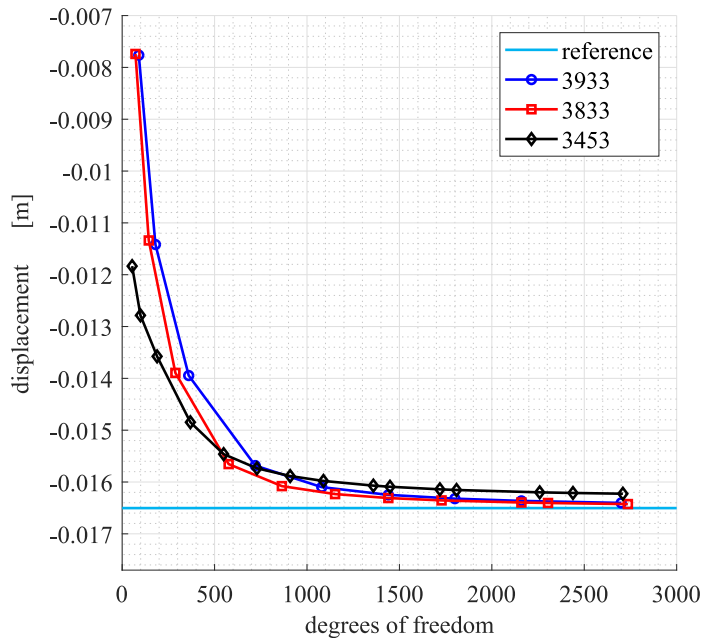


**Figure 3.6.** Results from *Publication III*: flapwise displacement in the Princeton beam experiment. Highest force case, force angle  $\alpha = 30^\circ$ . Reference results computed using SOLID95 elements in ANSYS.

In conclusion, the publication showed that it is possible to produce accurate results in complex load cases using higher order ANCF-based plate elements and employing the St. Venant–Kirchhoff material model. The best-performing elements were also found to exhibit satisfactory convergence rates. It can therefore be said that these elements avoid the commonly-found Poisson and shear locking problems, which endorses their applicability to mechanical simulation problems.

#### PUBLICATION IV

In the fourth publication, two element types which have not been formulated primarily with rotating applications in mind were tested in the simulation of a high-speed rotating structure. These element formulations were the superelement formulation as proposed by Boer et al. [7] and the quadratic beam element formulation based on the ANCF as proposed by Nachbagauer et al. [26]. These formulations are considerably different conceptually, and it was believed that evaluating their performance would give insight into new avenues in rotating system simulation.

For modal analysis, it was judged necessary to find a simplified procedure for evaluating the Campbell diagram (see section 1.2) of a model constructed using ANCF-based beam elements. This is due to the fact that the inertial terms related to rotation are not easily separable in ANCF-based models. By separating the rotational velocity component, a gyroscopic matrix could be derived as follows:

$$\mathbf{G} = 2 \int_V \rho \mathbf{S}_m^T (y \mathbf{S}_{m,z} - z \mathbf{S}_{m,y}) dV , \quad (3.6)$$

where  $\mathbf{S}_{m,y} = \partial \mathbf{S}_m / \partial y$  and  $\mathbf{S}_{m,z} = \partial \mathbf{S}_m / \partial z$ . It should be noted that the gyroscopic effect does not normally need to be separately accounted for in this way in the equations of motion of an ANCF-based model since the effect is already included in the description of inertia. Using this definition, it is possible to compute the Campbell diagram by performing a modal analysis on the linearized (common in the context of rotordynamics) form of the equations of motion:

$$\mathbf{M} \ddot{\mathbf{q}} + (\Omega \mathbf{G} + \mathbf{C}) \dot{\mathbf{q}} + \mathbf{K} \mathbf{q} = \mathbf{F} , \quad (3.7)$$

where  $\mathbf{M}$ ,  $\mathbf{C}$  and  $\mathbf{K}$  are the mass, damping and stiffness matrices of the system, respectively, while  $\mathbf{F}$  is the external force vector and  $\Omega$  is the rotational velocity.

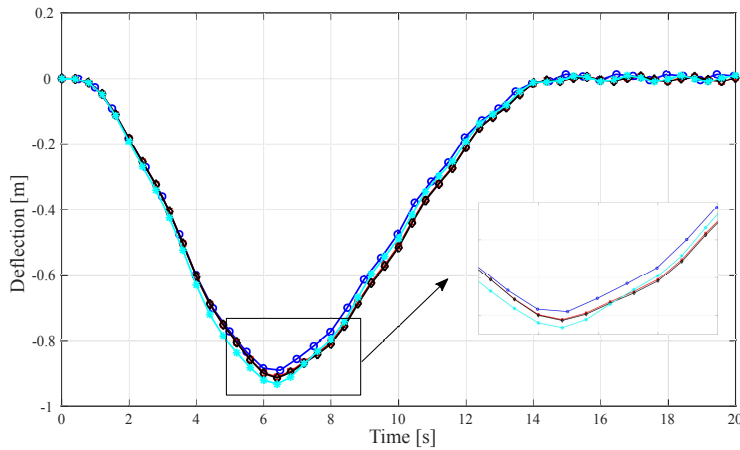
The performance of the studied formulations was examined via two numerical tests, found in the literature. The first test was a spinning beam example, in which the dynamic response in the time domain was examined. The second example studied an unbalanced rotating shaft, for which both time-domain and frequency-domain dynamic analyses were performed. The results of both tests, produced using both formulations, were compared against those produced in the commercial finite element software ANSYS and those available in literature.

In the spinning beam test, two cases with different angular velocities were tested. In the lower speed case, both element formulations produced results near the reference results produced using ANSYS. In the higher speed case, the results diverged more, but the responses were still similar. This is illustrated in Fig. 3.7a. It was judged that the differences were caused by the more pronounced rotational effects and the conceptual differences between the elements.

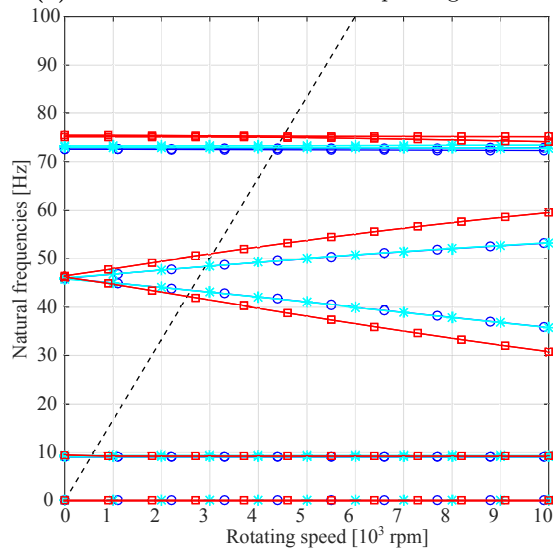
In the unbalanced shaft test, the ANCF-based element was found to produce results closer to the reference results than the superelement formulation, both in modal and time-domain computations. As can be observed from the Campbell diagram presented in Fig. 3.7b, the superelement results differ considerably from the ANCF and ANSYS result sets. In the time-domain test, for which reference results were available in the literature [4], the same observation was made.

In conclusion, it was judged that the ANCF-based element was able to produce results that agree with "classical" beam elements, even in applications where rotational effects are significant. However, the superelement formulation was

seen to perform unpredictably. While it can produce accurate results in certain cases, it was unable to produce satisfactory results in the second numerical test. Changing the number of elements in the mesh did not always produce the expected effect when using this formulation. Therefore, without further investigation, the superelement formulation cannot be said to perform adequately in the dynamic simulation of rotating machines.



(a) Transient test: deflection of spinning beam.



(b) Modal test: Campbell diagram.

**Figure 3.7.** Numerical results from *Publication IV*.  $\circ$  ANSYS BEAM188 (20 elements),  $\ast$  ANCF beam (16 elements in (a), 4 in (b)),  $\square$  and  $\diamond$  nonlinear superelements with velocity transformation matrices  $B1$  and  $B2$ , respectively (4 elements).

## PUBLICATION V

In the fifth publication, the four-node higher order beam element designated as 34X3, proposed in *Publication II*, was further tested by applying it to the modeling of rotating structures. Its ability to capture the cross-sectional deformations caused by inertial forces in rotation were tested in numerical dynamic tests. The results were compared with those acquired using the commercial finite element software ANSYS and analytical formulas.

The numerical tests consisted of a modal analysis example, where the cross-sectional mode shapes of a cylindrical beam were investigated, in addition to a static large deformation cantilever example. Finally, a time-domain dynamic test was performed, in which the cross-sectional deformation (radial expansion) of a rotating shaft with a circular cross-section was studied. The commercial finite element software ANSYS was employed in the computation of the reference results. For the modal analysis and dynamic test, SOLID186 elements were used, while BEAM188 elements were used for the static test. In addition, an analytical formula describing the radial expansion of a rotating cylinder was used as a reference in the dynamic test.

The results computed using the investigated element show good agreement with the ANSYS results in both modal and static analyses. In addition, the time-domain dynamic test results agree well with both the ANSYS and analytical results. The rate of convergence of the higher order element in the transient test is illustrated in Fig. 3.8, showing (approximately) a third order convergence rate with respect to the total number of degrees of freedom.

In conclusion, the numerical tests validated the capability of the element to predict cross-sectional deformation and accurately capture the cross-sectional expansion of a rotating shaft. However, as the test cases consisted solely of cylindrical beams, the applications of the element to structures with different cross-sectional shapes should be studied further.

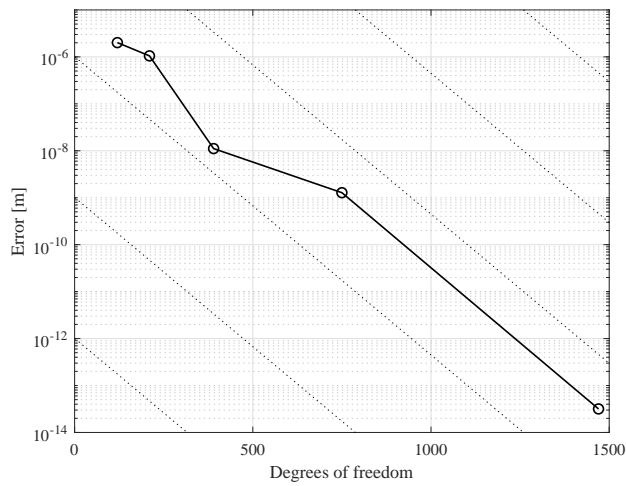


**Figure 3.8.** *Publication V:* convergence of radial deformation for higher order beam element 34X3. The error is defined in relation to the result computed using the highest number of elements (20). Diagonal dotted lines represent a third order rate of convergence.

## Conclusions

This dissertation discussed the simulation of flexibility in mechanical structures using finite elements based on the absolute nodal coordinate formulation. The absolute nodal coordinate formulation (ANCF) is a finite element-based formulation developed for modeling problems in multibody dynamics, wherein all nodal coordinates are defined in the inertial frame of reference. This leads to features such as a constant mass matrix and the elimination of the quadratic velocity vector, which are advantageous for numerical purposes. Describing elements using full continuum parametrization also enables the use of various material models defined in general continuum mechanics in a straightforward manner. However, various locking problems have previously been found to result from this type of definition, leading to investigations on different methods to avoid these problems.

Several planar and spatial beam and plate element formulations based on the ANCF were developed and numerically tested in the included publications. Many of the formulations developed can be categorized as higher-order elements. This element category was developed to avoid locking problems in elements employing three-dimensional elasticity by improving the ability of the elements to reproduce more complex deformation shapes. This is done by enriching the polynomial basis of the element and using higher-order derivatives as additional nodal coordinates.

The objective of the dissertation was to further the development of elements based on the absolute nodal coordinate formulation and apply them to the simulation of various types of mechanical structures. Element development was performed in *Publication I*, *Publication II* and *Publication III*. *Publication I* focused on a planar ANCF-based formulation with individual interpolation of shear deformation, while *Publication II* and *Publication III* focused on higher-order beam and plate elements, respectively. While all of the included publications included the application of the elements to various numerical experiments, *Publication IV* and *Publication V*

were the ones chiefly focused on applications. In these papers, lower and higher order ANCF-based elements were applied to problems of rotordynamics.

From the results presented in *Publication II*, *Publication III* and *Publication V*, it can be concluded that it is possible to avoid locking problems and produce accurate results in complex load cases when using higher-order ANCF-based plate elements and employing the linear hyperelastic St. Venant–Kirchhoff material model in the formulation of elastic forces. In the publications, these elements were tested in a wide variety of numerical experiments ranging from large deformation static cases to dynamic frequency-domain and time-domain cases, and they performed adequately. Therefore, the results provide proof that with regard to accuracy, these elements are applicable to the simulation of mechanical systems. In addition, the models created using these elements can, in certain applications, provide accuracy comparable to solid element models, but without their large computational requirements.

The results of *Publication IV* and *Publication V* showed the applicability of ANCF-based elements to problems of rotordynamics. In both publications, the employed elements were found to produce satisfactory results in modal and transient simulations. In addition, the proposed approach for computation of the Campbell diagrams was found to produce results corresponding to those produced using commercial software.

In conclusion, the higher-order ANCF-based elements have shown promising results in static and dynamic simulations in terms of both computational complexity and accuracy. They have been shown to result in computationally simpler models than solid elements while being able to reproduce more complex deformations than conventional or lower-order ANCF-based beam and plate elements. Further study and development of this type of formulation is, therefore, justified.

#### SUGGESTIONS FOR FUTURE WORK

There are several areas where the work presented in this dissertation could be continued. Some suggestions for future research topics regarding the ANCF-based elements are presented below.

The first topic is the extension of the planar element formulation presented in *Publication I* into a three-dimensional case. While the element formulation was shown to produce satisfactory results and some computational advantage compared to other formulations in the planar case, applications of planar elements in the simulation of physical problems are limited. Therefore, it should be investigated if the element could be extended to 3D and if the resulting spatial element would still produce a computational advantage.

Another topic for further research is finding the limits of the applicability of the proposed higher-order beam and plate elements. While the higher-order elements developed in *Publication II* and *Publication III* were already numerically tested to some extent, they were found to produce good results in all of the tested cases. However, all of the numerical cases were geometrically speaking somewhat simple, consisting mostly of uniform rectangular or cylindrical beams. It was suggested that the elements could possibly be used to model even more complex geometries than those used in the tests. For example, hollow shafts were put forward as an application.



- [1] ANSYS, INC. *Theory Reference for the Mechanical APDL and Mechanical Applications*. Canonsburg, Pennsylvania, USA, 2009.
- [2] BATHE, K.-J. *Finite Element Procedures*. Prentice–Hall, 2006.
- [3] BAUCHAU, O. A. *Flexible Multibody Dynamics*, 1st ed., vol. 176 of *Solid Mechanics and Its Applications*. Springer Netherlands, 2011.
- [4] BAUCHAU, O. A., BETSCH, P., CARDONA, A., GERSTMAYR, J., JONKER, B., MASARATI, P., AND SONNEVILLE, V. Validation of flexible multibody dynamics beam formulations using benchmark problems. *Multibody System Dynamics* 37, 1 (2016), 29–48.
- [5] BECHTEL, S. E., AND LOWE, R. L. Chapter 6 - nonlinear elasticity. In *Fundamentals of Continuum Mechanics*, S. E. Bechtel and R. L. Lowe, Eds. Academic Press, Boston, 2015, pp. 181 – 195.
- [6] BERZERI, M., AND SHABANA, A. Development of simple models for the elastic forces in the absolute nodal co-ordinate formulation. *Journal of Sound and Vibration* 235, 4 (2000), 539 – 565.
- [7] BOER, S. E., AARTS, R. G. K. M., MEIJAARD, J. P., BROUWER, D. M., AND JONKER, J. B. A nonlinear two-node superelement for use in flexible multibody systems. *Multibody System Dynamics* 31, 4 (2014), 405–431.
- [8] BUTCHER, J. C. *Numerical Methods for Ordinary Differential Equations*. John Wiley & Sons, 2008.
- [9] CRAIG, R. R. *Structural Dynamics: an Introduction to Computer Methods*. John Wiley & Sons, 1981.
- [10] DMITROCHENKO, O., AND MIKKOLA, A. Digital nomenclature code for topology and kinematics of finite elements based on the absolute nodal co-ordinate formulation. *Proceedings of the Institution of Mechanical Engineers, Part K: Journal of Multi-body Dynamics* 225, 1 (2011), 34–51.

- 
- [11] DOWELL, E. H., AND TRAYBAR, J. J. An experimental study of the nonlinear stiffness of a rotor blade undergoing flap, lag and twist deformations. Technical report, NASA, 1975.
- [12] FRISWELL, M. I., PENNY, J. E. T., GARVEY, S. D., AND LEES, A. W. *Dynamics of Rotating Machines*. Cambridge Aerospace Series. Cambridge University Press, 2010.
- [13] GERSTMAYR, J., MATIKAINEN, M. K., AND MIKKOLA, A. M. A geometrically exact beam element based on the absolute nodal coordinate formulation. *Multibody System Dynamics* 20, 4 (2008), 359–384.
- [14] GERSTMAYR, J., AND SHABANA, A. A. Efficient integration of the elastic forces and thin three-dimensional beam elements in the absolute nodal coordinate formulation. In *Multibody Dynamics 2005, ECCOMAS Thematic Conference* (Madrid, Spain, 21-24 June 2005).
- [15] GERSTMAYR, J., AND SHABANA, A. A. Analysis of thin beams and cables using the absolute nodal co-ordinate formulation. *Nonlinear Dynamics* 45, 1 (2006), 109–130.
- [16] GERSTMAYR, J., SUGIYAMA, H., AND MIKKOLA, A. Review on the absolute nodal coordinate formulation for large deformation analysis of multibody systems. *Journal of Computational and Nonlinear Dynamics* 8, 3 (2013).
- [17] MAQUEDA, L. G., AND SHABANA, A. A. Poisson modes and general nonlinear constitutive models in the large displacement analysis of beams. *Multibody System Dynamics* 18, 3 (2007), 375–396.
- [18] MATIKAINEN, M., DMITROCHENKO, O., AND MIKKOLA, A. Beam elements with trapezoidal cross section deformation modes based on the absolute nodal coordinate formulation. In *AIP Conference Proceedings* (2010), no. 1281, pp. 1266–1270.
- [19] MATIKAINEN, M. K., DMITROCHENKO, O., AND MIKKOLA, A. Higher order beam elements based on the absolute nodal coordinate formulation. In *Multibody Dynamics 2011, ECCOMAS Thematic Conference* (Brussels, Belgium, 4–7 July 2011).
- [20] MATIKAINEN, M. K., DMITROCHENKO, O., AND MIKKOLA, A. Higher order beam elements based on the absolute nodal coordinate formulation. *Multibody Dynamics* (2011).
- [21] MATIKAINEN, M. K., VALKEAPÄÄ, A. I., MIKKOLA, A. M., AND SCHWAB, A. L. A study of moderately thick quadrilateral plate elements based on the

- absolute nodal coordinate formulation. *Multibody System Dynamics* 31, 3 (2014), 309–338.
- [22] MIKKOLA, A., DMITROCHENKO, O., AND MATIKAINEN, M. Inclusion of transverse shear deformation in a beam element based on the absolute nodal coordinate formulation. *Journal of Computational and Nonlinear Dynamics* 4, 1 (2008).
- [23] MIKKOLA, A., AND SHABANA, A. A. A non-incremental finite element procedure for the analysis of large deformation of plates and shells in mechanical system applications. *Multibody System Dynamics* 9, 3 (2003), 283–309.
- [24] NACHBAGAUER, K. State of the art of ANCF elements regarding geometric description, interpolation strategies, definition of elastic forces, validation and the locking phenomenon in comparison with proposed beam finite elements. *Archives of Computational Methods in Engineering* 21, 3 (2014), 293–319.
- [25] NACHBAGAUER, K., GRUBER, P., AND GERSTMAYR, J. Structural and continuum mechanics approaches for a 3D shear deformable ancf beam finite element: Application to static and linearized dynamic examples. *Journal of Computational and Nonlinear Dynamics* 8, 2 (2012).
- [26] NACHBAGAUER, K., GRUBER, P., AND GERSTMAYR, J. A 3D shear deformable finite element based on the absolute nodal coordinate formulation. In *Multibody Dynamics: Computational Methods and Applications*, J.-C. Samin and P. Fiset, Eds. Springer Netherlands, Dordrecht, 2013, pp. 77–96.
- [27] NACHBAGAUER, K., PECHSTEIN, A. S., IRSCHIK, H., AND GERSTMAYR, J. A new locking-free formulation for planar, shear deformable, linear and quadratic beam finite elements based on the absolute nodal coordinate formulation. *Multibody System Dynamics* 26, 3 (2011), 245–263.
- [28] ORZECOWSKI, G., AND SHABANA, A. A. Analysis of warping deformation modes using higher order ANCF beam element. *Journal of Sound and Vibration* 363 (2016), 428–445.
- [29] SCHWAB, A. L., AND MEIJAARD, J. P. Comparison of three-dimensional flexible beam elements for dynamic analysis: classical finite element formulation and absolute nodal coordinate formulation. *Journal of Computational and Nonlinear Dynamics* 5, 1 (2009).
- [30] SHABANA, A. A. Flexible multibody dynamics: Review of past and recent developments. *Multibody System Dynamics* 1, 2 (1997), 189–222.

- 
- [31] SHABANA, A. A. *Dynamics of Multibody Systems*, 3rd ed. Cambridge University Press, 2005.
- [32] SHABANA, A. A., HUSSIEN, H. A., AND ESCALONA, J. L. Application of the absolute nodal coordinate formulation to large rotation and large deformation problems. *Journal of Mechanical Design* 120, 2 (1998), 188–195.
- [33] SHABANA, A. A., AND YAKOUB, R. Y. Three dimensional absolute nodal coordinate formulation for beam elements: theory. *Journal of Mechanical Design* 123, 4 (2000), 606–613.
- [34] SHEN, Z., LI, P., LIU, C., AND HU, G. A finite element beam model including cross-section distortion in the absolute nodal coordinate formulation. *Nonlinear Dynamics* 77, 3 (2014), 1019–1033.
- [35] SIMO, J. C. A finite strain beam formulation. The three-dimensional dynamic problem. Part I. *Computer Methods in Applied Mechanics and Engineering* 49, 1 (1985), 55–70.
- [36] SIMO, J. C., AND VU-QUOC, L. On the dynamics of flexible beams under large overall motions - the plane case: parts I and II. *Journal of Applied Mechanics* 53, 4 (1986), 849–863.
- [37] SOPANEN, J. T., AND MIKKOLA, A. M. Description of elastic forces in absolute nodal coordinate formulation. *Nonlinear Dynamics* 34, 1 (2003), 53–74.
- [38] VALKEAPÄÄ, A. I., MATIKAINEN, M. K., AND MIKKOLA, A. M. Meshing strategies in the absolute nodal coordinate formulation-based Euler-Bernoulli beam elements. *Proceedings of the Institution of Mechanical Engineers K, Journal of Multi-Body Dynamics* 230, 4 (2016), 606–614.
- [39] WASFY, T. M., AND NOOR, A. K. Computational strategies for flexible multibody systems. *Applied Mechanics Reviews* 56, 6 (2003), 553–613.
- [40] YAKOUB, R. Y., AND SHABANA, A. A. Three dimensional absolute nodal coordinate formulation for beam elements: implementation and applications. *Journal of Mechanical Design* 123, 4 (2000), 614–621.
- [41] YOO, W. S., AND HAUG, E. J. Dynamics of articulated structures. Part I. Theory. *Journal of Structural Mechanics* 14, 1 (1986), 105–126.

## Publication I

Hurskainen, V.-V., Matikainen, M.K., Wang, J., Mikkola, A.  
**A planar beam finite-element formulation with individually  
interpolated shear deformation**

Reprinted with permission from  
*Journal of Computational and Nonlinear Dynamics*  
Vol. 12(4), Paper No. CND-16-1313, January 2017  
© 2017, The American Society of Mechanical Engineers (ASME)



## Vesa-Ville T. Hurskainen

School of Energy Systems,  
Lappeenranta University of Technology,  
Skinnarilankatu 34,  
Lappeenranta 53851, Finland  
e-mail: vesa-ville.hurskainen@lut.fi

## Marko K. Matikainen

School of Energy Systems,  
Lappeenranta University of Technology,  
Skinnarilankatu 34,  
Lappeenranta 53851, Finland  
e-mail: marko.matikainen@lut.fi

## Jia J. Wang

School of Mechatronic Engineering,  
Harbin Institute of Technology,  
Harbin 150001, China  
e-mail: wangjia\_hit@163.com

## Aki M. Mikkola

School of Energy Systems,  
Lappeenranta University of Technology,  
Skinnarilankatu 34,  
Lappeenranta 53851, Finland  
e-mail: aki.mikkola@lut.fi

# A Planar Beam Finite-Element Formulation With Individually Interpolated Shear Deformation

*This paper introduces a new planar gradient deficient beam element based on the absolute nodal coordinate formulation. In the proposed formulation, the centerline position is interpolated using cubic polynomials while shear deformation is taken into account via independently interpolated linear terms. The orientation of the cross section, which is defined by the axial slope of the element's centerline position combined with the independent shear terms, is coupled with the displacement field. A structural mechanics based formulation is used to describe the strain energy via generalized strains derived using a local element coordinate frame. The accuracy and the convergence properties of the proposed formulation are verified using numerical tests in both static and dynamics cases. The numerical results show good agreement with reference formulations in terms of accuracy and convergence. [DOI: 10.1115/1.4035413]*

## 1 Introduction

Multibody system dynamics has established its position as a standard industrial tool for analyzing dynamic responses of complex systems. The reason for its popularity is the fact that multibody system dynamics offers a straightforward approach for defining the equations of motion for a wide variety of applications [1]. In its original form, multibody system dynamics was designed only to deal with interconnected rigid bodies [2]. Soon, however, designers realized that the accuracy and usability of the method can be improved by accounting for the mechanical flexibility of one or more of the bodies in the system.

Conventional finite elements of linear and nonlinear elastodynamics and, later, the floating frame of reference formulation and geometrically exact formulations (e.g., large rotation vector formulation) have been widely used to describe flexible bodies in dynamic analysis [3]. While conventional isoparametric continuum finite elements derived using the total or updated Lagrangian formulations can be successfully used in dynamic simulations of multibody applications, in lengthy simulations this approach leads to computationally expensive solutions due to the system's high number of degrees-of-freedom (DOFs) and high eigenfrequencies [4]. For this reason, the floating frame of reference formulation (used in conjunction with a coordinate reduction technique) becomes an often used approach in industrial applications. The floating frame of reference formulation employs a linear strain-displacement relation with respect to the noninertial reference frame. This leads to a computationally efficient approach, which can be used even in real-time applications [5]. This formulation is, however, difficult to apply to geometrically nonlinear problems.

To resolve this shortcoming, researchers have developed a number of formulations for large deformations, i.e., large

displacements and large strains, in dynamic simulations of multibody applications. The large rotation vector formulation uses independent interpolations for position and rotation fields and therefore leads to a coordinate redundancy problem that has to be avoided by employing quaternions. Due to these drawbacks, the absolute nodal coordinate formulation (ANCF) [6] has attracted interest within the multibody community with its simple kinematics description, combined with its characteristic ability to produce a constant mass matrix. In contrast to the large rotation vector formulation, the ANCF leads to a description of gradient fields instead of independent interpolations for position and rotation fields. This approach enables the description of cross-sectional or fiber deformations using components of the deformation gradient instead of rotational angles. Therefore, large reference rotations can be described without the singularity problems that may occur when using a three-dimensional rotation description in a total Lagrangian formulation. Due to the choice of generalized coordinates and use of the total Lagrangian formulation, the ANCF leads to straightforward implementation into a multibody code and produces a constant mass matrix, which is computationally beneficial when employing time integration schemes.

Different interpolation strategies and various locking phenomena occurring in ANCF elements are discussed in detail by Nachbagger [7]. In accordance with this paper, there are two main families of finite elements based on the ANCF. The first is comprised of conventional beam and plate elements, parameterized as centerlines or surfaces, that cannot capture such effects as transverse shear deformations. These elements are often called "gradient deficient" since the full position gradient is not represented in the chosen nodal coordinates [7]. The second family of elements employs transverse slope vectors, allowing them to reproduce effects like shear, cross-sectional, and fiber deformations. This, in turn, permits the relaxation of some assumptions made in Euler-Bernoulli and Timoshenko theories for beams or Kirchhoff-Love and Mindlin-Reissner theories for plates [8]. These elements are sometimes referred to as "fully parameterized." An interesting extension for shear-deformable ANCF-based

Contributed by the Design Engineering Division of ASME for publication in the JOURNAL OF COMPUTATIONAL AND NONLINEAR DYNAMICS. Manuscript received July 1, 2016; final manuscript received November 23, 2016; published online January 20, 2017. Assoc. Editor: José L. Escalona.

elements can be obtained by using higher-order derivatives to mitigate numerical locking phenomena (see, for example, Refs. [9,10]). The elastic forces must be defined with care because the use of full three-dimensional elasticity in conjunction with improper interpolations and choices of slope vectors has been demonstrated to be vulnerable to various locking phenomena.

In addition to “pure” ANCF elements, numerous hybrid element types have been developed, which include a combination of traits from the ANCF and other formulations. A planar beam example is the beam element introduced by Mikkola et al. [11], which uses a Timoshenko beam theory based approach for the inclusion of shear deformation. Another beam example, this time for a three-dimensional case, is the director-based Euler-Bernoulli element presented by Gruber et al. [12], which employs rotational degrees-of-freedom for torsion. A plate-type example is the large deformation plate element by Mikkola and Matikainen [13], which employs fiber rotations. While these hybrid types do not necessarily result in a constant mass matrix, if the variance is limited enough, a constant matrix can serve well as an approximation.

This paper introduces a new hybrid element type as an alternative approach to the ones mentioned above. The basis of the introduced formulation is a two-dimensional gradient deficient beam element that is enriched by using independent interpolation for shear deformation. This independently interpolated shear approach differs from previous formulations, as neither the commonly used transverse slopes nor the moment equilibrium equations used, e.g., in Ref. [11], are employed to capture shear deformation. Instead, shear deformation is described using an independent vector, the components of which are linearly interpolated between nodes. The present formulation can therefore be considered as an alternative approach to account for shear deformation in a centerline-parameterized element and seen as a combination of the absolute nodal coordinate formulation and the large rotation vector formulation.

First, the proposed element is explained in detail, including element kinematics and shape functions, in addition to the description of elastic and inertial forces. Then, the performance of the introduced element is demonstrated using various numerical examples and compared to the computationally efficient three-node quadratic beam element proposed by Nachbagauer et al. [14]. Numerical results demonstrate good convergence properties and accuracy in both static and dynamic cases.

## 2 Element Description

In this section, the individually interpolated shear approach is explained in detail. To this end, element shape functions are presented in addition to the element’s description of elastic and inertial forces. To shed light on the introduced formulation and its relation to the ANCF, the original gradient deficient beam element is also presented.

**2.1 ANCF-Based Gradient Deficient Beam Element.** A planar gradient deficient ANCF-based beam element (adapted from Ref. [11]) is presented in Fig. 1. The element consists of two nodes ( $i, j$ ), and the centerline position is defined by vector  $\mathbf{r}$ . The centerline position between nodes can be interpolated using cubic polynomials as

$$\mathbf{r} = \begin{bmatrix} r_1 \\ r_2 \end{bmatrix} = \begin{bmatrix} a_0 + a_1x + a_2x^2 + a_3x^3 \\ b_0 + b_1x + b_2x^2 + b_3x^3 \end{bmatrix} \quad (1)$$

where  $x \in [0, L]$  is the arc coordinate along the centerline, and  $a_0 \dots a_3$  and  $b_0 \dots b_3$  are the polynomial coefficients. Selecting position vector  $\mathbf{r}$  and slope vector  $\mathbf{r}_{,x}$  (partial derivative of  $\mathbf{r}$  with respect to  $x$ ) as nodal coordinates yields four nodal degrees-of-

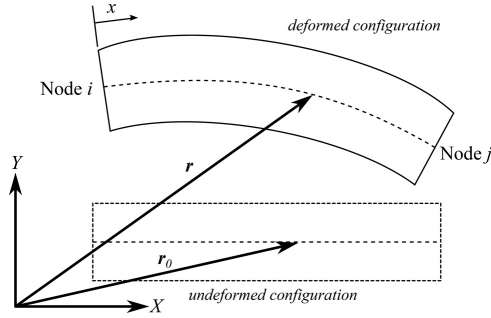


Fig. 1 Two-node ANCF-based beam element

freedom at a nodal location. The vector of nodal coordinates  $\mathbf{e}$  can be written as

$$\mathbf{e} = [\mathbf{e}_i^T \quad \mathbf{e}_j^T]^T = [\mathbf{r}_i^T \quad \mathbf{r}_{i,x}^T \quad \mathbf{r}_j^T \quad \mathbf{r}_{j,x}^T]^T \quad (2)$$

$$= [r_{i1} \quad r_{i2} \quad r_{i1,x} \quad r_{i2,x} \quad r_{j1} \quad r_{j2} \quad r_{j1,x} \quad r_{j2,x}]^T$$

The shape functions of the element can easily be derived from Eqs. (1) and (2). The shape function matrix  $\mathbf{S}$  can be written as

$$\mathbf{S} = \begin{bmatrix} S_1 & 0 & S_2 & 0 & S_3 & 0 & S_4 & 0 \\ 0 & S_1 & 0 & S_2 & 0 & S_3 & 0 & S_4 \end{bmatrix} \quad (3)$$

where (using the definition  $\xi = x/L$ ) individual shape functions  $S_{1 \dots 4}$  are written as

$$S_1 = 1 - 3\xi^2 + 2\xi^3 \quad S_3 = 3\xi^2 - 2\xi^3$$

$$S_2 = L(\xi - 2\xi^2 + \xi^3) \quad S_4 = L(-\xi^2 + \xi^3)$$

Now, the centerline position vector defined in Eq. (1) can be rewritten as

$$\mathbf{r} = \mathbf{S}\mathbf{e} \quad (4)$$

**2.2 Beam Element Based on Independently Interpolated Shear Approach.** A modified beam element is depicted in Fig. 2. As illustrated in the figure, the orientation (normal direction) of the cross-sectional plane of the modified element is described using vector  $\mathbf{t}$ , which can be defined as follows:

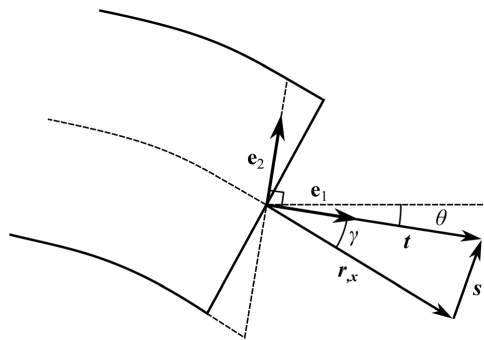


Fig. 2 Description of shear deformation and cross section orientation for the proposed element

$$\mathbf{t} = \frac{\partial \mathbf{r}}{\partial x} + \mathbf{s} = \mathbf{r}_{,x} + \mathbf{s} \quad (5)$$

In this formulation, the effect of shear deformation is accounted for by the use of shear deformation vector  $\mathbf{s}$ , which describes the change caused by shear in the orientation of the cross-sectional plane of the beam. A linear polynomial interpolation is used for the components of this vector, with coefficients  $c_0, c_1, d_0$ , and  $d_1$ . This yields the definition

$$\mathbf{s} = \begin{bmatrix} s_1 \\ s_2 \end{bmatrix} = \begin{bmatrix} c_0 + c_1 x \\ d_0 + d_1 x \end{bmatrix} \quad (6)$$

It should be noted that while the definition of cross section orientation is similar to Ref. [11], this formulation does not use the equation of moment equilibrium in the inclusion of shear deformation. Components of position vector  $\mathbf{r}$  can be interpolated in the same way as shown before, using cubic polynomials with coefficients  $a_0 \dots a_3$  and  $b_0 \dots b_3$ . Substituting Eqs. (1) and (6) into Eq. (5), cross section orientation vector  $\mathbf{t}$  can be rewritten as

$$\mathbf{t} = \begin{bmatrix} t_1 \\ t_2 \end{bmatrix} = \begin{bmatrix} a_1 + c_0 + (2a_2 + c_1)x + 3a_3 x^2 \\ b_1 + d_0 + (2b_2 + d_1)x + 3b_3 x^2 \end{bmatrix} \quad (7)$$

Selecting the vectors of position ( $\mathbf{r}$ ), orientation ( $\mathbf{t}$ ), and shear deformation ( $\mathbf{s}$ ) as nodal coordinates leads to six nodal degrees-of-freedom. This amounts to 12 degrees-of-freedom in total, which is the same as the total number of polynomial coefficients. The new vector of nodal coordinates  $\mathbf{q}$  can be written as

$$\mathbf{q} = [\mathbf{q}_i^T \quad \mathbf{q}_j^T]^T = [\mathbf{r}_i^T \quad \mathbf{t}_i^T \quad \mathbf{s}_i^T \quad \mathbf{r}_j^T \quad \mathbf{t}_j^T \quad \mathbf{s}_j^T]^T = [r_{i1} \quad r_{i2} \quad t_{i1} \quad t_{i2} \quad s_{i1} \quad s_{i2} \quad r_{j1} \quad r_{j2} \quad t_{j1} \quad t_{j2} \quad s_{j1} \quad s_{j2}]^T \quad (8)$$

Combining Eqs. (1), (7), and (8), the shape functions of the element can be solved. The shape function matrix  $\mathbf{S}_r$  associated with centerline translation  $\mathbf{r}$  can be written as

$$\mathbf{S}_r = \begin{bmatrix} S_{r1} & 0 & S_{r2} & 0 & S_{r3} & 0 & S_{r4} & 0 & S_{r5} & 0 & S_{r6} & 0 \\ 0 & S_{r1} & 0 & S_{r2} & 0 & S_{r3} & 0 & S_{r4} & 0 & S_{r5} & 0 & S_{r6} \end{bmatrix} \quad (9)$$

where (using the definition  $\xi = x/L$ ) individual shape functions  $S_{r1 \dots r6}$  are written as

$$\begin{aligned} S_{r1} &= 1 - 3\xi^2 + 2\xi^3 & S_{r4} &= 3\xi^2 - 2\xi^3 \\ S_{r2} &= L(\xi - 2\xi^2 + \xi^3) & S_{r5} &= L(-\xi^2 + \xi^3) \\ S_{r3} &= L(-\xi + 2\xi^2 - \xi^3) & S_{r6} &= L(\xi^2 - \xi^3) \end{aligned}$$

The shape function matrix  $\mathbf{S}_t$  associated with cross section orientation vector  $\mathbf{t}$  can be written as

$$\mathbf{S}_t = \begin{bmatrix} S_{t1} & 0 & S_{t2} & 0 & S_{t3} & 0 & S_{t4} & 0 & S_{t5} & 0 & S_{t6} & 0 \\ 0 & S_{t1} & 0 & S_{t2} & 0 & S_{t3} & 0 & S_{t4} & 0 & S_{t5} & 0 & S_{t6} \end{bmatrix} \quad (10)$$

where (using the definition  $\xi = x/L$ ) individual shape functions  $S_{t1 \dots t6}$  are written as

$$\begin{aligned} S_{t1} &= \frac{1}{L}(-6\xi + 6\xi^2) & S_{t4} &= \frac{1}{L}(6\xi - 6\xi^2) \\ S_{t2} &= 1 - 4\xi + 3\xi^2 & S_{t5} &= -2\xi + 3\xi^2 \\ S_{t3} &= 3\xi - 3\xi^2 & S_{t6} &= 3\xi - 3\xi^2 \end{aligned}$$

Now, definitions for vectors  $\mathbf{r}$  and  $\mathbf{t}$  can be rewritten as

$$\mathbf{r} = \mathbf{S}_r \mathbf{q} \quad (11)$$

$$\mathbf{t} = \mathbf{S}_t \mathbf{q} \quad (12)$$

A constant-shear variant of the proposed element can also be formulated by using constants as interpolation functions in Eq. (6), reducing element degrees-of-freedom by two. This variant is in many ways comparable to the shear inclusion element presented by Mikkola et al. [11], the main differences being the absence of the equation of moment equilibrium as a constraint and the choice of nodal degrees-of-freedom. However, in comparison to the linear-shear element presented here, the constant-shear variant shows considerably inferior convergence properties. Also, due to the fact that the constant-shear elements cannot share shear DOFs with neighboring elements, using this variant reduces the system DOFs very little compared to the better-performing linear-shear element. As a result of these considerations, the constant-shear variant will not be discussed further in this paper.

**2.3 Strain Description.** In this section, strains for the proposed element are defined by applying the formulation introduced by Simo and Vu-Quoc [15,16] based on Reissner's nonlinear rod theory [17]. Three generalized strain components are defined: axial strain  $\Gamma_1$ , shear strain  $\Gamma_2$ , and bending strain  $K$ . To help define these strains, a local element coordinate system (function of  $x$ ) is defined using base vectors  $\mathbf{e}_1$  and  $\mathbf{e}_2$

$$\mathbf{e}_1 = \frac{\mathbf{t}}{\|\mathbf{t}\|}, \quad \mathbf{e}_2 = \bar{\mathbf{I}}\mathbf{e}_1 = \frac{\bar{\mathbf{I}}\mathbf{t}}{\|\mathbf{t}\|} = \frac{1}{\|\mathbf{t}\|} \begin{bmatrix} -t_2 \\ t_1 \end{bmatrix} \quad (13)$$

where  $\bar{\mathbf{I}}$  is a transformation matrix describing a 90 deg counter-clockwise rotation. Here,  $\mathbf{e}_1$  describes the cross section normal (axial) direction and  $\mathbf{e}_2$  the corresponding transverse direction. Generalized strains of the element can now be defined with vector operations between the local coordinate system base vectors and the vectors describing cross section deformation (see Fig. 2). Using this method, beam axial strain  $\Gamma_1$  can be defined simply as

$$\Gamma_1 = \mathbf{e}_1^T \mathbf{r}_{,x} - 1 \quad (14)$$

Transverse shear strain  $\Gamma_2$  can, in turn, be defined as

$$\Gamma_2 = \mathbf{e}_2^T \mathbf{r}_{,x} \quad (15)$$

Finally, bending strain  $K$  can be defined as

$$K = \frac{d\theta}{dx} = \frac{t_1 t_{2,x} - t_2 t_{1,x}}{t_1^2 + t_2^2} = \frac{\mathbf{t} \times \mathbf{t}_{,x}}{\|\mathbf{t}\|^2} \quad (16)$$

where  $\mathbf{t}_{,x}$  denotes a derivative of  $\mathbf{t}$  with respect to  $x$ .

**2.4 Elastic Forces.** According to Simo and Vu-Quoc [15,16], the strain energy  $U$  can be calculated using the previously defined generalized strains, yielding the equation

$$U_0 = \frac{1}{2} \int_0^L (EA\Gamma_1^2 + k_s GA\Gamma_2^2 + EI_t K^2) dx \quad (17)$$

where  $A$  is the cross-sectional area,  $I_t$  is the square moment of inertia,  $E$  is the Young's modulus,  $G$  is the shear modulus, and  $k_s$  is the shear correction factor. In addition, an artificial penalty term is used and defined as

$$U_{\text{penalty}} = \frac{1}{2} \int_0^L k_p E_p^2 dx \quad (18)$$

where  $k_p$  is the penalty factor, and  $E_p = \mathbf{t}^T \mathbf{t} - 1$ . This term is required since none of the generalized strains used in the calculation of elastic forces (formulated according to Simo and Vu-Quoc

[15,16]) includes the length of the vector  $\mathbf{t}$ , only the direction, effectively making its length arbitrary with regard to the elastic forces. This can cause computational problems, and therefore, an artificial stiffness (penalty factor  $k_p$ ) is assigned to vector  $\mathbf{t}$  to keep its length near unit length. The total strain energy  $U$  can now be written as

$$U = U_0 + U_{\text{penalty}} \quad (19)$$

Elastic force vector  $\mathbf{F}_e$  can be calculated by partial differentiation of the strain energy with respect to nodal coordinates  $q$ , or as

$$\mathbf{F}_e = \begin{bmatrix} \frac{\partial U}{\partial q_1} & \frac{\partial U}{\partial q_2} & \cdots & \frac{\partial U}{\partial q_{12}} \end{bmatrix}^T \quad (20)$$

**2.5 Inertial Forces.** This section presents the inertial force equations for the proposed element. Arbitrary position  $p$  within the beam can be defined using the equation

$$\mathbf{r}_p = \mathbf{r} + y\mathbf{e}_2 \quad (21)$$

where coordinate  $y$  denotes the transverse distance from the beam centerline (measured within the cross-sectional plane). Using this definition, the total kinetic energy equation of the element can be written as

$$T = \frac{1}{2} \int_V \rho \dot{\mathbf{r}}_p^T \dot{\mathbf{r}}_p dV \quad (22)$$

where  $\rho$  is the material density, and  $\dot{\mathbf{r}}_p$  denotes the time derivative of  $\mathbf{r}_p$ . Deriving from Eq. (21),  $\dot{\mathbf{r}}_p$  yields the definition

$$\dot{\mathbf{r}}_p = \dot{\mathbf{r}} + y\dot{\mathbf{e}}_2 = \dot{\mathbf{r}} + y \frac{\dot{\mathbf{I}}}{\|\mathbf{t}\|} \left( \mathbf{I} - \frac{\mathbf{t}\mathbf{t}^T}{\|\mathbf{t}\|^2} \right) \mathbf{i} \quad (23)$$

where  $\mathbf{I}$  is a  $2 \times 2$  identity matrix. The mass matrix of the element can be written as

$$\mathbf{M} = \mathbf{M}_r + \mathbf{M}_t \quad (24)$$

where  $\mathbf{M}_r$  and  $\mathbf{M}_t$  denote the parts of the matrix pertaining to vectors  $\mathbf{r}$  and  $\mathbf{t}$ , respectively. Deriving from Eq. (22), these matrices can be written as

$$\begin{aligned} \mathbf{M}_r &= \int_0^L \rho A \mathbf{S}_r^T \mathbf{S}_r dx \\ \mathbf{M}_t &= \int_0^L \rho I_z \frac{\mathbf{S}_t^T \dot{\mathbf{I}} \mathbf{t} \mathbf{t}^T \mathbf{S}_t}{\|\mathbf{t}\|^4} dx \end{aligned} \quad (25)$$

Notably, this definition implies that  $\mathbf{M}_t$  is dependent on the length of vector  $\mathbf{t}$  and thus time-variant. However, due to the penalty term included in the strain energy, vector  $\mathbf{t}$  should remain very close to unit length in most situations. Therefore, the mass matrix can be approximated as constant without much loss of accuracy, a notion supported by computational results.

### 3 Numerical Examples

To collect data about the performance of the introduced formulation, the element presented in Sec. 2 was implemented using MATLAB. Static and dynamic analysis examples, in addition to eigenmode analysis, have been computed using numerical methods. The results have been compared to a set of reference results.

Regarding the penalty factor  $k_p$  in Eq. (18), while convergence may be slightly improved by optimization (i.e., finding the minimum value with no errors), this was not the focus of this study. It was instead attempted to find a universal value that produces no

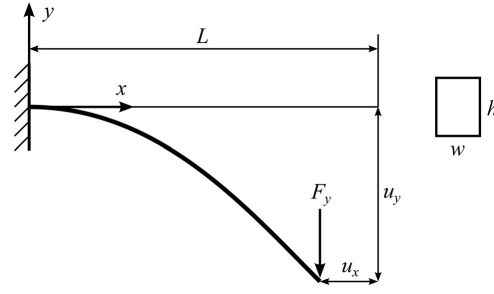


**Fig. 3 Static example: geometry and load description of a cantilever beam of length  $L$  under vertical tip load  $F_y$**

errors in any scenario. The value  $k_p = AE$  was not observed to produce problems in any of the tests, and therefore, this value was used for all the presented results.

**3.1 Static Analysis.** To test the static loading properties of the element, the large deformation cantilever example presented in Fig. 3 was calculated using MATLAB. The same example is featured in several papers on ANCF elements (e.g., see Refs. [14,18]), thus providing comparable data. The material, geometrical, and load parameters presented in Table 1 were used in the analysis, which was performed several times with incrementally finer lengthwise element divisions to investigate the element's convergence properties. In each successive step, the previous element number was doubled.

The computed beam tip displacements are presented for a small deformation case (small tip load) in Table 2 and for a large deformation case (large tip load) in Table 3. Converged results calculated using the computationally efficient three-node quadratic element formulation by Nachbagauer et al. [14] and the original geometrically exact formulation by Simo and Vu-Quoc [15,16] are used as reference results. Penalty factor value  $k_p = AE$  was used in the calculation of the tabulated results. Two settings were used for numerical integration: an exact integration scheme (a sufficiently large number of integration points) and a reduced integration scheme, using three-point Lobatto quadrature for the penalty term and three-point Gauss quadrature for other strain energy terms.

This reduced integration scheme was included for comparison since the scheme was observed to result in improved convergence in the large deformation case. While a Gaussian quadrature may be used for all the terms, the element was observed to converge particularly well when using a third-order Lobatto quadrature. It is the understanding of the authors that this is a result of the way integration points which are chosen in the Lobatto quadrature:

**Table 1 Static example: material, geometric, and load parameters for a cantilever beam [18]**

Material property	Symbol	Value
Young's modulus	$E$	$2.07 \times 10^{11}$ Pa
Shear modulus	$G$	$7.9615 \times 10^{10}$ Pa
Poisson's ratio	$\nu$	0.3
Shear correction factor	$k_s$	$\frac{10(1+\nu)}{12+11\nu} = 0.8497$
Geometric property		
Length ( $x$ )	$l$	2 m
Height ( $y$ )	$h$	0.5 m
Width ( $z$ )	$w$	0.1 m
Load property		
Tip load (small def.)	$F_y$	$5h^3 \times 10^5$ N
Tip load (large def.)	$F_y$	$5h^3 \times 10^8$ N

**Table 2 Static small deformation case: numerical results of beam free end displacement**

Elements	#	Displacement, $u_x$ (m) $\times 10^{-6}$	Displacement, $u_y$ (m) $\times 10^{-3}$
Proposed element: exact int.	1	0.188849046	0.809902993
	2	0.188849162	0.809903247
	4	0.188849164	0.809903254
	8	0.188849164	0.809903254
Proposed element: reduced int.	1	0.188849163	0.809903251
	2	0.188849164	0.809903253
	4	0.188849165	0.809903254
	8	0.188849165	0.809903254
References (converged)			
Nachbagauer et al. [14] quadr.		0.188849164	0.809903254
Simo-Vu Quoc [15,16], computed by Gerstmayr et al. [18]		0.18884916	0.80990325
ANSYS BEAM188		0.18932521	0.81023560

**Table 3 Static large deformation case: numerical results of beam free end displacement**

Elements	#	Displacement, $u_x$ (m)	Displacement, $u_y$ (m)
Proposed element: exact int.	1	0.119582605	0.631068073
	2	0.149526094	0.706435119
	4	0.150939303	0.710475908
	8	0.150970476	0.710566844
	16	0.150971124	0.710568558
	32	0.150971143	0.710568596
	64	0.150971144	0.710568598
	128	0.150971144	0.710568598
Proposed element: reduced int.	1	0.150017279	0.707508295
	2	0.150794796	0.710069017
	4	0.150965259	0.710554362
	8	0.150970898	0.710568150
	16	0.150971131	0.710568578
	32	0.150971143	0.710568597
	64	0.150971144	0.710568598
	128	0.150971144	0.710568598
References (converged)			
Nachbagauer et al. [14] quadr.		0.150971144	0.710568598
Simo-Vu Quoc [15,16], computed by Gerstmayr et al. [18]		0.15097114	0.71056859
ANSYS BEAM188		0.15162964	0.71143170

when using a third-order quadrature, the integration points are located at the midpoint and both endpoints of the element. These particular points appear to be advantageous for enforcing the artificial constraint represented by the penalty term, and in light of the results, using more than three points is unnecessary for the sake of avoiding computational errors. The reduced scheme was only applied to the static example.

The element shows good convergence, both integration schemes produce large deformation results that are converged to at least five significant figures with as few as eight elements. Even a single element provides an acceptable result in the small deformation case for both schemes. However, it seems that while the reduced integration scheme shows better results for low element numbers in the large deformation case, it also shows slightly reduced accuracy in the small deformation case.

In Fig. 4, the element's convergence properties in the large deformation case are compared further. Again, the three-node quadratic beam element presented by Nachbagauer et al. [14] is used as a reference element. For the reference element, a three-point Lobatto quadrature was used for the thickness term of the strain energy, while a two-point Gauss quadrature was used for the other terms. These settings produce results that correspond with those presented in Ref. [14]. For a second reference set, the example was computed in the commercial software ANSYS using the element BEAM188, which is based on geometrically exact theory. For all the elements, the relative error was calculated as the difference between successive results, or with the equation

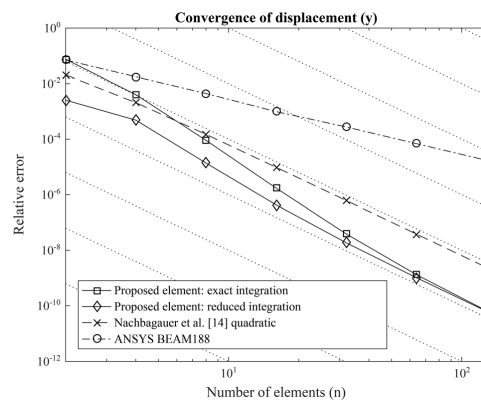


**Fig. 4 Comparison of static response: convergence of the vertical displacement of the free end of a beam in a large deformation case. Dotted reference lines indicate a convergence rate of  $O(n^4)$ . The relative error is calculated according to Eq. (26).**

**Table 4 Eigenfrequencies of the simply supported beam**

Elements	First bending	Second bending	First shear	Second shear	First axial	Second axial
1	105.148	484.420	1766.99	1896.70	281.174	983.712
2	96.0396	358.979	1766.99	1897.20	280.385	859.482
4	95.6592	333.816	1766.99	1879.05	280.324	842.087
8	95.6356	332.324	1766.99	1878.90	280.321	841.022
16	95.6341	332.240	1766.99	1878.87	280.321	840.965
32	95.6340	332.235	1766.99	1878.87	280.321	840.962
64	95.6340	332.235	1766.99	1878.87	280.321	840.962
Analytical	95.6340	332.235	1766.99	1878.87	280.321	840.962

**Table 5 Dynamic example: geometric, material, and load parameters for free beam [15,16]**

Parameter	$EA$	$GAK$	$EI$	$A\rho$	$I\rho$	$M$	$F$
Value (SI units)	$1 \times 10^4$	$1 \times 10^4$	100	1	10	80	$M/10$

$$Err(n) = |\text{Sol}(n) - \text{Sol}(n - 1)| \quad (26)$$

where  $\text{Sol}(n)$  is the solution with element number  $2^n$  and  $n = 1 \dots 7$ . Errors were calculated in this way to avoid problems caused by the numerical precision of the reference value when using a logarithmic scale. For the same reason, the figure uses a higher precision for values than was deemed practical to be presented in Tables 2 and 3.

The figure reveals that the proposed element shows better convergence properties than either reference element in the examined large deformation case, with the reduced scheme showing a consistently smaller error and the exact scheme showing a greater rate of convergence (although, initially, a larger error) than the element by Nachbagauer et al. It should also be noted that the higher rate of convergence of the exact integration scheme allows the scheme to “catch up” with the reduced one with larger element numbers, leading to both schemes producing the same amount of error.

**3.2 Eigen Frequencies of the Simply Supported Beam.** The second numerical test is an eigenfrequency analysis with simply supported boundaries, previously studied, e.g., in Ref. [18]. The eigenfrequency analysis is used as a linearized dynamics test because it offers the advantage of coordinate-free frequency and vibration mode comparisons. The numerical values of the parameters are adopted from Ref. [18] as follows: length  $L = 2$  m, width  $W = 0.4$  m, height  $H = 0.4$  m, Young’s modulus  $E = 1 \times 10^9$  N/m<sup>2</sup>, density  $\rho = 7850$  kg/m<sup>3</sup>, shear modulus  $G = E/2(1 + \nu)$ , transverse shear correction factors  $k_s = 10(1 + \nu)/(12 + 11\nu)$ , and Poisson’s ratio  $\nu = 0.3$ . The eigenfrequencies of a simply supported beam, solved with the proposed beam element, are presented in Table 4. The reference solutions are defined analytically by using the Timoshenko beam theory (see, e.g., Ref. [18]). It is apparent from Table 4 that when the element number is 32 or higher the first two bending, shear and axial modes of the proposed beam element agree with the Timoshenko solution within six digits.

**3.3 Dynamic Analysis.** In the third and final numerical example, the dynamics of a highly flexible beam is studied. The studied example, designated as the “flying spaghetti problem” was originally introduced by Simo and Vu-Quoc [15,16]. This problem has been used by Gerstmayr et al. [18] for comparing the ANCF to the implementation of Reissner’s geometrically exact beam theory presented by Simo and Vu-Quoc in Ref. [15,16]. As the example is sensitive to all the parameters in the elastic forces and the inertia, it is suitable for validating the dynamic performance of the proposed formulation. The geometric and material parameters

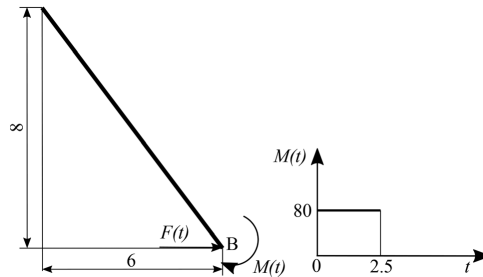


**Fig. 5 Dynamic example: geometry and load description of the free beam [15,16]**

used in the calculation are shown in Table 5. Figure 5 is a sketch of the free beam geometry with a description of the loads applied. It is worth noting that the parameters used in inertia are not consistent with those used in elastic forces and that the shear correction factor is set to  $k_s = 1$ . In addition to the proposed element, the flying spaghetti problem was solved with some reference formulations [14–16,18] to acquire data for comparison. The solution based on the proposed element is calculated with penalty factor value  $k_p = AE = 10^4$  and solver ODE45. As presented in the figure, loads are applied at point B from time 0 to 2.5 s and then set to zero. The total simulation time was set at 10 s.

A dynamic solution was computed using 24 of the proposed elements, resulting in a total of 150 DOFs. Four reference result sets were used for the verification of these dynamic results. The first was the original set of results by Simo and Vu-Quoc [15,16]. The second set was computed using the geometrically exact ANCF beam element by Gerstmayr et al. [18] (64 elements and 390 DOFs), which is based on Simo–Vu-Quoc strain energy. A solution obtained using the commercial software ANSYS with element type BEAM188 (64 elements and  $2 \times 195$  DOFs) was used as the third set. Finally, results computed using the quadratic element by Nachbagauer et al. [14] (24 elements and 196 DOFs) were used as the fourth reference set. A comparison of results is presented in Fig. 6 and Table 7.

As Fig. 6 shows that the differences between the responses of the compared elements are not large. The differences are further illustrated in Fig. 7, using the element by Gerstmayr et al. as a reference. It is observed that ANSYS BEAM188 produces the largest difference. This may be caused by the fact that BEAM188 is a spatial (3D) element, unlike all other elements compared here, which are planar. The difference could also result from the deformation of the cross section, which was restrained in BEAM188. As can be seen from this figure, the results of the proposed element agree with the chosen reference set better than the results of the element by Nachbagauer et al. In the absence of empirical results, however, it is difficult to say which reference values correspond best to reality. In a broader sense, as Fig. 6 shows that all of the elements compared here produce similar results.

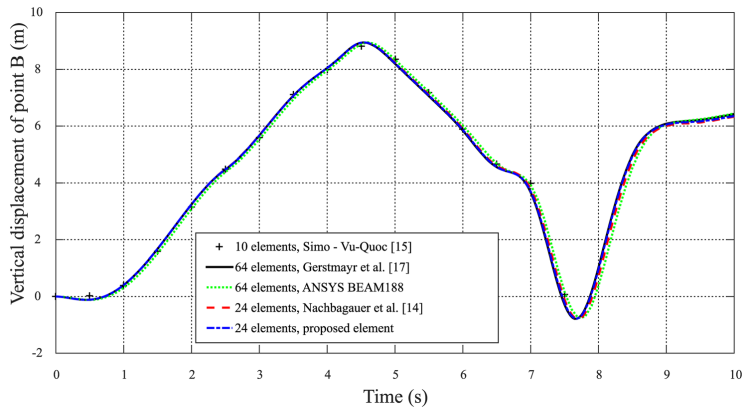


Fig. 6 Comparison of dynamic response: vertical position of point B versus time

Table 6 Dynamic example: comparison of computational effort

	Nachbagauer et al. [14]	Proposed element
Element number	24	24
DOFs	196	150
Time spent (s)	1484.9	742.7
Function evaluations	132,619	96,757
Integration steps	19,803	14,895
Relative tolerance	$1 \times 10^{-3}$	$1 \times 10^{-3}$
Absolute tolerance	$1 \times 10^{-6}$	$1 \times 10^{-6}$

The performance of the proposed element is further compared to that of the quadratic element of Nachbagauer et al. in terms of computational effort in Table 6 and in terms of convergence properties in Table 7. For Table 6, an approximation of the effort required for the calculation of the dynamic example was recorded by capturing the solution data from MATLAB. Table 7 illustrates the

Table 7 Comparison of dynamic response: vertical displacement of point B at  $t = 10$  s, along with relative error calculated according to Eq. (26)

Elements	Displacement, $u_y$ (m)	Rel. error (m)
Proposed element	8	6.89216
	16	6.35253
	32	6.35891
	64	6.36389
Nachbagauer et al. [14]	8	5.33068
	16	6.77298
	32	6.25839
	64	6.22635
Ref.: ANSYS BEAM188	64	6.41238
Ref.: Gerstmayr et al. [18]	64	6.4258

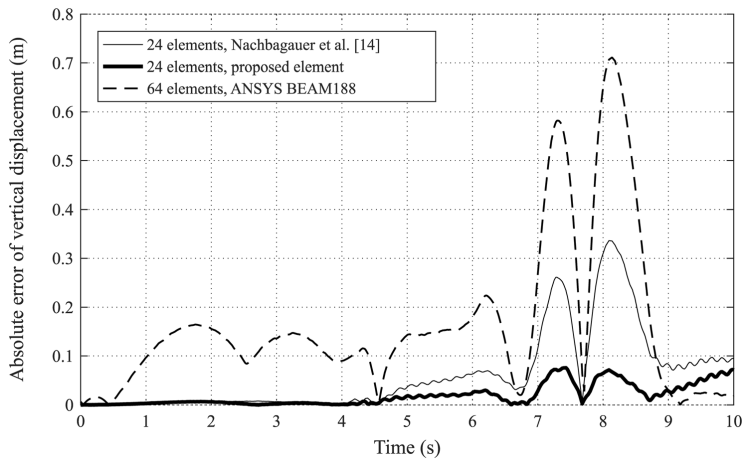


Fig. 7 Comparison of dynamic response: absolute error of vertical displacement of point B versus time. The reference set is composed of results computed using the element formulation by Gerstmayr et al. [18].

two elements' convergence properties by way of the end-time displacements of point B with incrementally larger numbers of elements, with relative error again calculated using Eq. (26) with  $n = 4 \dots 6$ . The data in Table 6 show that the numbers of function evaluations and integration steps, as well as the amount of time spent, are smaller for the proposed element. Furthermore, the relative error values presented in Table 7 are consistently smaller for the proposed element. Also, the displacement result obtained with the proposed element at  $t = 10$  s is closer to the values obtained using ANSYS and the formulation by Gerstmayr et al. [18] than the corresponding result obtained using the element by Nachbagauer et al.

#### 4 Summary and Conclusions

In this investigation, a planar beam finite element with independently interpolated shear deformation is introduced. In the proposed formulation, the centerline of the beam is interpolated by cubic polynomials, while shear deformation is taken into account via independently interpolated linear terms. The orientation of the element's cross section, which is defined by the axial slope of the centerline position combined with the independent shear terms, is coupled with the displacement field. Generalized strains are defined using two base vectors, which are derived from the orientation of the cross section, thus forming a local cross-sectional coordinate system. Strain energy is written based on the structural mechanics formulation with generalized strains, and an additional penalty term is added to the total strain energy to prevent computational errors. Finally, elastic forces are obtained from the variation of the strain energy with respect to the nodal coordinates.

The accuracy and convergence properties of the introduced element are verified using numerical examples in both static and dynamic cases. A cantilever beam under linear small deformation and nonlinear large deformation is used as the static example. The numerical results of the static example reveal that the proposed element shows good accuracy and convergence properties. Second, an eigenmode analysis for a simply supported beam is computed. The results of this test agree well with the analytical reference solution. Finally, as a large deformation dynamics case, an example known as the flying spaghetti problem is computed. These dynamic results also show that the proposed element agrees well with a geometrically exact reference formulation.

#### References

- [1] Schiehlen, W., 1997, "Multibody System Dynamics: Roots and Perspectives," *Multibody Syst. Dyn.*, **1**, pp. 149–188.
- [2] Schiehlen, W., 1990, *Multibody Systems Handbook*, Springer Verlag, Berlin.
- [3] Wasfy, T. M., and Noor, A. K., 2003, "Computational Strategies for Flexible Multibody Systems," *Appl. Mech.*, **56**(6), pp. 553–613.
- [4] Nowakowski, C., Fehr, J., Fischer, M., and Eberhard, P., 2012, "Model Order Reduction in Elastic Multibody Systems Using the Floating Frame of Reference Formulation," *IFAC Proc. Vol.*, **45**(2), pp. 40–48.
- [5] Baharudin, M. E., Korkealaakso, P., Rouvinen, A., and Mikkola, A., 2012, "Crane Operators Training Based on the Real-Time Multibody Simulation," *Multibody System Dynamics, Robotics and Control*, Springer, Vienna, Austria, pp. 213–229.
- [6] Shabana, A. A., 1997, "Definition of the Slopes and the Finite Element Absolute Nodal Coordinate Formulation," *Multibody Syst. Dyn.*, **1**(3), pp. 339–348.
- [7] Nachbagauer, K., 2014, "State of the Art of ANCF Elements Regarding Geometric Description, Interpolation Strategies, Definition of Elastic Forces, Validation and the Locking Phenomenon in Comparison With Proposed Beam Finite Elements," *Arch. Comput. Methods Eng.*, **21**(3), pp. 293–319.
- [8] Gerstmayr, J., Sugiyama, H., and Mikkola, A., 2013, "Review on the Absolute Nodal Coordinate Formulation for Large Deformation Analysis of Multibody Systems," *ASME J. Comput. Nonlinear Dyn.*, **8**(3), p. 031016.
- [9] Gerstmayr, J., and Shabana, A. A., 2005, "Efficient Integration of the Elastic Forces and Thin Three-Dimensional Beam Elements in the Absolute Nodal Coordinate Formulation," *Multibody Dynamics 2005, ECCOMAS Thematic Conference*.
- [10] Matikainen, M., Dmitrochenko, O., and Mikkola, A., 2010, "Beam Elements With Trapezoidal Cross Section Deformation Modes Based on the Absolute Nodal Coordinate Formulation," *International Conference of Numerical Analysis and Applied Mathematics*, pp. 19–25.
- [11] Mikkola, A., Dmitrochenko, O., and Matikainen, M., 2009, "Inclusion of Transverse Shear Deformation in a Beam Element Based on the Absolute Nodal Coordinate Formulation," *ASME J. Comput. Nonlinear Dyn.*, **4**(1), pp. 1–9.
- [12] Gruber, P. G., Nachbagauer, K., Vetyukov, Y., and Gerstmayr, J., 2013, "A Novel Director-Based Bernoulli-Euler Beam Finite Element in Absolute Nodal Coordinate Formulation Free of Geometric Singularities," *Mech. Sci.*, **4**(2), pp. 279–289.
- [13] Mikkola, A. M., and Matikainen, M. K., 2005, "Development of Elastic Forces for a Large Deformation Plate Element Based on the Absolute Nodal Coordinate Formulation," *ASME J. Comput. Nonlinear Dyn.*, **1**(2), pp. 103–108.
- [14] Nachbagauer, K., Pechstein, A. S., Irschik, H., and Gerstmayr, J., 2011, "A New Locking-Free Formulation for Planar, Shear Deformable, Linear and Quadratic Beam Finite Elements Based on the Absolute Nodal Coordinate Formulation," *Multibody Syst. Dyn.*, **26**(3), pp. 245–263.
- [15] Simo, J. C., and Vu-Quoc, L., 1986, "On the Dynamics of Flexible Beams Under Large Overall Motions—Part I: The Plane Case," *ASME J. Appl. Mech.*, **53**(4), pp. 849–863.
- [16] Simo, J. C., and Vu-Quoc, L., 1986, "On the Dynamics of Flexible Beams Under Large Overall Motions—Part II: The Plane Case," *ASME J. Appl. Mech.*, **53**(4), pp. 849–863.
- [17] Reissner, E., 1972, "On One-Dimensional Finite-Strain Beam Theory: The Plane Problem," *Z. Angew. Math. Phys.*, **23**(5), pp. 795–804.
- [18] Gerstmayr, J., Matikainen, M. K., and Mikkola, A. M., 2008, "A Geometrically Exact Beam Element Based on the Absolute Nodal Coordinate Formulation," *Multibody Syst. Dyn.*, **20**(4), pp. 359–384.

## Publication II

Ebel, H., Matikainen, M.K., Hurskainen, V.-V., Mikkola, A.  
**Higher-order beam elements based on the absolute nodal  
coordinate formulation for three-dimensional elasticity**

Reprinted with permission from  
*Nonlinear Dynamics*  
Vol. 88(2), pp. 1075–1091, April 2017  
© 2016, Springer Nature



# Higher-order beam elements based on the absolute nodal coordinate formulation for three-dimensional elasticity

Henrik Ebel · Marko K. Matikainen ·  
Vesa-Ville Hurskainen · Aki Mikkola

Received: 4 December 2015 / Accepted: 14 December 2016 / Published online: 28 December 2016  
© Springer Science+Business Media Dordrecht 2016

**Abstract** This study thoroughly examines various higher-order three and four-node beam elements for use in the absolute nodal coordinate formulation (ANCF). The paper carefully investigates which potential benefits and drawbacks the utilization of higher-order ANCF beam elements without in-slope vectors has in the case of the usage of full three-dimensional elasticity. When the elastic forces for shear-deformable ANCF beam elements are calculated using full three-dimensional elasticity—especially in the form of the St. Venant–Kirchhoff material law—Poisson locking severely deteriorates the accuracy of the numeric results. As shown in this paper, an existing approach to preventing this locking phenomenon for three-node beam elements can still produce unsatisfying results in load cases involving bidirectional bending. The

results of this study show that enriching the polynomial basis used to approximate the beam kinematics provides a natural solution to this issue. As will be seen, these findings for three-node elements can also be extended to four-node elements. When using a sufficient approximation order in transverse directions, satisfying accuracy can be achieved both in conventional one-dimensional bending and in the above-mentioned bidirectional load case.

**Keywords** Continuum beam elements · Three-dimensional elasticity · St. Venant–Kirchhoff material · Princeton beam experiment · Numerical locking

## 1 Introduction

The computer analysis of multibody system dynamics has become increasingly important in advanced machine system design. Increased computational power and enhanced formulations are making it possible to solve progressively more sophisticated mathematical models describing the dynamic behavior of complex systems. Nevertheless, computational efficiency is an important consideration for the multibody system dynamics analyst, and the level of detail for a mechanical system model should not be any greater than is needed to yield a sufficiently accurate numerical result. In multibody system dynamics, an acceptable simplification for the analysis of motion and forces in many

---

H. Ebel (✉)  
Institute of Engineering and Computational Mechanics,  
University of Stuttgart, Pfaffenwaldring 9, 70569 Stuttgart,  
Germany  
e-mail: henrik.ebel@itm.uni-stuttgart.de

M. K. Matikainen · V.-V. Hurskainen · A. Mikkola  
Mechanical Engineering, Lappeenranta University of  
Technology, Skinnarilankatu 34, 53850 Lappeenranta,  
Finland  
e-mail: marko.matikainen@lut.fi

V.-V. Hurskainen  
e-mail: vesa-ville.hurskainen@lut.fi

A. Mikkola  
e-mail: aki.mikkola@lut.fi

practical engineering problems can be obtained by representing a system under investigation by rigid interconnected bodies. In a number of practical applications, however, simulation accuracy can be improved significantly by taking into account deformations of one or more bodies. To this end, the floating frame of reference formulation can be used. In this approach, linear strain–displacement and linear stress–strain relations are typically assumed. Consequently, linear model order reduction techniques can be applied to the finite element models that represent the elastic bodies, which allows for efficient computation. However, these assumptions do not lead to accurate models in cases such as belts, cables, drapes, bushings and leaf springs. In these applications, more advanced approaches such as the absolute nodal coordinate formulation (ANCF) and the large rotation vector formulation need to be used [9, 11, 23]. These approaches can also handle nonlinear strain–displacement relationships as well as material nonlinearities.

The absolute nodal coordinate formulation is a finite element-based approach in which beam and plate elements are described using absolute nodal positions and their gradients [21]. Recently, solid (brick) elements have also been implemented in the ANCF framework [18]. By using the components of the deformation gradient instead of rotation angles, large reference rotations can be described without the singularity problems that may occur in the three-dimensional rotation description in a total Lagrangian formulation. The use of gradients instead of rotation angles as degrees of freedom in beam and plate elements can be seen as the fundamental feature of the absolute nodal coordinate formulation. This approach leads to a straightforward description for the equations of motion with a constant mass matrix which increases the numerical efficiency of the time integration. Therefore, it can be seen that the absolute nodal coordinate formulation is particularly suitable for multibody applications since models based on ANCF can be solved using time integration schemes typically used in multibody system dynamics. This makes it possible to combine the ANCF with simpler approaches to achieve desired simulation accuracies with minimal computational burden.

The development of ANCF-based elements can be divided into the following two variants. The first one comprises a family of ANCF-described conventional beam and plate elements that cannot capture transverse shear deformations. These elements are parame-

terized as centerlines or surfaces using gradient vectors to define the longitudinal direction and position coordinates to define the remaining directions. Elements based on this type of parametrization are often referred to as gradient deficient elements, because they lack gradient vectors in the transverse direction. The second variant applies the ANCF to describe shear-deformable elements. In the ANCF, transverse shear deformation is described by introducing additional gradient vectors in the transverse directions. These added gradient vectors also define cross-sectional or fiber deformation which allows the relaxation of some of the assumptions used in the Euler–Bernoulli and Timoshenko beam theories or Kirchhoff–Love and Mindlin–Reissner plate theories. On the downside, introducing the transverse gradient vectors can result in computational difficulties, such as locking, and can reduce accuracy and numerical performance. These problems are particularly severe when defining elastic forces by employing the St. Venant–Kirchhoff material model. To alleviate these problems, elastic forces can be defined using a structural mechanics-based approach, in which strain components are handled independently. Despite the fact that the structural approach in the definition of elastic forces leads to accurate results, it is cumbersome to use in the case of advanced material models [6, 19].

An interesting extension for shear-deformable ANCF-based elements can be obtained by using higher-order derivatives to mitigate numerical locking phenomena and thereby improving accuracy. Gerstmayr and Shabana [8] first introduced ANCF beam elements where the polynomial basis was enriched with higher-order polynomials by using the components of higher-order derivatives as additional nodal coordinates. In [8], polynomial enrichment with respect to the longitudinal coordinate was used to prevent slow convergence as a result of shear locking. Matikainen et al. [13, 14] proposed the use of higher-order components to describe cross-sectional deformations more precisely. By including the trapezoidal cross-sectional mode, this higher-order approach helps to overcome the Poisson locking phenomenon when using the St. Venant–Kirchhoff material law. For this purpose, a three-dimensional four-node plate element in the framework of the higher-order ANCF elements introduced in [16] uses second-order displacement interpolation in thickness direction. In [22], three-dimensional two-node higher-order beam elements were studied. One of the proposed two-node elements uses second-order inter-

polation for cross-sectional deformation, which has the potential to lead to a locking-free beam element with St. Venant–Kirchhoff material. In [12], higher-order beam elements without longitudinal slope vectors were studied. One of the proposed three-node higher-order elements uses second-order interpolation for cross-sectional deformation modes leading to promising results in both large deformation problems with two-dimensional loading as well as in eigenvalue analysis. The Euler–Bernoulli type ANCF elements were studied in the framework of the higher-order beam elements [10, 24].

The objective of this paper is to demonstrate that accurate results in the absolute nodal coordinate formulation can be obtained by using three- and four-node higher-order elements based on full three-dimensional elasticity. The studied beam elements are based on continuum mechanics theory, and the St. Venant–Kirchhoff material model is used in the formulations. To this end, the paper introduces a higher-order approach for beam structures in which an enriched polynomial basis is used so that more elaborate cross-sectional deformation modes can be represented. The introduced approach is carefully verified using numerical examples including the so-called “Princeton beam experiment”.

### 2 Kinematics of the higher-order ANCF beam elements

Let  $\mathbf{r} = \mathbf{r}(\mathbf{x}, t) \in \mathbb{R}^3$  denote the global position at time  $t$  of an arbitrary particle. Therein, the vector  $\mathbf{x}$  defines the reference configuration of the examined

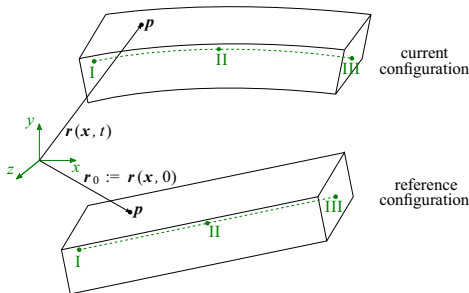


**Fig. 1** Illustration of a three-node beam element with an arbitrary particle  $\mathbf{p}$  in reference and in current configuration. The three nodes are denoted by I, II and III, respectively

elastic body. For a three-node beam element, this is illustrated in Fig. 1.

In the ANCF, this position vector  $\mathbf{r}$  can be expressed in the form

$$\mathbf{r}(\mathbf{x}, t) = \mathbf{S}_m(\mathbf{x})\mathbf{e}(t) \tag{1}$$

where  $\mathbf{S}_m$  is the shape function matrix containing appropriately chosen shape functions and  $\mathbf{e} = \mathbf{e}(t)$  is the vector of nodal coordinates. The vector  $\mathbf{e}$  contains the position of the nodes expressed in the inertial frame as well as derivatives of these positions. Therefore, in the following, the shorthand notations

$$\begin{aligned} \mathbf{r}_{,x} &:= \frac{\partial \mathbf{r}}{\partial x}, & \mathbf{r}_{,y} &:= \frac{\partial \mathbf{r}}{\partial y}, & \mathbf{r}_{,z} &:= \frac{\partial \mathbf{r}}{\partial z}, \\ \mathbf{r}_{,yz} &:= \frac{\partial^2 \mathbf{r}}{\partial y \partial z}, & \mathbf{r}_{,yy} &:= \frac{\partial^2 \mathbf{r}}{\partial y^2}, & \mathbf{r}_{,zz} &:= \frac{\partial^2 \mathbf{r}}{\partial z^2} \\ \mathbf{r}_{,yyz} &:= \frac{\partial^3 \mathbf{r}}{\partial y^2 \partial z}, & \mathbf{r}_{,yyy} &:= \frac{\partial^3 \mathbf{r}}{\partial y^3}, & \mathbf{r}_{,zzz} &:= \frac{\partial^3 \mathbf{r}}{\partial z^3} \\ \mathbf{r}_{,yzz} &:= \frac{\partial^3 \mathbf{r}}{\partial y \partial z^2} \end{aligned}$$

are used to denote the directional derivatives occurring in the elements considered in this paper. The specific vectors of nodal coordinates used for the various elements are depicted in Table 1 and will be discussed later.

The shape function matrix can be derived with the help of the polynomial basis used to approximate the absolute particle position  $\mathbf{r}$ . Without loss of generality, assume that a monomial basis is used for the desired polynomial vector space and that  $\mathbf{b}_p \in \mathbb{R}^{1 \times p}$  is a vector containing the monomials of the basis. Also, the same basis is used to approximate all three dimensions of  $\mathbf{r}$  such that

$$\mathbf{r}(\mathbf{x}, t) = \mathbf{P}(\mathbf{x})\mathbf{a}(t) \tag{2}$$

holds with  $\mathbf{a}$  being the vector of polynomial coefficients and  $\mathbf{P}$  defined as

$$\mathbf{P} = \text{diag}(\mathbf{b}_p, \mathbf{b}_p, \mathbf{b}_p) \in \mathbb{R}^{3 \times (3 \cdot p)}. \tag{3}$$

In order to obtain an expression in the form of Eq. (1), a transformation

$$\mathbf{e}(t) = \mathbf{T}_p \mathbf{a}(t) \tag{4}$$

**Table 1** Proposed elements with their nodal degrees of freedom and the monomial basis employed

Element	Nodal degrees of freedom	Basis
3343	$\mathbf{r}, \mathbf{r}_{,y}, \mathbf{r}_{,z}, \mathbf{r}_{,yz}$	$\beta \cup \{yz, xyz, x^2yz\}$
3343 <sub>111</sub>	$\mathbf{r}, \mathbf{r}_{,y}, \mathbf{r}_{,z}, \mathbf{r}_{,xyz}$	$\beta \cup \{xyz, x^2yz, x^3yz\}$
3353	$\mathbf{r}, \mathbf{r}_{,y}, \mathbf{r}_{,z}, \mathbf{r}_{,yy}, \mathbf{r}_{,zz}$	$\beta^{[3353]} := \beta \cup \{y^2, xy^2, x^2y^2, z^2, xz^2, x^2z^2\}$
3363	$\mathbf{r}, \mathbf{r}_{,y}, \mathbf{r}_{,z}, \mathbf{r}_{,yz}, \mathbf{r}_{,yy}, \mathbf{r}_{,zz}$	$\beta^{[3363]} := \beta^{[3353]} \cup \{yz, xyz, x^2yz\}$
34X3	$\mathbf{r}, \mathbf{r}_{,y}, \mathbf{r}_{,z}, \mathbf{r}_{,yz}, \mathbf{r}_{,yy}, \mathbf{r}_{,zz}, \mathbf{r}_{,yyz}, \mathbf{r}_{,yzz}, \mathbf{r}_{,yyy}, \mathbf{r}_{,zzz}$	See Eq. (12)

Therein, the shorthand notation  $\beta := \beta^{[3333]} = \{1, x, y, z, xy, xz, x^2, x^2y, x^2z\}$  is used

with an invertible matrix  $T_p$  yielding the desired expression

$$\mathbf{r}(x, t) = \mathbf{P}(x)\mathbf{a}(t) = \mathbf{P}(x)\mathbf{T}_p^{-1}\mathbf{e}(t) =: \mathbf{S}_m(x)\mathbf{e}(t) \quad (5)$$

is needed. In this transformation, the matrix  $T_p$  is a direct consequence of the conditions resulting from inserting the reference positions of the nodes into Eq. (2) as well as into the derivatives of Eq. (2) that are used as nodal coordinates. Consequently, when constructing higher-order elements, the choice of basis functions in  $\mathbf{b}_p$  is closely related to the choice of nodal coordinates  $\mathbf{e}$  in the sense that the matrix  $T_p$  must have full rank.

2.1 Shape functions for the considered beam elements

This paper considers four different three-node beam elements and, for demonstrative purposes, one four-node beam element. There are two fundamentally different approaches to derive the vector of elastic forces—namely the structural mechanics-based and the full elasticity-based approaches. As will be discussed later, for higher-order elements, the approach based on full three-dimensional elasticity, which is rooted in fundamental continuum mechanics, is to be preferred. To differentiate the elements studied, the four-digit numerical code as introduced in [2] will be used. For four digits  $abcd$ ,  $a$  denotes the dimension of the element,  $b$  the number of nodes, and  $c$  the number of degrees of freedom per node and dimension. In this study, the digit  $d$  will always take the value 3 as the same polynomial basis is used to approximate all 3 dimensions. For the purpose of this paper, the number of degrees of freedom per node and dimension  $c$  will be called ‘the order of the element’.

In this paper, the various higher-order elements differ in the choice of additional nodal degrees of freedom. In general, the vector of nodal coordinates for a beam element with  $b$  nodes can be written as

$$\mathbf{e} = [\mathbf{e}_I^T \mathbf{e}_{II}^T \dots \mathbf{e}_b^T]^T. \quad (6)$$

Therein,  $\mathbf{e}_i, i \in \{I, II, \dots, b\}$ , is the vector of nodal coordinates of the  $i$ -th node.

The three-node elements considered here can be seen as extensions of the lower-order three-node beam element proposed by Nachbagauer et al. in [17]. This element possesses

$$\mathbf{e}_i^{[3333]} = [\mathbf{r}^{(i)T} \mathbf{r}_{,y}^{(i)T} \mathbf{r}_{,z}^{(i)T}]^T \quad (7)$$

as its nodal degrees of freedom.

The first element examined is element 3343 with the degrees of freedom of one node chosen to

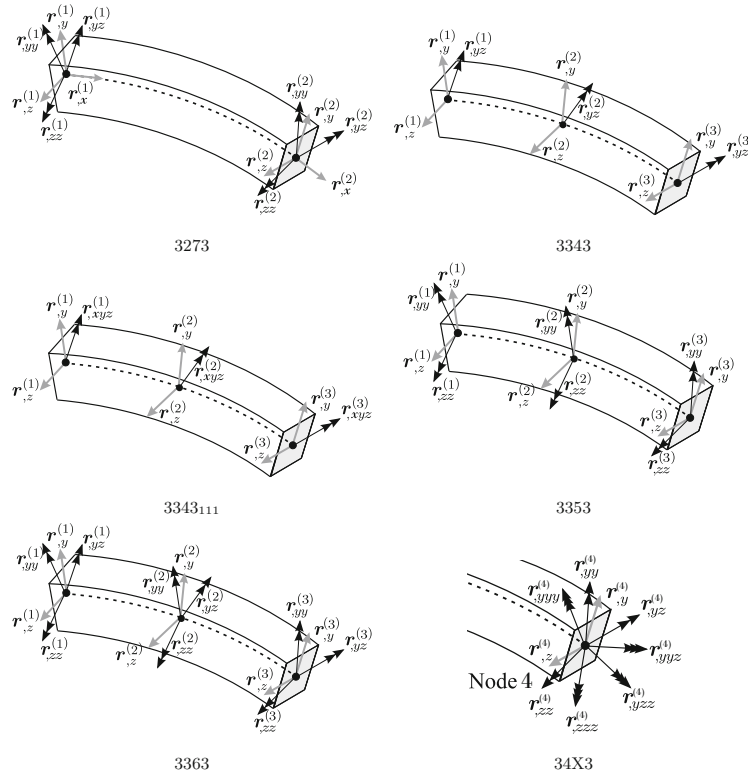
$$\mathbf{e}_i^{[3343]} = [\mathbf{r}^{(i)T} \mathbf{r}_{,y}^{(i)T} \mathbf{r}_{,z}^{(i)T} \mathbf{r}_{,yz}^{(i)T}]^T \quad (8)$$

with the superscript ( $i$ ) denoting that the positions and derivatives are evaluated at the location of node  $i$ . The use of the vector  $\mathbf{r}_{,yz}$  allows to describe trapezoidal deformations of the cross section. This is important in order to diminish the influence of Poisson locking [15]. Another valid choice of nodal degrees of freedom for an element of the same order is

$$\mathbf{e}_i^{[3343_{111}]} = [\mathbf{r}^{(i)T} \mathbf{r}_{,y}^{(i)T} \mathbf{r}_{,z}^{(i)T} \mathbf{r}_{,xyz}^{(i)T}]^T \quad (9)$$

and the respective element will be denoted by 3343<sub>111</sub>. In the same way, elements of orders 5 and 6 can be introduced which further increase the number of

**Fig. 2** Illustration of the elements occurring in this study including their nodal degrees of freedom



basis polynomials theoretically enabling the reproduction of more complex deformation modes of the cross section. This leads to the nodal degrees of freedom

$$e_i^{[3353]} = [r^{(i)T} \ r_{,y}^{(i)T} \ r_{,z}^{(i)T} \ r_{,yy}^{(i)T} \ r_{,zz}^{(i)T}]^T, \quad (10)$$

$$e_i^{[3363]} = [r^{(i)T} \ r_{,y}^{(i)T} \ r_{,z}^{(i)T} \ r_{,yz}^{(i)T} \ r_{,yy}^{(i)T} \ r_{,zz}^{(i)T}]^T \quad (11)$$

for the elements 3353 and 3363, respectively. As described at the beginning, this choice is also motivated by the circumstance that a polynomial basis must exist and be found so that  $T_p$  as in Eq. (5) is invertible. In the same manner, a four-node beam element of order 10, subsequently denoted by 34X3, can be derived. Taking all this into account, the basis monomials for the various elements can be written as given in Table 1.

To get a better understanding of the nodal coordinates of the various elements, Fig. 2 illustrates these coordinates.

The basis for the four-node element can be written as

$$\begin{aligned} \beta^{[3363]} \cup & \{x^3, x^3y, x^3z, x^3yz, x^3y^2, x^3z^2\} \\ & \cup \{y^2z, xy^2z, x^2y^2z, x^3y^2z\} \\ & \cup \{yz^2, xyz^2, x^2yz^2, x^3yz^2\} \\ & \cup \{y^3, xy^3, x^2y^3, x^3y^3\} \cup \{z^3, xz^3, x^2z^3, x^3z^3\}. \end{aligned} \quad (12)$$

Since the elements are isoparametric, the resulting shape functions can equivalently be given both in the physical coordinate system  $\{x, y, z\}$  and in local element coordinates  $\{\xi, \eta, \zeta\}$ . In the present paper, without loss of generality, it is assumed that the beam of length  $L$ , height  $H$  and width  $W$  is initially rectangular with the directions of the respective axes of the physical and local element coordinate systems coinciding. Also, the local coordinates are assumed to be scaled such that  $-1 \leq \xi, \eta, \zeta \leq 1$ . Hence, in these coordinates, the

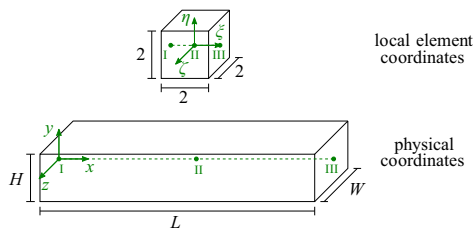


**Fig. 3** Illustration of a three-node beam element in physical and in local element coordinates with coordinate systems as presumed in Sect. 2.1. The three nodes are denoted by I, II and III, respectively

element represents a bi-unit cube. For a three-node beam, these assumptions are illustrated in Fig. 3. With these basis functions, the shape function matrix  $S_m$  can be derived by means of a simple calculation as shown in Eqs. (2)–(5). In the case of element 3343, for instance, this yields 12 different shape functions of the form

$$\begin{aligned}
 s_1 &= 1/2 \xi^2 - 1/2 \xi, \\
 s_2 &= 1/4 \eta H \xi^2 - 1/4 \eta H \xi \\
 s_3 &= 1/4 \zeta W \xi^2 - 1/4 \zeta W \xi, \\
 s_4 &= 1/8 \eta H \zeta W \xi^2 - 1/8 \eta H \zeta W \xi, \\
 s_5 &= -\xi^2 + 1, \\
 s_6 &= -1/2 \eta H \xi^2 + 1/2 \eta H, \\
 s_7 &= -1/2 \zeta W \xi^2 + 1/2 \zeta W, \\
 s_8 &= -1/4 \eta H \zeta W \xi^2 + 1/4 \eta H \zeta W, \\
 s_9 &= 1/2 \xi^2 + 1/2 \xi, \\
 s_{10} &= 1/4 \eta H \xi^2 + 1/4 \eta H \xi, \\
 s_{11} &= 1/4 \zeta W \xi^2 + 1/4 \zeta W \xi, \\
 s_{12} &= 1/8 \eta H \zeta W \xi^2 + 1/8 \eta H \zeta W \xi,
 \end{aligned}$$

this time given in local element coordinates. The shape function matrix  $S_m$  then is of the structure

$$\begin{aligned}
 S_m &= s_v^{[3343]} \otimes \begin{bmatrix} 1 & 0 & 0 \\ 0 & 1 & 0 \\ 0 & 0 & 1 \end{bmatrix} \\
 &= \begin{bmatrix} s_1 & 0 & 0 & s_2 & 0 & 0 & \cdots & s_{12} & 0 & 0 \\ 0 & s_1 & 0 & 0 & s_2 & 0 & \cdots & 0 & s_{12} & 0 \\ 0 & 0 & s_1 & 0 & 0 & s_2 & \cdots & 0 & 0 & s_{12} \end{bmatrix},
 \end{aligned}$$

with  $s_v^{[3343]} = [s_1 \ s_2 \ \cdots \ s_{12}]$  and  $\otimes$  denoting the Kronecker product.

**3 Elastic forces**

The elastic forces can be derived using two different approaches—the first one being based on three-dimensional elasticity and the second one on structural mechanics [17]. General hyperelastic materials can be used for the derivation of the elastic forces in continuum elements. In this work, three-dimensional elasticity is employed in the form of the St. Venant–Kirchhoff material model that assumes a linear relationship

$$S = {}^4D : E \tag{13}$$

between the Green–Lagrange strain tensor  $E$  and the second Piola–Kirchhoff stress tensor  $S$ . The fourth-order tensor  ${}^4D$  includes the properties of the material. For an elastic isotropic material, the relationship takes the form

$$S = \lambda I \text{tr}(E) + 2G E, \tag{14}$$

where  $\lambda$  and  $G$  are the Lamé elastic constants. Therein, using the deformation gradient  $F$ , the Green–Lagrange strain tensor is defined as

$$E = \frac{1}{2} (F^T F - I). \tag{15}$$

For the purpose of defining the deformation gradient, let  $r$  denote the current position of an arbitrary particle, while  $r_0$  denotes the reference configuration. Then,  $F$  reads

$$F = \frac{\partial r}{\partial r_0} = \frac{\partial r}{\partial \xi} \frac{\partial \xi}{\partial r_0} =: \frac{\partial r}{\partial \xi} J^{-1} \tag{16}$$

wherein  $\xi = [\xi \ \eta \ \zeta]^T$  and  $J$  is the Jacobian matrix that provides the transformation between the physical and local coordinate systems. Using Voigt notation, the strains and stresses can be expressed in form of the two vectors

$$\begin{aligned}
 \epsilon &= [E_{11} \ E_{22} \ E_{33} \ 2E_{23} \ 2E_{13} \ 2E_{12}]^T, \\
 \sigma &= [S_{11} \ S_{22} \ S_{33} \ S_{23} \ S_{13} \ S_{12}]^T.
 \end{aligned}$$

This allows to rewrite equation (13) in the form  $\sigma = \hat{D}\epsilon$  with

$$\hat{D} = \begin{bmatrix} \lambda + 2G & \lambda & \lambda & 0 & 0 & 0 \\ \lambda & \lambda + 2G & \lambda & 0 & 0 & 0 \\ \lambda & \lambda & \lambda + 2G & 0 & 0 & 0 \\ 0 & 0 & 0 & G & 0 & 0 \\ 0 & 0 & 0 & 0 & Gk_{s2} & 0 \\ 0 & 0 & 0 & 0 & 0 & Gk_{s3} \end{bmatrix}, \quad (17)$$

shear corrections factors  $k_{s2}, k_{s3}$ , Lamé parameter  $\lambda$  and shear modulus  $G$ . Using these relationships, the virtual work done by elastic forces can be written as

$$\delta W_i^c = \left( \frac{1}{2} \nabla_e \int_{-1}^1 \int_{-1}^1 \int_{-1}^1 \epsilon^T \hat{D} \epsilon \det(\mathbf{J}) \, d\xi \, d\eta \, d\zeta \right) \cdot \delta e \quad (18)$$

and the desired vector of elastic forces is given by the term in brackets. For implementation purposes, the integration in Eq. (18) is performed by Gaussian integration of a sufficient degree of exactness. In the above case of rectangular cross sections and appropriately scaled coordinate systems, standard Gaussian quadrature rules can be applied directly and independently for the three integrations.

For lower-order elements in the case of bending, it has been observed that, for Poisson ratios other than zero, this approach leads to a locking phenomenon called Poisson locking. As shown by Nachbagauer et al. [17], this can be overcome by splitting the equation describing the elastic forces into two parts, only considering the Poisson effect on the central axis of the beam and applying different quadrature rules for the two parts. While this approach solves the described problems with Poisson locking, it still produces poor results in certain load cases with bidirectional bending. This will be demonstrated in numerical examples examined below. It is for this reason that, for the higher-order elements examined in this paper, no such approach is taken in order to gain insight whether a richer polynomial basis is able to eliminate or at least alleviate the effect of Poisson locking in a natural way. In fact, if one understands Poisson locking as the result of the inability of the element to reproduce the cross-sectional deformation caused by the coupling of axial and transverse normal strains, it makes sense to enrich the polynomial basis so that more elaborate cross-sectional deformation modes can be represented.

Next, the definition of the elastic forces for beam elements based on structural mechanics is briefly discussed. In this case, the virtual work  $\delta W_i^s$  done by elastic forces can be understood to consist of two parts. The first one, denoted by  $\delta W_i^{bt}$  below, is associated with beam bending and torsion, and the second one,  $\delta W_i^{cd}$ , is associated with the deformation of the cross section [17]. The first part can be expressed as

$$\delta W_i^{bt} = \left( \frac{1}{2} \nabla_e \int_{-1}^1 (EA \Gamma_1^2 + GA \Gamma_2^2 k_{s2} + GA \Gamma_3^2 k_{s3} + GJ \kappa_1^2 + EI_2 \kappa_2^2 + EI_3 \kappa_3^2) \Big|_{(\eta,\zeta)=0} \det(\mathbf{J}) \, d\xi \right) \cdot \delta e \quad (19)$$

with sectional parameters for axial and shear strains  $\Gamma_1, \Gamma_2$  and  $\Gamma_3$ , as well as torsional and bending strains  $\kappa_1, \kappa_2$  and  $\kappa_3$ , see [17] and [1]. It is noteworthy that in Eq. (19), bending and torsion are only taken into account using the central axis of the beam, which is somewhat characteristic for the approach taken in structural mechanics. This explains why the structural approach is conceptually incompatible with higher-order elements since additionally considered higher-order terms are always zero on the central axis. On the other hand, the expression for the virtual work related to cross-sectional deformation can be written as

$$\delta W_i^{cd} = \left( \frac{1}{2} \nabla_e \int_{-1}^1 (EA (E_{22}^2 + E_{33}^2) + 2 GA E_{23}^2) \det(\mathbf{J}) \, d\xi \right) \cdot \delta e. \quad (20)$$

For higher-order elements, the integrand in Eq. (20) would also depend on  $\eta$  and  $\zeta$ . However, simply replacing the one-dimensional by a three-dimensional integration does not work since this leads to an inconsistency with Eq. (19) where higher-order deformation modes would be considered for cross-sectional deformation but not for bending and torsion. Consequently, only the approach based on three-dimensional elasticity is used for the higher-order elements. However, numerical results using the lower-order three-node beam element in structural formulation as proposed in [17] will be included as a reference. Using the above contributions, the total virtual work of internal forces in structural formulation reads

$$\delta W_i^s = \delta W_i^{bt} + \delta W_i^{cd}. \quad (21)$$

#### 4 Numerical analysis using benchmark problems

This paper examines five different higher-order beam elements. As outlined above, the elastic forces are calculated using the St. Venant–Kirchhoff material law. These elements are applied in a series of different benchmark problems to gain insight into the accuracy attainable using the respective approximation orders and formulations. For comparison purposes, numerical results using the lower-order beam element proposed by Nachbagauer et al. [17], subsequently denoted as element 3333, both in structural and in three-dimensional elasticity-based formulations are given. For the sake of readability, the four-digit numerical code of the elements will be supplemented by an ‘s’ for structural or a ‘c’ for full elasticity-based elements.

In order to prevent Poisson locking, element 3333c makes use of the splitting and selective integration of Eq. (18) as introduced in [17]. In the case of the eigenfrequency analysis, results of the two-node higher-order element proposed in [20] are used for highlighting the advantages of three-node beam elements. This two-node element of order 7 is denoted by 3273c in the following. Also, in more elaborate numerical examples that rely on nonlinear phenomena, results obtained using beam and solid elements of the commercial software ANSYS permit comparisons with conventional finite element formulations. The numerical calculations involving the ANCF elements have been performed in MATLAB. During assembly of the ANCF elements, all the coordinates of inter-element nodes are shared and hence the continuity of all nodal degrees of freedom is enforced across the element borders.

##### 4.1 Small displacement cantilever

To verify that there is no fundamental flaw in the formulation or implementation of the elements, a simple test is conducted involving a cantilever with a concentrated load on the tip of the beam. The force is chosen such that the resulting displacement is small enough enabling a meaningful comparison with the analytical solution for the tip displacement using linear Timoshenko theory. In this experiment, a beam of the length  $L = 2$  m with a rectangular cross section of the height  $H = 0.5$  m and the width  $W = 0.1$  m, Young’s modulus  $E = 2.07 \times 10^{11}$  N/m<sup>2</sup> and Poisson’s ratio  $\nu = 0.3$  is examined. The force on the tip of

**Table 2** Tip displacements obtained in the small displacement cantilever test for all considered elements along with the linear reference solution using Timoshenko beam theory

element [#]	$u_x$ [m]	$u_y$ [m]
3343c [64]	$-1.5834 \times 10^{-7}$	$7.2976 \times 10^{-4}$
3343 <sub>111</sub> c [64]	$-1.2757 \times 10^{-7}$	$6.5572 \times 10^{-4}$
3353c [64]	$-1.5745 \times 10^{-7}$	$7.2843 \times 10^{-4}$
3363c [64]	$-1.8951_s \times 10^{-7}$	$7.9834 \times 10^{-4}$
34X3c [64]	$-1.9142 \times 10^{-7}$	$8.0363 \times 10^{-4}$
3273c [64]	$-1.8913 \times 10^{-7}$	$7.9744 \times 10^{-4}$
3333s [64]	$-1.8885 \times 10^{-7}$	$8.0990 \times 10^{-4}$
3333c [64]	$-1.9472 \times 10^{-7}$	$8.0990 \times 10^{-4}$
Reference		$8.0990 \times 10^{-4}$

The numbers of elements used are given in square brackets

the beam is of the value  $F_y = 62.5 \times 10^3$  N. For the ANCF elements that employ approximations of higher order in the transversal directions, due to the different assumptions for the cross-sectional deformation, transverse and torsional shear correction factors are set to 1. The typical shear correction factors used for linear theories are only correct if straight surfaces remain straight, i.e., if there is no higher-order deformation of the cross section [25]. On the other hand, for the transversally linear 3333-elements, the shear correction factors are set to  $k_s := k_{s_2} = k_{s_3} = 10(1 + \nu)/(12 + 11\nu)$ . The chosen parameters are the same as those used in [17] which permits direct comparisons of the results. The analytical solution is given as

$$u_y = \frac{F_y L^3}{3EI_z} + \frac{F_y L}{GAk_s} \approx 8.0990 \times 10^{-4} \text{ m.} \quad (22)$$

The results of the numerical calculations using the studied ANCF elements are depicted in Table 2. As can be seen from the results, apart from the reference elements, only elements 3363c and 34X3c are in acceptable agreement with the linear reference solution. Generally, it is to be expected that these two elements, as well as element 3273c, do not deliver exactly the same result as the 3333 elements. One of the reasons behind this is that, for the 3333s element, the Poisson effect is neglected in the derivation of the strain energy contribution of cross-sectional deformation and for the 3333c element, it is only considered on the central axis of the beam. For the higher-order three-dimensional elasticity-based elements, however, the Poisson effect

**Table 3** Eigenfrequencies of the simply supported beam for selected modes in rad/s

	3333s	3333c	3363c	34X3c	3273c	BEAM188
1st Bending	95.634	95.634	95.417	94.969	95.431	95.605
2nd Bending	332.23	332.23	329.63	325.39	329.78	331.93
3rd Bending	635.70	635.70	625.10	613.25	625.59	634.85
1st Axial	280.32	280.18	247.42	244.00	247.56	280.32
1st Torsional	315.14	320.50	347.69	347.69	347.70	321.66
2nd Torsional	603.10	641.00	695.39	695.39	695.46	643.34

The results were obtained using 128 of each of the ANCF and ANSYS beam elements

is fully incorporated in the derivation of the elastic forces. Additionally, the elements 3363c, 34X3c and 3273c are nonlinear in the transversal directions permitting second-order deformations of the cross sections. Effects like these are neglected in the classical beam theory in which straight surfaces remain straight. Naturally, for this small deformation problem, this does not significantly affect the result, and thus the results of the higher-order elements are still comparatively close to the analytical solution. However, these theoretical differences will have a more significant effect in load cases involving larger deformations. On another note, the elements 3343c, 3343<sub>111</sub>c and 3353c—just like comparable elements of lower order—suffer from severe Poisson locking. For this reason, and in order to increase the readability of tables and figures, the following numerical experiments are mainly conducted for the reference elements and the element 3363c. Nevertheless, comparing the results obtained with the elements 3343c and 3343<sub>111</sub>c shows that allowing for trapezoidal deformations of the cross section, while not sufficient to fully eliminate Poisson locking, indeed seems to be more important than other second-order deformation modes since element 3343c yields the better results of the two.

As a summary, it can be concluded that for three-node beam elements as considered here, the approximation order of the beam kinematics must be at least of order 2 in all directions to eliminate Poisson locking without applying any simplifications. Based on this, it appears that using the same polynomial order equal to or larger than 2 for the approximation of displacements in all three directions seems to be a good practice. Element 34X3c substantiates this thesis since it uses approximations of third order in all directions and delivers good results. However, it remains to be seen if this hypothesis still holds true for more

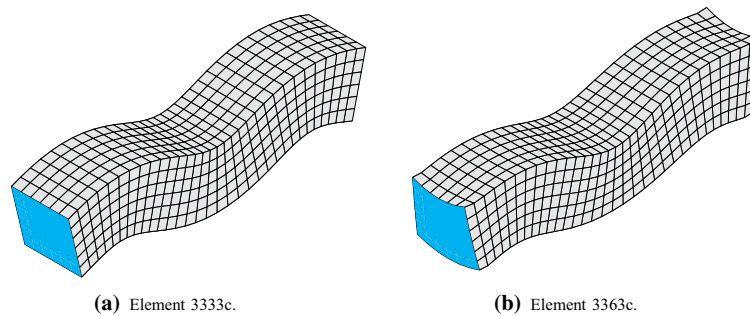
elaborate numerical tests that are conducted in the following.

#### 4.2 Eigenfrequencies of the simply supported beam

The second numerical test is an eigenfrequency analysis with simply supported boundaries, previously studied for instance in [7]. The eigenfrequency analysis is used as a linearized dynamics test because it offers the advantage of coordinate-free frequency and vibration mode comparisons. The numerical values of the parameters are adopted from [7]. The beam is of the length  $L = 2$  m and has a cross section of the width and height  $W = H = 0.4$  m. Young's modulus is chosen to be  $E = 1 \times 10^9$  N/m<sup>2</sup>, the density is  $\rho = 7850$  kg/m<sup>3</sup>, the shear modulus is given by  $G = E/2(1 + \nu)$  and Poisson's ratio is  $\nu = 0.3$ . Once again, all shear correction factors are set to 1. The reference solutions for the bending modes were calculated using the ANSYS beam element BEAM188. It is a linear two-node three-dimensional beam element that takes shear deformation into account. With the ANSYS default option keys used in these calculations, it has six nodal degrees of freedom and linear shape functions along its length. A four-cell cross section was used in the model. The numerical results are depicted in Table 3.

As can be seen from the results, the higher-order three-dimensional elasticity-based elements are converging to different eigenfrequencies especially in axial and higher-order bending modes compared to the structural and ANSYS beam elements. Nonetheless, when compared among themselves, the eigenfrequencies of the higher-order elements seem to converge to the same or, when considering also element 34X3c, at least more similar values. This can be explained by two circumstances. Firstly, as explained before, there are consti-

**Fig. 4** Visualization of the third bending mode using 32 of the respective elements



tutive differences in the derivation of the elastic forces when comparing elements 3363c, 34X3c and 3273c with the 3333 elements. Secondly, for the higher-order elements, the axial and higher-order bending modes show rather significant warping of the cross section that cannot be reproduced by beam elements that are linear in transverse direction. For the third bending mode, this is visualized in Fig. 4.

The investigation of higher-order plate elements in [16] revealed a locking phenomenon that deteriorates the accuracy attainable in the calculation of the eigenfrequencies of bending modes. In [16], this type of problem seems to possibly originate from the use of the longitudinal slope vector  $r_{,x}$  as a nodal degree of freedom. Fortunately, for the higher-order three-node elements considered here, only nodal positions and derivatives in transversal directions are used as degrees of freedom. For element 3273c originally proposed in [20], however,  $r_{,x}$  is indeed used as a nodal degree of freedom. As observed above, to eliminate Poisson locking, an interpolation order of at least 2 is needed in transversal directions. To construct a basis so that  $T_p$  of Sect. 2 is invertible, the interpolation in axial direction must be of order 3. In consequence, since there are only two nodes in the case of element 3273c, the longitudinal slope vector must be part of the set of nodal coordinates, despite the possibly negative effects.

Moreover, in [20], it has also been noted that element 3273c suffers from shear locking. When compared to element 3363c, element 3273c lacks, among others, the monomials  $x^2y$  and  $x^2z$  in its basis. In [8] however, exactly these monomials help to reduce shear locking in a beam element with 30 degrees of freedom, albeit not completely eliminating it. Hence, because of these basis polynomials and the observations with

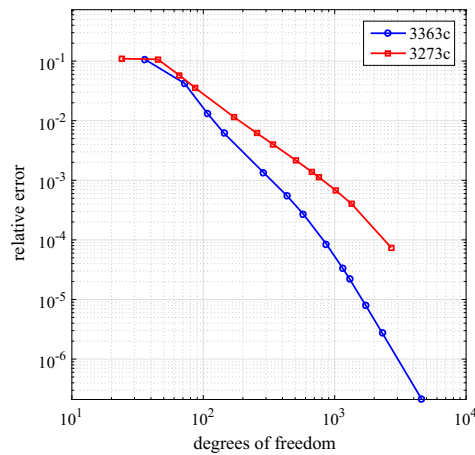


**Fig. 5** Relative errors obtained in the numerical calculation of the eigenfrequency of the first bending mode when using elements 3363c and 3273c. For the calculation of the relative error, the numerical results obtained when using 196 of the respective elements were used as the reference result

plate elements [16] mentioned above, one might expect a better convergence rate for element 3363c. As can be gathered from Fig. 5, element 3363c indeed performs markedly better with respect to the convergence of the eigenfrequency of the first bending mode.

For low numbers of degrees of freedom, the results obtained with element 3273c show no convergence whatsoever. For higher numbers of degrees of freedom, element 3273c exhibits an approximately quadratic convergence rate, while element 3363c converges approximately cubically. This locking effect of element 3273c becomes more pronounced for higher-

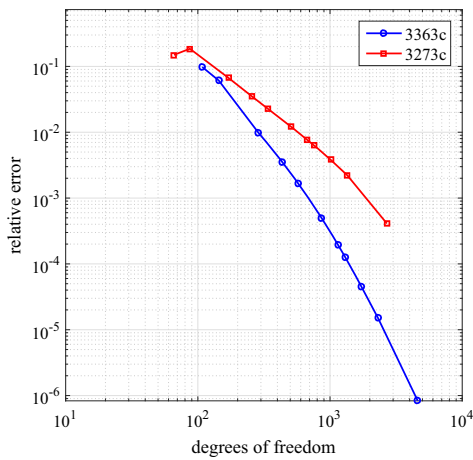


**Fig. 6** Relative errors obtained in the numerical calculation of the eigenfrequency of the third bending mode when using elements 3363c and 3273c. For the calculation of the relative error, the numerical results obtained when using 196 of the respective elements were used as the reference result

order modes. As can be seen in Fig. 6 for the third bending mode, when increasing the amount of elements used, the obtained relative error even increases initially. Since this locking phenomenon persists if Poisson's ratio is set to zero, it is unrelated to Poisson locking.

In effect, as explained above, this locking phenomenon might result from certain missing polynomials in the basis of element 3273c or possibly also from the inclusion of the longitudinal slope vector which poses additional continuity requirements of the solution across the element boundaries. Since these two circumstances cannot be separated completely for the considered elements, further studies are needed to fully

understand the reasons for this locking behavior. In the meantime, the results of this study show that the setup of element 3363c leads to a complete removal of the locking phenomenon.

#### 4.3 Eigenfrequencies of the unconstrained beam

Since the boundary conditions of an ideal simply supported beam cannot easily be replicated with solid finite elements, an additional eigenfrequency analysis for an unconstrained beam has been undertaken. Thus, a comparison with results of solid elements is made possible. The parameters used match the ones from the previous simply supported beam of Sect. 4.2. The obtained numerical results are given in Table 4.

As can be seen, the ANCF elements using full three-dimensional elasticity deliver quite similar results when compared with each other. However, for the second and third bending modes, element 34X3c is significantly closer to the result obtained with the ANSYS solid element SOLID95 which might be explained by the more accurate representation of the cross-sectional warping made possible by the third-order approximation in transversal directions for element 34X3c. SOLID95 is a 20-node structural solid element with three nodal degrees of freedom. Although the element has multiple possible shapes, in these calculations a hexahedral mesh was applied.

Nevertheless, as will be seen in the following sections, the differences in the results of actual nonlinear tests are not nearly as large as one might expect when looking at the eigenfrequency results. This calls attention to the fact that for nonlinear systems, results of tests relying on linearization are inherently of limited informative value. On another note, the eigenfrequencies obtained for the torsional modes differ from the refer-

**Table 4** Eigenfrequencies of the unconstrained beam for selected modes in rad/s

	3333s	3333c	3363c	34X3c	3273c	BEAM188	SOLID95
1st Bending	204.17	204.17	205.63	204.44	205.64	204.10	204.40
2nd Bending	477.91	477.91	487.40	479.74	487.46	477.52	479.38
3rd Bending	795.84	795.84	819.95	800.82	820.12	794.89	799.30
1st Axial	560.64	559.45	558.96	558.94	558.96	560.65	558.94
1st Torsional	315.14	320.50	347.69	347.69	347.70	321.66	319.29
2nd Torsional	603.10	640.99	695.39	695.39	695.46	643.34	638.37

The results were obtained using 128 of each of the ANCF and ANSYS beam elements. For the solid element, a mesh with  $80 \times 16 \times 16$  elements was used

**Table 5** Tip displacements obtained in the large displacement cantilever test. The numbers of elements used are given in square brackets. For the ANSYS solid element, the given result is the arithmetic mean of the displacement values of all the nodes in the end cross section of the beam. All shear correction factors are set to one

Element (#)	$u_x$ (m)	$u_y$ (m)
3363c [128]	-0.15552	-0.70955
34X3c [128]	-0.15722	-0.71466
3333s [128]	-0.15097	-0.71057
3333c [128]	-0.15828	-0.71606
ANSYS SOLID95 [134×34×7]	-0.14759	-0.71479
ANSYS BEAM188 [128]	-0.15161	-0.71130

ence results for all considered ANCF elements. This unresolved issue has also been previously observed for different two-node higher-order elements [22]. In the interest of clarity, the following numerical examples will again focus on the elements 3363c and 34X3c, with most attention being drawn to element 3363c since it seems to have good numerical properties without the high number of degrees of freedom of element 34X3c.

#### 4.4 Large displacement cantilever problem

The preceding numerical results focused on linearized dynamics or problems where nonlinear effects were negligible. Thus, in the following, two numerical tests relying on nonlinear effects are conducted. The first one is again a cantilever with one-dimensional loading at the tip of the beam, but this time, the parameters are chosen in such a way that large deformations can be observed. The same large displacement cantilever test was for instance examined in [3] and [17]. The cantilever is of the length  $L = 2$  m with a rectangular cross section of the width  $W = 0.1$  m and height  $H = 0.5$  m. Young's modulus amounts to  $E = 2.07 \times 10^{11}$  N/m<sup>2</sup> and Poisson's ratio is  $\nu = 0.3$ . The tip load acts in  $y$ -direction and amounts to  $F_y = -6.25 \times 10^6$  N. The numerical results are shown in Table 5.

As can be seen from the results, all considered ANCF elements deliver reasonable results, with the structural mechanics-based element 3333s being closer to the ANSYS beam element solution than to the solid element solution. Therefore, at least in one-dimensional bending, both the lower and the higher-order three-node elements seem to perform as desired.

For this reason, in order to gain insight into possible differences of the elements, a more sophisticated load case involving two-dimensional bending will be considered next.

#### 4.5 Princeton beam experiment

In the following, the above-mentioned beam elements are tested in the so-called Princeton beam experiment. In this experiment, originally conducted physically by researchers from Princeton University [5], again, a slender cantilevered beam is subjected to a concentrated tip load. This time, however, the angle of the tip force is varied. In the original experiment, this was done by rotating the beam. In the numeric experiment undertaken here, the angle of the force is changed directly, which simplifies implementation without changing the results. The forces applied lead to interesting load cases with large deformation bidirectional bending. Therefore, in this experiment, also the nonlinear capabilities of the considered elements are put to the test, while the parameters are still rooted in a physical experiment for which a multitude of measurements has been performed [4]. For this reason, this experiment has already been used as a benchmark problem for numerical tests both of different ANCF elements and of other beam formulations [1]. The numerical values used for the parameters are the same as those used in [1]. The beam of the length  $L = 0.508$  m has a rectangular cross section of the height  $H = 12.377 \times 10^{-3}$  m and width  $W = 3.2024 \times 10^{-3}$  m. Young's modulus amounts to  $E = 71.7 \times 10^9$  N/m<sup>2</sup> and Poisson's ratio is set to  $\nu = 0.31$ . Again, all possible shear correction factors are set to 1. The numerical calculations are done for three distinct absolute values of the

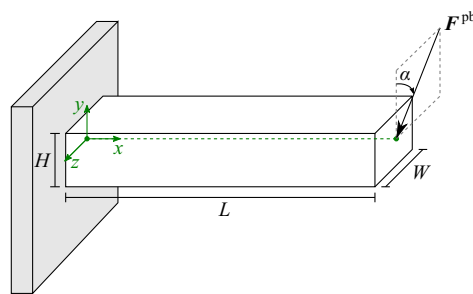
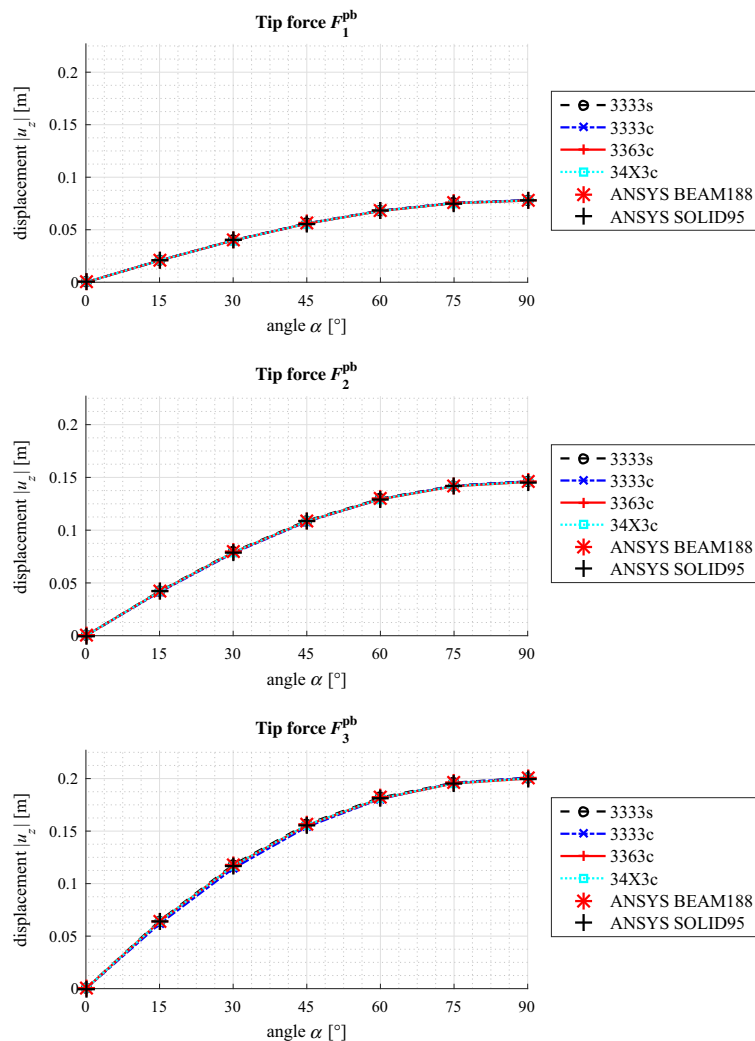


**Fig. 7** Schematic illustration of the Princeton beam experiment in reference configuration with the concentrated tip load  $F^{pb}$

**Fig. 8** Chordwise displacements of the Princeton beam experiment. For the ANSYS solid element, the given result is the arithmetic mean of the displacement values of all the nodes in the end cross section of the beam



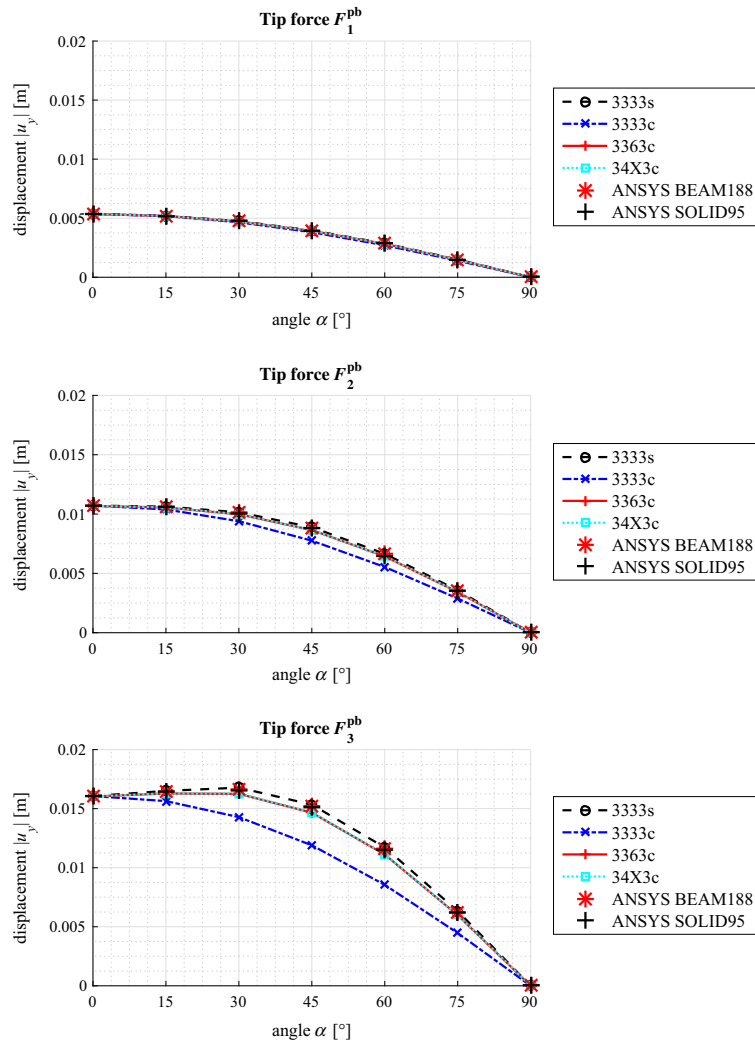
tip load, namely  $F_1^{pb} = 4.448$  N,  $F_2^{pb} = 8.896$  N and  $F_3^{pb} = 13.345$  N. The angle  $\alpha$  is defined as the angle between the force vector and the y-axis with  $\alpha = 0^\circ$  meaning that the force is acting in the negative y-direction. The angles considered vary in  $15^\circ$  steps from  $\alpha = 0^\circ$  to  $\alpha = 90^\circ$ . The setup is illustrated in Fig. 7.

The numerical results for chordwise and flapwise displacements can be found in Figs. 8 and 9. For the calculation, 96 lower-order ANCF elements have

been used. For the elements 3363c and 34X3c, 48 and 24 elements have been employed, respectively. The reference results have been obtained with a mesh of  $160 \times 8 \times 2$  elements in the case of SOLID95 and with 64 of the beam elements.

As can be seen immediately from the results, elements 3363c, 34X3c and 3333s are in good agreement with the reference results with the two higher-order elements performing almost identically to one another. With respect to the chordwise displacements,

**Fig. 9** Flapwise displacements of the Princeton beam experiment. For the ANSYS solid element, the given result is the arithmetic mean of the displacement values of all the nodes in the end cross section of the beam



the differences between all elements are negligible. Of particular interest is the fact that, for the largest tip load, as  $\alpha$  increases from  $0^\circ$  to around  $30^\circ$ , also the flapwise displacement  $u_y$  increases. So although the force in  $y$ -direction decreases, the displacement increases. This is an inherently nonlinear phenomenon and thus not reproducible by any kind of linear theory. In this context, it is rather unsurprising that the differences that indeed exist between the aforementioned

elements can mainly be seen around the discussed  $30^\circ$  peak of the flapwise displacement. As pointed out before, this may be rooted in the fact that only in the derivation of the higher-order ‘c’ elements, the Poisson effect is fully incorporated. The results obtained with the ANSYS elements SOLID95 and BEAM188 are always in between those of the elements 3363c and 3333s with the higher-order results being closer to the SOLID95 result than to the BEAM188 result.

**Table 6** Flapwise displacements  $u_y$  (m) using different numbers of elements for the Princeton beam experiment with force  $F_3^{\text{pb}}$  and  $\alpha = 30^\circ$ 

Number of elements	3333s	3333c	3363c	34X3c
1	-0.015532	-0.014082	-0.007871	-0.013552
2	-0.016678	-0.014265	-0.011482	-0.015048
4	-0.016771	-0.014281	-0.013943	-0.015781
8	-0.016777	-0.014283	-0.015549	-0.016095
16	-0.016777	-0.014283	-0.016065	-0.016227
32	-0.016777	-0.014283	-0.016217	-0.016275
48	-0.016777	-0.014283	-0.016252	-0.016286
64	-0.016777	-0.014283	-0.016265	-0.016291
96	-0.016777	-0.014283	-0.016275	-0.016294

The calculations have been performed up to a comparable amount of degrees of freedom for the different elements. For reference, the converged ANSYS results amount to 0.016661 for BEAM188 and 0.016503 for SOLID95

In the case of element 3333c, however, because of the constitutive relations being used for the calculation of the elastic forces, the coupling between axial and transverse normal strains does not seem to be reproduced correctly, gravely deteriorating the results. While this is not a problem for simple one-dimensional bending tests as conducted in [17], a meaningful application to a more demanding load cases like the Princeton beam experiment is rendered impossible.

#### 4.6 Convergence analysis

In the numerical examples above, the calculations have been performed with a fixed number of elements, albeit with a number large enough to render the results reliable. For practical use and in order to detect possible remaining locking phenomena, however, it is of great importance to illustrate convergence rates. For the reasons described before, the most interesting load case for this analysis seems to be the Princeton beam experiment with a tip load of  $F_3^{\text{pb}}$  and an angle of  $\alpha = 30^\circ$ . Table 6 depicts the results for the flapwise displacement  $u_y$  using increasing numbers of elements.

In Fig. 10, the relative errors are visualized for the different numbers of elements used. As can be seen immediately, the two elements of order 3 exhibit a better rate of convergence in this bidirectional loading test. However, as explained before, element 3333c converges against an incorrect value, and thus, the high rate of convergence is not of much use. In effect, for the

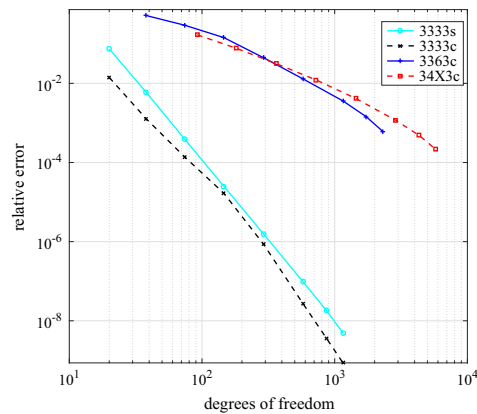


**Fig. 10** Relative errors obtained in the numerical calculation of the flapwise displacement in the Princeton beam experiment with an angle of  $\alpha = 30^\circ$  and a force of  $F_3^{\text{pb}}$ . For the calculation of the relative error, the result obtained with the largest number of elements depicted in Table 6 was used as a reference value for the respective elements. Hence, since only relative errors are shown, it should be noted that the results of element 3333c converge against an incorrect value

lower-order elements, only the structural mechanics-based element delivers reasonable results. However, this comes with the typical disadvantages of structural elements, namely the hardship of incorporating alternative material laws, since material laws known from general continuum mechanics cannot be implemented as straight-forwardly as for elements based on full three-dimensional elasticity.

On the other hand, the considered higher-order elements, although making use of full three-dimensional elasticity, converge against a reasonable value. Nevertheless, there is a considerable increase in the necessary calculation effort when compared to the structural 3333s element.

## 5 Conclusions

In applications of linear ANCF elements that make use of the St. Venant–Kirchhoff material law, it has previously been observed that the attainable accuracy is severely hampered by Poisson locking. For three-node beam elements, this phenomenon can be prevented by certain modifications and selective integration in the calculation of the elastic forces [7]. However, this study shows that these measures still do not help to produce correct results in bidirectional load cases like the Princeton beam experiment.

This paper introduced various higher-order ANCF beam elements and examined them systematically focusing on three-node beam elements. The introduced higher-order elements were carefully verified using a variety of benchmark problems. Having proven their reliability in a small displacement cantilever test, an eigenfrequency analysis of the linearized dynamics was undertaken, highlighting certain advantages of higher-order three-node beam elements. In further tests, it was observed that higher-order beam elements providing at least second-order approximations in transversal directions are indeed capable of eliminating Poisson locking while maintaining performance in the challenging Princeton beam experiment. Additionally, a higher-order four-node element was introduced and investigated, showing that these positive properties can in principle be preserved for beam elements with more nodes.

All things considered, the three-node higher-order element denoted by the identifier 3363c was shown to give reasonable results in all conducted nonlinear tests while maintaining still usable convergence rates. Having ensured performance in conventional load cases, further research might be concerned with the performance of these or similar elements in practical applications like rotor dynamics where the additional higher-order deformation modes could be beneficial in recreating deformations caused by centrifugal forces.

**Acknowledgements** The authors would like to thank the Academy of Finland (Application No. 259543 for the funding of Postdoctoral Researchers and Application No. 285064) for supporting Marko K. Matikainen.

## References

1. Bauchau, O.A., Han, S., Mikkola, A., Matikainen, M.K., Gruber, P.: Experimental validation of flexible multibody dynamics beam formulations. *Multibody Syst. Dyn.* **34**(4), 373–389 (2015)
2. Dmitrochenko, O., Mikkola, A.: Digital nomenclature code for topology and kinematics of finite elements based on the absolute nodal co-ordinate formulation. *Proc. Inst. Mech. Eng., Part K: J. Multi-Body Dyn.* **225**(1), 34–51 (2011)
3. Dufva, K.E., Sopanen, J.T., Mikkola, A.M.: A two-dimensional shear deformable beam element based on the absolute nodal coordinate formulation. *J. Sound Vib.* **280**(3), 719–738 (2005)
4. Dowell, E.H., Traybar, J.J.: An addendum to AMS report no 1194 entitled an experimental study of the nonlinear stiffness of a rotor blade undergoing flap, lag, and twist deformations. Technical Report 1257, AMS Report, December (1975)
5. Dowell, E.H., Traybar, J.J.: An experimental study of the nonlinear stiffness of a rotor blade undergoing flap, lag and twist deformations. Technical Report 1194, AMS Report, January (1975)
6. Gerstmayr, J., Matikainen, M.K.: Analysis of stress and strain in the absolute nodal coordinate formulation. *Mech. Based Des. Struct. Mach.* **34**(4), 409–430 (2006)
7. Gerstmayr, J., Matikainen, M.K., Mikkola, A.M.: A geometrically exact beam element based on the absolute nodal coordinate formulation. *Multibody Syst. Dyn.* **20**(4), 359–384 (2008)
8. Gerstmayr, J., Shabana, A.A.: Efficient integration of the elastic forces and thin three-dimensional beam elements in the absolute nodal coordinate formulation. In: *Multibody Dynamics 2005, ECCOMAS Thematic Conference, Madrid, Spain, 21–24 June 2005*
9. Gerstmayr, J., Shabana, A.A.: Analysis of thin beams and cables using the absolute nodal co-ordinate formulation. *Nonlinear Dyn.* **45**(1), 109–130 (2006)
10. Humer, A.: Dynamic modeling of beams with non-material, deformation-dependent boundary conditions. *J. Sound Vib.* **332**(3), 622–641 (2013)
11. Kerkkänen, K.S., García-Vallejo, D., Mikkola, A.M.: Modeling of belt-drives using a large deformation finite element formulation. *Nonlinear Dyn.* **43**(3), 239–256 (2006)
12. Matikainen, M.K., Dmitrochenko, O.: A study of three-node higher-order gradient beam elements based on the absolute nodal coordinate formulation. In: *The 3rd Joint International Conference on Multibody System Dynamics, Busan, Korea (2014)*
13. Matikainen, M.K., Dmitrochenko, O., Mikkola, A.: Beam elements with trapezoidal cross section deformation modes based on the absolute nodal coordinate formulation. In: *International Conference of Numerical Analysis and Applied Mathematics, Rhodes, Greece, 19–25 Sept 2010*

14. Matikainen, M.K., Dmitrochenko, O., Mikkola, A.: Higher order beam elements based on the absolute nodal coordinate formulation. In: *Multibody Dynamics 2011, ECCO-MAS Thematic Conference*, 4–7 July 2011
15. Matikainen, M.K., Dmitrochenko, O., Mikkola, A.: Higher order beam elements based on the absolute nodal coordinate formulation. *Multibody Dynamics* (2011)
16. Matikainen, M.K., Valkeapää, A.I., Mikkola, A.M., Schwab, A.L.: A study of moderately thick quadrilateral plate elements based on the absolute nodal coordinate formulation. *Multibody Syst. Dyn.* **31**(3), 309–338 (2014)
17. Nachbagauer, K., Gruber, P., Gerstmayr, J.: A 3d shear deformable finite element based on the absolute nodal coordinate formulation. In: Samin, Jean-Claude, Fiset, Paul (eds.) *Multibody Dynamics. Computational Methods in Applied Sciences*, vol. 28, pp. 77–96. Springer, Netherlands (2013)
18. Olshevskiy, A., Dmitrochenko, O., Kim, C.-W.: Three-dimensional solid brick element using slopes in the absolute nodal coordinate formulation. *J. Comput. Nonlinear Dyn.* **9**(2), 021001 (2014)
19. Orzechowski, G., Fraczek, J.: Nearly incompressible nonlinear material models in the large deformation analysis of beams using ANCF. *Nonlinear Dyn.* **82**(1), 451–464 (2015)
20. Orzechowski, G., Shabana, A.A.: Analysis of warping deformation modes using higher order ANCF beam element. *J. Sound Vib.* **363**, 428–445 (2016)
21. Shabana, A.A.: Definition of the slopes and the finite element absolute nodal coordinate formulation. *Multibody Syst. Dyn.* **1**, 339–348 (1997)
22. Shen, Z., Li, P., Liu, C., Hu, G.: A finite element beam model including cross-section distortion in the absolute nodal coordinate formulation. *Nonlinear Dyn.* **77**(3), 1019–1033 (2014)
23. Sugiyama, H., Mikkola, A.M., Shabana, A.A.: A non-incremental nonlinear finite element solution for cable problems. In: *ASME 2003 International Design Engineering Technical Conferences and Computers and Information in Engineering Conference*, pp. 171–181. American Society of Mechanical Engineers (2003)
24. Valkeapää, A.I., Matikainen, M.K., Mikkola, A.M.: Meshing strategies in the absolute nodal coordinate formulation-based Euler-Bernoulli beam elements. *Proc. Inst. Mech. Eng., Part K: J. Multi-Body Dyn.* **230**(4), 606–614 (2016)
25. Wang, C.M., Reddy, J.N., Lee, K.H.: *Shear Deformable Beams and Plates*. Elsevier, Amsterdam (2000)



## Publication III

Ebel, H., Matikainen, M.K., Hurskainen, V-V., Mikkola, A.  
**Analysis of high-order quadrilateral plate elements based on the  
absolute nodal coordinate formulation for three-dimensional  
elasticity**

Reprinted from  
*Advances in Mechanical Engineering*  
Vol. 9(6), June 2017  
© 2017, the authors



# Analysis of high-order quadrilateral plate elements based on the absolute nodal coordinate formulation for three-dimensional elasticity

Henrik Ebel<sup>1</sup>, Marko K Matikainen<sup>2</sup>, Vesa-Ville Hurskainen<sup>2</sup> and Aki Mikkola<sup>2</sup>

## Abstract

The absolute nodal coordinate formulation is a computational approach to analyze the dynamic performance of flexible bodies experiencing large deformations in multibody system dynamics applications. In the absolute nodal coordinate formulation, full three-dimensional elasticity can be used in the definition of the elastic forces. This approach makes it straightforward to implement advanced material models known from general continuum mechanics in the absolute nodal coordinate formulation. As, however, pointed out in the literature, the use of full three-dimensional elasticity can lead to severe locking problems, already present in simple, static tests. To overcome these drawbacks and to get a better understanding of these behaviors in the case of absolute nodal coordinate formulation elements, this study introduces and carefully analyses several high-order three-dimensional plate elements based on the absolute nodal coordinate formulation, primarily in meaningful static scenarios. The proposed elements are put to test in various numerical experiments intended to bring forward possible locking phenomena and to evaluate the accuracy attainable with the considered element formulations. The proposed eight- and nine-node elements that incorporate polynomial approximations of second order in all three directions prove to be advantageous both with respect to the actual performance and with regard to the numerical efficiency when compared to other absolute nodal coordinate formulation plate elements. A comparison with a four-node high-order element corroborates the supposition that the usage of in-plane slopes as nodal coordinates has a negative effect on numerical convergence properties in thin-plate use cases. An additional example showcases the functioning of two of the higher-order elements in a dynamic simulation.

## Keywords

Continuum plate elements, three-dimensional elasticity, St. Venant–Kirchhoff material, Princeton beam experiment, numerical locking

Date received: 16 January 2017; accepted: 23 March 2017

Academic Editor: Xiaoting Rui

## Introduction

The absolute nodal coordinate formulation (ANCF) is a nonlinear finite element-based approach that is designed to describe flexible bodies undergoing large displacements and rotations in multibody system dynamics applications.<sup>1</sup> In the ANCF, the kinematics of the finite element is defined by employing the spatial

<sup>1</sup>Institute of Engineering and Computational Mechanics, University of Stuttgart, Stuttgart, Germany

<sup>2</sup>Mechanical Engineering, Lappeenranta University of Technology, Lappeenranta, Finland

### Corresponding author:

Marko K Matikainen, Mechanical Engineering, Lappeenranta University of Technology, Skinnarilankatu 34, 53850 Lappeenranta, Finland.  
Email: marko.matikainen@lut.fi



Creative Commons CC-BY: This article is distributed under the terms of the Creative Commons Attribution 4.0 License (<http://www.creativecommons.org/licenses/by/4.0/>) which permits any use, reproduction and distribution of the work without further permission provided the original work is attributed as specified on the SAGE and Open Access pages (<https://us.sagepub.com/en-us/nam/open-access-at-sage>).

shape functions together with the element nodal coordinates. The nodes of the elements are located on the centerline for beams or on the mid-plane for plates. Contrary to beam and plate elements in traditional finite element analysis, ANCF beam and plate elements are described using absolute nodal positions and their derivatives. Using the components of the deformation gradient instead of the rotation angles as degrees of freedom, large three-dimensional rotations can be described without the singularity problems in a total Lagrangian formulation. Additionally, this choice of nodal coordinates leads to a constant mass matrix, which is computationally beneficial especially when employing explicit time integration schemes. With a properly selected material model and a suitable strain description, the ANCF can capture nonlinear strain-displacement relationships as well as material nonlinearities. For a more detailed discussion of the definition of ANCF elements, see Shabana.<sup>2</sup>

The elastic forces can be defined using either structural-based approaches, which handle strain components independently, or full three-dimensional elasticity, for instance in the form of the St. Venant-Kirchhoff material law. However, the elastic forces must be defined with care as the use of full three-dimensional elasticity in conjunction with improper interpolations and choice of slope vectors has been demonstrated to be vulnerable for various locking phenomena. The shear-deformable four-node quadrilateral ANCF plate element proposed in Mikkola and Shabana,<sup>3</sup> for instance, suffers from transverse shear locking and Poisson locking. Poisson locking can be eliminated using the structural mechanics-based approach for the calculation of the elastic forces. With respect to advanced material modeling, however, the use of full three-dimensional elasticity is superior when compared to the structural-based approach. Accordingly, by eliminating drawbacks associated with the use of full three-dimensional elasticity, ANCF offers a straightforward platform for dynamic analysis based on advanced material models in the context of multibody systems. It is for this reason that the research of approaches to eliminate locking phenomena also for full three-dimensional elasticity is justified.

Kuhl and Ramm<sup>4</sup> give an overview of locking phenomena in traditional finite element analysis and existing techniques to prevent these phenomena. Apart from other strategies, it is mentioned that a natural approach to avoid locking phenomena is to develop high-order elements. Since ANCF elements are often quite closely related to their traditional finite element counterparts, it makes sense to consider this possibility also in the realm of ANCF. In the case of ANCF elements, higher approximation orders can be achieved using more nodes per element, by employing high-order

derivatives as nodal coordinates, or using a combination of the two. This high-order approach has been examined thoroughly for ANCF beam elements, but comparatively little attention has been devoted to three-dimensional quadrilateral high-order plate elements. For the purpose of this article, elements are said to be of high order if they employ high-order derivatives as nodal coordinates.

Concerning ANCF beam elements, in Gerstmayr and Shabana,<sup>5</sup> the deterioration of the speed of convergence as a result of shear locking has been alleviated by enriching the polynomial basis with respect to the longitudinal coordinate. To reduce the influence of Poisson locking in the case of ANCF beam elements, Matikainen et al.<sup>6,7</sup> have proposed to include the trapezoidal cross-section mode using a second-order transversal derivative as a nodal coordinate. In Ebel et al.<sup>8</sup> and Shen et al.,<sup>9</sup> many high-order beam elements were studied to demonstrate the above-mentioned locking problems.

Regarding plate elements, Olshevskiy et al.<sup>10</sup> introduce a triangular two-dimensional ANCF plate element making use of a second-order mixed derivative as an additional nodal coordinate. The numerical performance of further high-order triangular plate elements has also been investigated by Olshevskiy et al.<sup>11</sup> Matikainen et al.<sup>12</sup> have examined various quadrilateral ANCF plate elements, including one high-order four-node element that uses a second-order displacement interpolation in the thickness direction to successfully overcome Poisson locking. However, the element still suffers from an additional shear locking phenomenon limiting the numerical performance in the case of thin plates. There is a perception that the use of in-plane slope vectors together with derivatives in transversal directions in the nodal coordinates contributes to this problem. In previous studies, an approach that does not employ in-plane slope vectors has delivered promising results for three-node ANCF beam elements that make use of the St. Venant-Kirchhoff material law.<sup>8</sup>

The objective of this article is to extend this recently introduced approach of the usage of a high polynomial order in all three directions without the use of in-plane slopes to plate applications. This extension makes it possible to employ full three-dimensional elasticity in the definition of the elastic forces. This, in turn, allows the implementation of advanced material models in the ANCF in a straightforward manner. To reach this objective, this article introduces eight- and nine-node high-order ANCF plate elements. The performance of the elements is systematically compared to low- and high-order four-node elements in several static tests that are designed to focus on certain locking phenomena. Furthermore, a dynamic test exemplifies the usage of two of the functioning higher-order elements in simulations over the time domain.

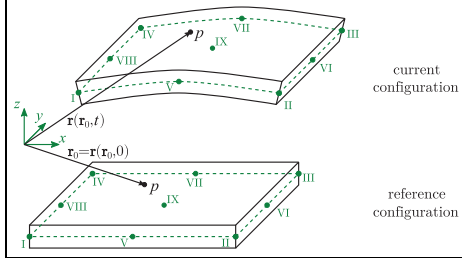


**Figure 1.** Illustration of a nine-node plate element with a particle  $p$  in reference and in current configuration. The nodes are denoted by I, II, ..., IX. For plate elements with fewer nodes, the nodes with higher numbers are omitted.

### Definition of the considered ANCF plate elements

In the ANCF, the current position of an arbitrary particle  $r \in \mathbb{R}^3$  at time  $t \in \mathbb{R}_0^+$  can be written as

$$\mathbf{r}(\mathbf{x}, t) = \mathbf{S}(\mathbf{x})\mathbf{e}(t) \quad (1)$$

where  $\mathbf{S}(\mathbf{x})$  is the shape function matrix and  $\mathbf{e}(t)$  is the vector of nodal coordinates. The vector  $\mathbf{x}$  denotes the position of the considered particle in the reference configuration, and thus, the identity

$$\mathbf{r}_0 := \mathbf{r}(\mathbf{x}, 0) = \mathbf{x}$$

holds.

In this article, various plate elements with eight and nine nodes will be considered. For comparison purposes, some results obtained with four-node elements will also be given. An exemplary nine-node element is illustrated in Figure 1.

For a plate element with  $b$  nodes, the vector of nodal coordinates can be written as

$$\mathbf{e} = [\mathbf{e}_I^T \mathbf{e}_{II}^T \dots \mathbf{e}_b^T]^T \quad (2)$$

With  $\mathbf{e}_i$ ,  $i \in \{I, II, \dots, b\}$ , being the nodal coordinate vector of the  $i$ th node. The nodal coordinates can contain the positions  $\mathbf{r}$  of the element's nodes in the inertial frame of reference and selected spatial derivatives of these position vectors. For the sake of readability, for the spatial derivatives, the shorthand notations

$$\mathbf{r}_{,x} := \frac{\partial \mathbf{r}}{\partial x}, \mathbf{r}_{,y} := \frac{\partial \mathbf{r}}{\partial y}, \mathbf{r}_{,z} := \frac{\partial \mathbf{r}}{\partial z}, \mathbf{r}_{,zz} := \frac{\partial^2 \mathbf{r}}{\partial z^2}$$

will be used in the formulation of the considered elements.

One possibility to derive the shape function matrix  $\mathbf{S}$  is to employ a polynomial basis to approximate the particle positions of the considered element. In ANCF, the same basis is used for all three dimensions.<sup>1</sup> Assuming that a monomial basis consisting of  $p$  monomials is

used and that the vector  $\mathbf{b}_p(\mathbf{x}) \in \mathbb{R}^{1 \times p}$  contains all of these monomials, the polynomial expansion can be written as

$$\mathbf{r}(\mathbf{x}, t) = \begin{bmatrix} \mathbf{b}_p(\mathbf{x}) & \mathbf{0} & \mathbf{0} \\ \mathbf{0} & \mathbf{b}_p(\mathbf{x}) & \mathbf{0} \\ \mathbf{0} & \mathbf{0} & \mathbf{b}_p(\mathbf{x}) \end{bmatrix} \mathbf{c}(t) =: \mathbf{P}(\mathbf{x})\mathbf{c}(t) \quad (3)$$

where  $\mathbf{c}$  is the vector of polynomial coefficients. Substituting the reference positions of the nodes into equation (3) and into those spatial derivatives of equation (3) that are used as nodal coordinates directly gives a linear relationship

$$\mathbf{e}(t) = \mathbf{T}\mathbf{c}(t) \quad (4)$$

between the polynomial coefficients and the nodal coordinates. Hence, if the polynomial basis has been chosen in a way that  $\mathbf{T}$  is invertible, the shape function matrix reads

$$\mathbf{S}(\mathbf{x}) = \mathbf{P}(\mathbf{x})\mathbf{T}^{-1} \quad (5)$$

Therefore, given a specific type of element with a specified number and arrangement of nodes, the shape function matrix is a direct consequence of the chosen polynomial basis and the chosen set of nodal coordinates. Accordingly, the subsequent section deals with the introduction of various ANCF plate elements by giving both the employed polynomial bases and nodal coordinates.

### Derivation of the shape functions

To easily identify the various elements used in this article, a four-digit code similar to the one introduced in Dmitrochenko and Mikkola<sup>13</sup> will be used. For the four digits  $abcd$ ,  $a$  signifies the dimension of the element,  $b$  the number of nodes,  $c$  the number of nodal coordinates per node and dimension and  $d$  will always be of the value 3 in the following, since the same polynomial basis is used for all three dimensions of the element.

In total, seven different ANCF plate elements are considered throughout this article. Table 1 depicts the nodal degrees of freedom and the polynomial bases of all seven elements, using the abbreviations

$$\begin{aligned} \beta_{\text{iin.}} &= \{1, x, y, z, xy, xz, yz, xyz\} \\ \beta_{\text{qx}} &= \{x^2, x^2y, x^2z, x^2yz\} \\ \beta_{\text{qy}} &= \{y^2, xy^2, y^2z, xy^2z\} \\ \beta_{\text{qz}} &= \{z^2, xz^2, yz^2, xyz^2\} \\ \beta_a &= \{x^2y^2, x^2z^2, y^2z^2, x^2y^2z, x^2yz^2, xy^2z^2, x^2y^2z^2\} \\ \beta_b &= \{x^2, y^2, x^3, y^3, x^2y, xy^2, x^3y, xy^3, z^2, xz^2, yz^2, xyz^2\} \\ \beta^{[3933]} &= \beta_{\text{iin.}} \cup \beta_{\text{qx}} \cup \beta_{\text{qy}} \cup \beta_{\text{qz}} \cup \beta_a \end{aligned} \quad (6)$$

**Table 1.** Nodal coordinates and bases of all considered elements.

Element [dof]	Nodal coordinates	Basis	$n_x \times n_y \times n_z$
3933 [81]	$\mathbf{r}, \mathbf{r}_z, \mathbf{r}_{zz}$	$\beta^{[3933]}$	$5 \times 5 \times 5$
3923 [54]	$\mathbf{r}, \mathbf{r}_z$	$\beta_{lin.} \cup \beta_{qx} \cup \beta_{qy} \cup \{x^2y^2, x^2y^2z\}$	$5 \times 5 \times 3$
3833 [72]	$\mathbf{r}, \mathbf{r}_z, \mathbf{r}_{zz}$	$\beta^{[3933]} \setminus \{x^2y^2, x^2y^2z, x^2y^2z^2\}$	$5 \times 5 \times 5$
3823 [48]	$\mathbf{r}, \mathbf{r}_z$	$\beta_{lin.} \cup \beta_{qx} \cup \beta_{qy}$	$5 \times 5 \times 3$
3453 [60]	$\mathbf{r}, \mathbf{r}_x, \mathbf{r}_y, \mathbf{r}_z, \mathbf{r}_{zz}$	$\beta^{[3453]} := \beta_{lin.} \cup \beta_b$	$7 \times 7 \times 5$
3443 [48]	$\mathbf{r}, \mathbf{r}_x, \mathbf{r}_y, \mathbf{r}_z$	$\beta^{[3453]} \setminus \{z^2, xz^2, yz^2, xyz^2\}$	$7 \times 7 \times 3$
3423 [24]	$\mathbf{r}, \mathbf{r}_z$	$\beta_{lin.}$	$3 \times 3 \times 3$

The abbreviations used are defined in equation (6). The last column contains the number of integration points used in the evaluation of the elastic forces.

Two of the elements, namely 3933 and 3923, have nine nodes. Element 3933 is characterized by the fact that it uses an approximation of order 2 in all three directions. Element 3923 employs linear polynomials for the approximation in the  $z$  direction. Furthermore, two eight-node elements 3833 and 3823 are examined. They are similar to their nine-node counterparts, but since they lack a middle node, they make use of a basis containing three monomials less than elements 3933 and 3923, respectively.

For comparison, also the three four-node elements 3453, 3443, and 3423 are considered. Again, element 3453, originally proposed in Matikainen et al.,<sup>12</sup> uses an approximation of order 2 in the  $z$  direction, while element 3443 is linear in the  $z$  direction. On the other hand, element 3423, which is purely considered for demonstrative purposes, is linear in all directions.

For eight-node elements, there are, in theory, many different possibilities to choose valid bases in the sense that the matrix  $\mathbf{T}$  from equation (4) is invertible. In this study, the two bases were chosen in such a way that the basis of the two-dimensional serendipity element Q8 from conventional finite element analysis is a subset of the bases of both element 3833 and element 3823.

The shape function matrices for all above-mentioned elements can now be calculated using equation (5). The shape functions can be given either in physical coordinates  $\mathbf{x} = [x, y, z]^T$  or in local element coordinates  $\xi = [\xi, \eta, \zeta]^T$ . In this study, the latter ones are scaled so that  $-1 \leq \xi, \eta, \zeta \leq 1$ . For a nine-node plate element, this is illustrated in Figure 2.

### Calculation of the elastic forces

In this paper, all considered elements make use of the St. Venant–Kirchhoff material law which assumes a linear relationship between the Green–Lagrange strain tensor  $\mathbf{E}$  and the second Piola–Kirchhoff stress tensor  $\mathbf{S}^{PK}$ .<sup>5</sup> For implementation purposes, the integration to calculate the elastic forces is evaluated using Gaussian quadrature of a sufficient degree of exactness for all

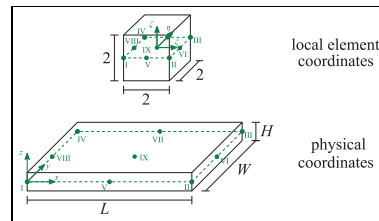


**Figure 2.** Illustration of a nine-node plate element in physical and in local element coordinates.

three dimensions independently. For the purpose of this article, the number of integration points is always set to be large enough such that no additional error is introduced into the calculation, see Table 1.

### Numerical experiments

In this section, the above-mentioned plate elements are put to test in various numerical experiments. The goal of this analysis is to gain insight into which elements deliver accurate results while still maintaining acceptable convergence rates. Of special interest are the questions whether the introduction of second-order  $z$ -derivatives can alleviate certain locking phenomena and whether omitting in-plane slopes is actually beneficial for calculations involving thin plates. The first two tests that are conducted involve small deformations only. This allows for comparisons with approximative analytical solutions in order to eliminate the possibility of any fundamental flaws in element formulation and implementation. After that, two large-displacement tests are conducted. For these tests, reference results are calculated using finite elements provided by the commercial software ANSYS. The elements involved are the solid element SOLID95 and the beam element BEAM188. SOLID95 is a three-dimensional structural solid element with three nodal degrees of freedom for

**Table 2.** Numeric results for the cantilevered plate experiment with Poisson's ratio of  $\nu = 0.3$ .

Element [#, dof]	$u_z^{\text{absmin}}$ (m)	$u_z^{\text{av}}$ (m)	$u_z^{\text{absmax}}$ (m)
3933 [9×18, 5994]	$-1.6840 \times 10^{-5}$	$-1.7415 \times 10^{-5}$	$-1.7679 \times 10^{-5}$
3923 [11×22, 5940]	$-1.3902 \times 10^{-5}$	$-1.4638 \times 10^{-5}$	$-1.4967 \times 10^{-5}$
3833 [10×20, 5580]	$-1.6862 \times 10^{-5}$	$-1.7439 \times 10^{-5}$	$-1.7700 \times 10^{-5}$
3823 [12×24, 5328]	$-1.3906 \times 10^{-5}$	$-1.4644 \times 10^{-5}$	$-1.4972 \times 10^{-5}$
3453 [13×26, 5346]	$-1.6772 \times 10^{-5}$	$-1.7327 \times 10^{-5}$	$-1.7589 \times 10^{-5}$
3443 [15×30, 5673]	$-1.3904 \times 10^{-5}$	$-1.4625 \times 10^{-5}$	$-1.4959 \times 10^{-5}$
3423 [22×44, 5940]	$-2.0257 \times 10^{-6}$	$-2.0513 \times 10^{-6}$	$-2.0667 \times 10^{-6}$
Reference ( $W \rightarrow \infty$ )	$-1.7333 \times 10^{-5}$	$-1.7333 \times 10^{-5}$	$-1.7333 \times 10^{-5}$

The element mesh and numbers of degrees of freedom used are given in square brackets. The values  $u_z^{\text{av}}$  represent the arithmetic means of the displacement values for all nodes at the free end of the plate. On the other hand,  $u_z^{\text{absmin}}$  and  $u_z^{\text{absmax}}$  are the nodal displacements that have the smallest or largest absolute value.

each of its 20 nodes. In general, this element has multiple reference shapes, but for these calculations, hexahedral elements were applied. BEAM188, on the other hand, is a three-dimensional shear-deformable linear beam element with two nodes and 6 degrees of freedom per node. For the calculations in this study, a four-cell cross-section was used. All numeric calculations involving ANCF elements have been performed using MATLAB.

### Cantilevered plate

The first test involves a cantilevered plate of the length  $L = 1$  m, the width  $W = 2$  m, and the thickness  $H = 0.01$  m. Young's modulus amounts to  $E = 210 \times 10^9$  N/m<sup>2</sup>, Poisson's ratio is set to  $\nu = 0.3$ , and the shear modulus is given by  $G = E/(2(1 + \nu))$ . A distributed force of  $F_z = -1$  N/m is applied to the free edge of the mid-surface of the plate. Apart from the width  $W$ , the same cantilevered plate has been studied in Matikainen et al.<sup>12</sup> This setup has the advantage that the obtained results can be compared with an analytical solution for the vertical displacement of the free end of a cantilevered plate of infinite width.<sup>12</sup> This analytical solution is given as

$$u_z^{W \rightarrow \infty} = \frac{12(1 - \nu^2)FL^2}{EH^3} \frac{1}{3} \approx -1.7333 \times 10^{-5} \text{ m} \quad (7)$$

Naturally, since the plate of this experiment has a finite width, one cannot expect a result that is identical to the analytical solution. Nevertheless, the results should still be comparable. In particular, for a finitely wide plate with a non-zero Poisson's ratio, the displacement in the middle of the free end will be larger than in the free corners of the plate. For this reason, the arithmetic means of the vertical displacements of all nodes at the end edge of the cantilever are calculated. Also, in the interest of a more thorough analysis, the nodal

displacements with the smallest and largest absolute values are recorded.

The discretization has been chosen so that, as a first priority, all ANCF plate elements are always square-shaped and, as a second priority, so that the resulting number of degrees of freedom is similar for the different elements. The numeric results are depicted in Table 2.

As can be seen from the results, for elements 3933, 3833, and 3453, the analytical result is well in the range of the nodal displacements. These elements have in common that they employ a second-order approximation in the  $z$  direction. In contrast, all elements that are merely linear in the  $z$  direction deliver inaccurate results. However, since elements 3923, 3823, and 3443 still give similar values when compared with each other, it seems that a common phenomenon must be responsible for the fact that they converge to the wrong value. Indeed, when repeating the experiment with Poisson's ratio set to be equal to zero, also elements 3923, 3823, and 3443 deliver correct results. This can be seen in Table 3.

In conclusion, these elements suffer from Poisson locking, and similar to the findings for beam elements in previous studies, approximations of at least second order in all directions seem to be a functional remedy for Poisson locking.<sup>8</sup> The linear element 3423, however, suffers from a variety of severe locking phenomena and hence delivers results with absolute values that are approximately an order of magnitude smaller than the reference value.

### Simply supported plate under body load

The second numeric experiment is a square, simply supported plate subjected to a body load as previously studied in Matikainen et al.<sup>12</sup> The plate is of the length and width  $L = W = 1$  m, Young's modulus is set to  $E = 2.1 \times 10^{11}$  N/m<sup>2</sup>, and Poisson's ratio is  $\nu = 0.3$ . The calculations are performed for three different

**Table 3.** Numeric results for the cantilevered plate experiment with Poisson's ratio of  $\nu = 0$ .

Element [#, dof]	$u_z^{\text{absmin}}$ (m)	$u_z^{\text{av}}$ (m)	$u_z^{\text{absmax}}$ (m)
3933 [9×18, 5994]	$-1.8994 \times 10^{-5}$	$-1.8994 \times 10^{-5}$	$-1.8994 \times 10^{-5}$
3923 [11×22, 5940]	$-1.9013 \times 10^{-5}$	$-1.9013 \times 10^{-5}$	$-1.9013 \times 10^{-5}$
3833 [10×20, 5580]	$-1.9005 \times 10^{-5}$	$-1.9005 \times 10^{-5}$	$-1.9005 \times 10^{-5}$
3823 [12×24, 5328]	$-1.9020 \times 10^{-5}$	$-1.9020 \times 10^{-5}$	$-1.9020 \times 10^{-5}$
3453 [13×26, 5346]	$-1.9020 \times 10^{-5}$	$-1.9020 \times 10^{-5}$	$-1.9020 \times 10^{-5}$
3443 [15×30, 5673]	$-1.9027 \times 10^{-5}$	$-1.9027 \times 10^{-5}$	$-1.9027 \times 10^{-5}$
3423 [22×44, 5940]	$-1.6812 \times 10^{-6}$	$-1.6812 \times 10^{-6}$	$-1.6812 \times 10^{-6}$
Reference ( $W \rightarrow \infty$ )	$-1.9048 \times 10^{-5}$	$-1.9048 \times 10^{-5}$	$-1.9048 \times 10^{-5}$

**Table 4.** Results for the center displacements of the simply supported plate under body load for various thickness values.

Element [#, dof]	$u_z, H_1 = 0.1$ m	$u_z, H_2 = 0.01$ m	$u_z, H_3 = 0.005$ m
3933 [16×16, 9541]	1.0782	1.0019	0.9995
3923 [20×20, 9762]	0.8722	0.8183	0.8165
3833 [18×18, 9113]	1.0787	1.0025	0.9999
3823 [22×22, 8890]	0.8723	0.8186	0.8166
3453 [24×24, 9179]	1.0717	1.0002	0.9963
3443 [28×28, 9864]	0.8693	0.8171	0.8151
3423 [40×40, 9762]	0.8631	0.4344	0.1801

The results are normalized with respect to the reference values of  $-1.1018 \times 10^{-6}$  m,  $-1.0567 \times 10^{-6}$  m, and  $-1.0563 \times 10^{-6}$  m for  $H_1, H_2$ , and  $H_3$ .

thickness values, namely  $H_1 = 0.1$  m,  $H_2 = 0.01$  m, and  $H_3 = 0.005$  m. The uniform body load amounts to

$$\mathbf{b} = [0 \quad 0 \quad -5 \times 10^6 \cdot H_i^2]^T$$

for the respective thickness values. The setup is illustrated in Figure 3.

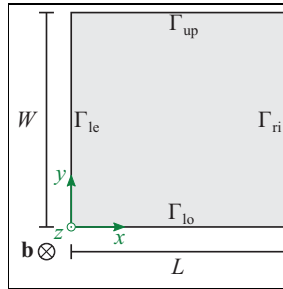
The boundary conditions are given by

$$\begin{aligned} (\mathbf{r})_{1,3}|_{\Gamma_{lc}} &= \mathbf{0}, (\mathbf{r})_{1,3}|_{\Gamma_{ri}} = \mathbf{0} \\ (\mathbf{r})_{2,3}|_{\Gamma_{lo}} &= \mathbf{0}, (\mathbf{r})_{2,3}|_{\Gamma_{up}} = \mathbf{0} \end{aligned} \quad (8)$$

The displacements are recorded in the middle of the plate. Once again, there exists a thin-plate analytical solution for this problem. Using Reissner–Mindlin plate theory,<sup>12</sup> this analytical solution of the  $z$  displacement in the middle of the plate is of the form

$$\begin{aligned} u_z^{\text{RM}} &= \frac{12(1-\nu^2)}{\pi^4 E H_i^3} \sum_{p=1}^{\infty} \sum_{q=1}^{\infty} \left[ \frac{\sin(p\pi/2) \sin(q\pi/2) 4b_3 H_i}{(p^2/L^2 + q^2/W^2)^2 \pi^2 p q} (1 - \cos(\pi p))(1 - \cos(\pi q)) \right] \\ &+ \frac{1}{G H_i \pi^2} \sum_{p=1}^{\infty} \sum_{q=1}^{\infty} \left[ \frac{\sin(p\pi/2) \sin(q\pi/2) 4b_3 H_i}{p^2/L^2 + q^2/W^2 \pi^2 p q} (1 - \cos(\pi p))(1 - \cos(\pi q)) \right] \end{aligned} \quad (9)$$

The results are given in Table 4. The reference values given have been obtained by evaluating the sums in equation (9) up to  $p = q = 1024$ , which gives results

**Figure 3.** Illustration of the setup for the simply supported plate.

that can be considered as exact with respect to the given accuracy.

As can be gathered from the results for all three thickness values, the simply supported plate experiment reinforces the impressions from the previous test. Once more, the elements 3933, 3833, and 3453 deliver correct

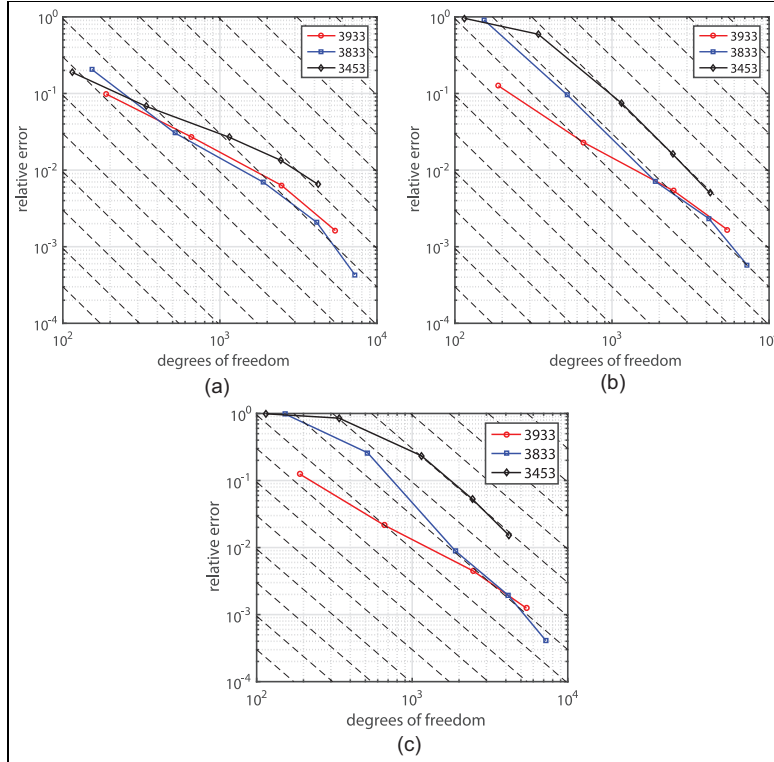


**Figure 4.** In this figure, the relative errors of the displacement results of the simply supported plate under body load are plotted for different numbers of elements. For the calculation of the relative error, the values given in Table 4 were used as the respective reference solutions: (a)  $H_1 = 0.1$  m, (b)  $H_2 = 0.01$  m, and (c)  $H_3 = 0.005$  m.

results. The elements 3923, 3823, 3443, and 3423, on the other hand, are once again incapable of delivering correct displacements. Thus, in the interest of clarity, the remainder of this article will show only results of the three better-performing ANCF elements.

In practical applications, it is not only important that the numerical solution converges to a correct value for increasing numbers of elements, but rather that a satisfactory solution can already be obtained for a modest number of degrees of freedom. Therefore, in the following, the convergence rates for elements 3933, 3833, and 3453 will be investigated. Figure 4(a) and (b) show the relative errors for the thicknesses  $H_1$  and  $H_2$ .

While for  $H_1 = 0.1$  m, the three elements exhibit quite similar convergence behaviors, for the thinner plate of thickness  $H_2 = 0.01$  m, element 3453 seems to suffer from a locking phenomenon, since for the first few hundred degrees of freedom, the convergence rate is noticeably decreased. This can already be of practical

relevance. While element 3933 delivers quite reasonable results for less than 2000 degrees of freedom with a relative error noticeably below 1%, element 3453 needs approximately twice as many degrees of freedom to achieve a relative error as small as that.

Even more so, when using exact Gaussian quadrature for all elements, the computation effort per degree of freedom for calculations with element 3453 is larger than for elements 3933 and 3833. The reason for this lies in the fact that the basis used for element 3453 contains monomials up to the third order of  $x$  while the other two elements only use monomials up to second order. Hence, for an exact quadrature, element 3453 needs to use more integration points in the  $x$  direction.

Furthermore, as demonstrated by Figure 4(c), this locking phenomenon is even more severe for the thinnest considered plate of thickness  $H_3 = 0.005$  m. This phenomenon is usually referred to as shear locking or transverse shear locking in the literature since it

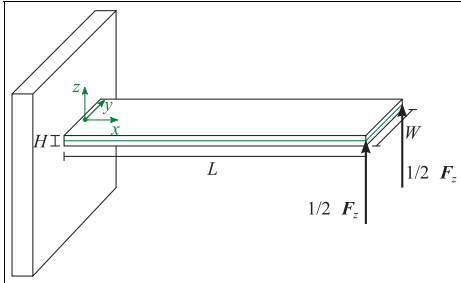


**Figure 5.** Illustration of the setup for the large-displacement cantilever experiment for a total applied force of  $F_z$ .

involves artificial shear strains that render the element to be overly stiff. In conventional finite element analysis, this phenomenon appears for instance in linear plate elements since then linear shape functions are used for both displacements and rotations and thus, pure bending cannot be replicated without artificial shear strains.<sup>14</sup>

However, as the presented results suggest, in the case of ANCF plate elements, it seems that this phenomenon is also connected to the usage of the in-plane slope vectors  $\mathbf{r}_x$  and  $\mathbf{r}_y$  as nodal coordinates and hence the enforcement of the continuity of said slopes between the elements. This fits to the findings of Matikainen et al.<sup>12</sup> where the element 3453 was also put to the test. The absence of noticeable shear locking in the results of the elements 3833 and 3933 shows that the usage of approximation orders of at least two in all directions without the employment of in-plane slopes as nodal coordinates seems to be a good practice to yield ANCF plate elements that suffer neither from shear nor from Poisson locking.

#### Large-displacement cantilever

All previous experiments have dealt with load cases that lead to small displacements. For this reason, the intention of the following experiment is to clarify whether the elements 3933, 3833, and 3453 still deliver reasonable results in the case of large deformations. To this end, a cantilevered plate of the length  $L = 0.5$  m, the width  $W = 0.15$  m, and the thickness  $H = 0.001$  m is considered. The same plate was examined in Dufva and Shabana.<sup>15</sup> Young's modulus is set to  $E = 2.07 \times 10^{11}$  N/m<sup>2</sup> with Poisson's ratio being  $\nu = 0.3$ . The total applied force is  $F_z = 30$  N. As illustrated in Figure 5, this force is split equally on the two free corners of the plate.

For the ANCF elements, the mesh was set up in a way that always one element was used in the  $y$  direction

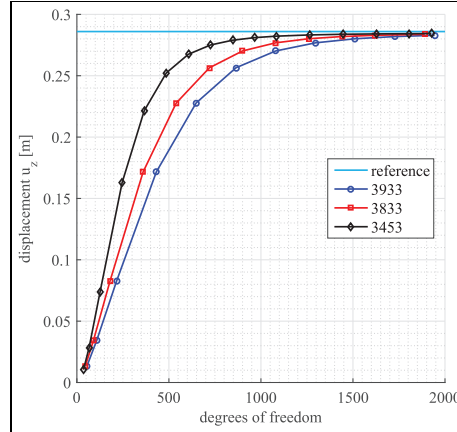


**Figure 6.** Results of the large-displacement cantilever test for various elements.

while the number of elements in the  $x$  direction was increased step by step. The displayed reference result was obtained with the ANSYS solid element SOLID95 and a mesh consisting of 334 elements in the  $x$  direction, 100 elements in the  $y$  direction, and 1 element in the  $z$  direction.

The results of the numerical calculations for different numbers of degrees of freedom are depicted in Figure 6. For all elements, the given displacement value is the arithmetic mean of the vertical displacements of all nodes in the end cross-section.

The results show that all of the high-order elements deliver reasonable results. None of the elements shows any sign of noteworthy convergence problems.

#### Princeton beam experiment

The previous examples have dealt with either small-displacement or simple one-dimensional bending problems. Since the proposed elements are based on full three-dimensional elasticity, they should in theory be usable in a wide range of problems. Hence, in this section, the plate elements are put to the test in the so-called Princeton beam experiment which is a demanding example involving bidirectional bending. First conceived by researchers from Princeton University,<sup>16</sup> this experiment has previously been used to evaluate different beam formulations, including ANCF beam elements.<sup>17</sup>

The cantilevered beam is of the length  $L = 0.508$  m and has a rectangular cross-section of the width  $W = 12.377 \times 10^{-3}$  m and the height  $H = 3.2024 \times 10^{-3}$  m. Young's modulus and Poisson's ratio amount

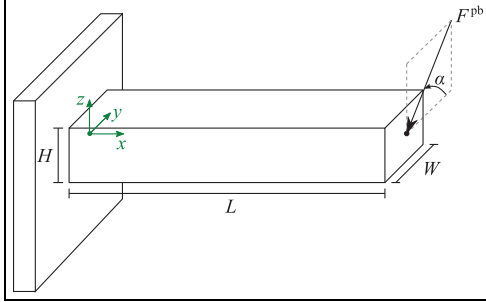


**Figure 7.** Illustration of the setup for the Princeton beam experiment for a tip load of  $F^{pb}$ .

to  $E = 71.7 \times 10^9 \text{ N/m}^2$  and  $\nu = 0.31$ , respectively. The beam is subjected to a concentrated tip load acting on the center of the end cross-section. The force vector is parallel to the  $y$ - $z$ -plane. Its direction, as defined by the angle  $\alpha$  that is included between the force vector and the direction of the  $y$ -axis, is varied in  $15^\circ$  steps from  $0^\circ$  to  $90^\circ$ . The experiment is performed for three different absolute values of the force, namely,  $F_1^{pb} = 4.448 \text{ N}$ ,  $F_2^{pb} = 8.896 \text{ N}$ , and  $F_3^{pb} = 13.345 \text{ N}$ . The setup is illustrated in Figure 7.

For all ANCF elements involved, two elements were used in the  $y$  direction so that for all element types, a node exists that is precisely in the middle of the end cross-section. The recorded displacements are those of that middle node. For the elements 3933, 3833, and 3453, respectively, 20, 25, and 40 elements were used in the  $x$  direction. As a result, for all three elements, the system has approximately 1800 degrees of freedom. The results for the different load cases are depicted in Figures 8 and 9. For the reference results, 64 elements of the ANSYS beam element BEAM188 and a mesh of  $160 \times 8 \times 2$  elements of the ANSYS solid element SOLID95 were used.

Both the results for the chordwise and flapwise displacements show that all of the elements that have passed the previous tests also deliver reasonable results in all load cases of the Princeton beam experiment. This is of particular significance since the Princeton beam experiment is a rather elaborate test case involving nonlinear effects based on the coupling of axial and transverse normal strains. This becomes manifest in the fact that as the angle  $\alpha$  increases from  $0^\circ$  to  $30^\circ$ , the absolute value of the displacement in the  $y$  direction also increases while the force in that direction decreases. However, all considered elements that involve approximation orders of at least two in each direction are able to reproduce this effect. Only upon closer inspection of the results, slight differences between the elements become apparent.

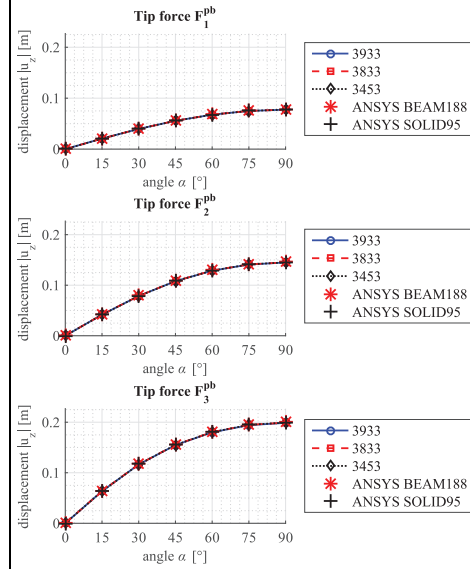


**Figure 8.** Results for the chordwise displacements in the Princeton beam experiment.

In Figure 10, the  $y$  displacements are plotted over different numbers of degrees of freedom. The results have been obtained for the load case with an angle of  $\alpha = 30^\circ$  and the largest force of magnitude  $F_3^{pb}$ , because for these parameters, the nonlinear contributions are most significant and the differences between the elements are most apparent.

As the results show, the elements 3933 and 3833 actually seem to be able to deliver results that are in better concordance with those obtained with the ANSYS solid element SOLID95. The displacement for element 3453, on the other hand, seems to converge to an absolute value that is slightly smaller.

### Dynamic test

The example case selected for the dynamic test is the moderately thick free-flying plate problem presented in Figure 11, originally developed by Matikainen et al.<sup>12</sup> The example was solved using the higher-order ANCF plate elements 3833 and 3933, which have been chosen due to their good performance in the previously presented static examples. The material parameters used in the test are as follows: Young's modulus is  $E = 10^6 \text{ N/m}^2$ , Poisson's ratio amounts to  $\nu = 0.3$ , the density is  $\rho = 1500 \text{ kg/m}^3$ , and shear modulus and correction factor are set to  $G = E/(2(1 + \nu))$  and  $k_s = 5/6$ , respectively. The studied plate is of the length  $L = 1 \text{ m}$ , width  $W = 0.5 \text{ m}$ , and thickness  $H = 0.1 \text{ m}$ .

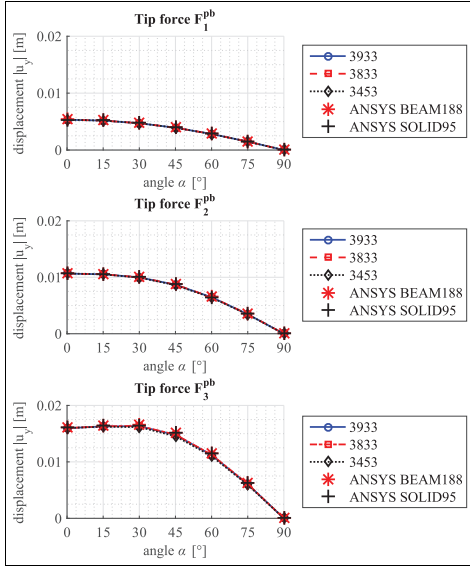


**Figure 9.** Results for the flapwise displacements in the Princeton beam experiment.

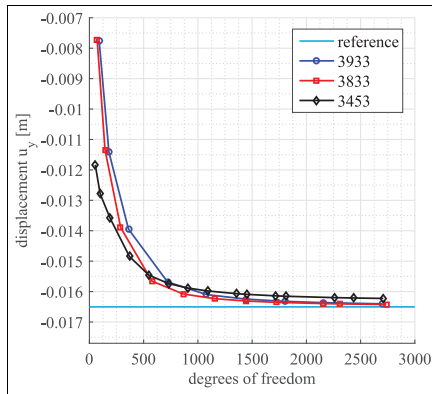


**Figure 10.** Results for the flapwise displacement of the Princeton beam experiment with an angle of  $\alpha = 30^\circ$  and a force of absolute value  $F_3^{pb}$ . The displayed reference result has been obtained with the ANSYS solid element SOLID95 and a mesh of  $160 \times 8 \times 2$  elements.

The force components  $F_x$  and  $F_y$  only affect the node at point  $a$ , while the moment  $M_z$  is distributed evenly among the nodes on the line  $ab$ . As given by

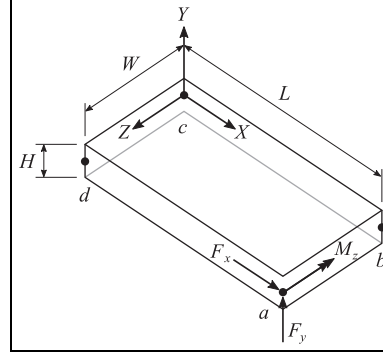


**Figure 11.** Free flying flexible plate.

$$F_x(t) = \begin{cases} 0 & \text{if } 0 \leq t \leq 1.5 \\ 13.5 & \text{if } 1.5 < t \leq 2.5 \end{cases} \text{ (N)} \quad (10)$$

$$F_y(t) = \begin{cases} 0 & \text{if } 0 \leq t \leq 1.5 \\ 18(t - 1.5) & \text{if } 1.5 < t \leq 2.5 \end{cases} \text{ (N)} \quad (11)$$

$$M_z(t) = \begin{cases} -47.5t & \text{if } 0 \leq t \leq 1.5 \\ 0 & \text{if } 1.5 < t \leq 2.5 \end{cases} \text{ (Nm)} \quad (12)$$

the loading of the plate varies as a function of time. The total duration of the simulation is 2.5 s. The results are computed using MATLAB's integrated solver ode15s, which is a variable order integrator for stiff problems, with an output step length of  $10^{-3}$  s. The integration of the elastic forces of each element is done via Gaussian quadratures of order 5. The absolute and relative error tolerances for the solution of the equations of motion are both set to  $5 \times 10^{-4}$ .

The reference results are calculated using a  $256 \times 128$  mesh of SHELL181 elements in ANSYS Mechanical APDL version 17.2. Geometrical nonlinearities are taken into account in the model. The Newmark algorithm is employed in the solution process, with the integration parameters  $\delta = 1/2$  and  $\alpha = 1/4$ . The time steps are of variable length with a starting and maximum step length of  $10^{-2}$  s and a minimum step length of  $10^{-4}$  s. The full Newton–Raphson method is employed in the solution, with convergence criteria settings left at the ANSYS default values, that is, employing the Euclidean norm with tolerance  $10^{-3}$  for force and moment.

The absolute error of the displacement of point  $a$  at time  $t = 0.75$  s for various mesh sizes is presented in Figure 12. The error norms at the later time  $t = 2.5$  s are depicted in Figure 13, while the computational effort required for the computations is compared in Table 5. It should be noted that the computation time values presented in the table are only suggestive, since

**Table 5.** Comparison of the computational effort for the simulation over the time interval  $t \in [0, 2.5]$  (s).

Mesh $x \times y$	Element 3833			Element 3933		
	DOF	Eval.	Time	DOF	Eval.	Time
$2 \times 1$	117	33,870	1.00	135	36,229	1.17
$4 \times 2$	333	41,665	4.98	405	38,591	5.97
$6 \times 3$	657	51,576	19.6	819	52,371	27.9
$8 \times 4$	1089	60,397	57.9	1377	56,681	72.7

DOF: degree of freedom.

"Eval." denotes the number of function evaluations of the equations of motion and "Time" denotes total computation time, scaled with respect to the smallest value.

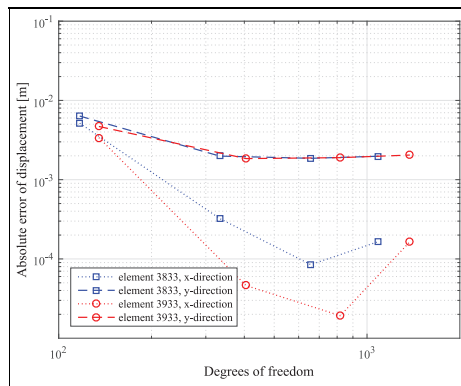


**Figure 12.** Absolute error of the displacement of point  $a$  at  $t = 0.75$  s. The reference results were computed using a  $256 \times 128$  mesh of SHELL181 elements in ANSYS.

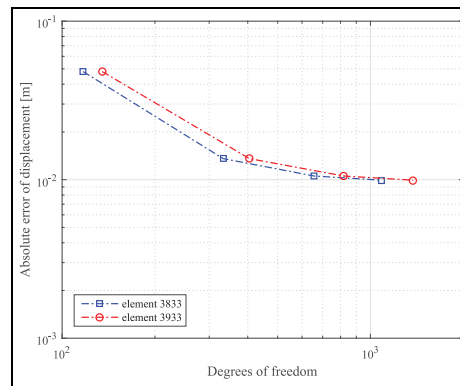


**Figure 13.** Norm of the displacement error of point  $a$  at  $t = 2.5$  s. The reference results were computed using a  $256 \times 128$  mesh of SHELL181 elements in ANSYS.

it could not be ensured that the computation was not hindered by other processes on the machine.

While Figure 12 shows a certain degree of difference between the ANSYS model and the higher-order plate element models, particularly in the  $y$ -directional displacement, it can be concluded from the simulation that generally the higher-order plate models behave very similarly to the ANSYS model. In particular, the plate's rotation is reproduced in the proper way without incorrect strains. Predictably, Table 5 shows that the more complex element 3933 is more computationally demanding, while, according to Figures 12 and 13, element 3833 converges to roughly the same error value with fewer degrees of freedom.

## Conclusion

This study introduces high-order three-dimensional plate elements based on the ANCF for large deformation multibody applications. The introduced elements employ eight or nine nodes.

Contrary to quadrilateral ANCF plate elements considered in previous studies, the two proposed eight-

and nine-node high-order plate elements deliver reasonable results in all considered load cases while exhibiting satisfactory convergence rates. Specifically, both Poisson and shear locking are resolved through the setup of the two elements. In this study, Poisson locking disappears for all elements that have at least an approximation order of two in all directions. In addition, the absence of in-plane slope vectors in the nodal coordinates of the two elements seems to lead to elements that do not suffer from severely deteriorated convergence rates in case of very thin plates.

The considered load cases include two small-displacement tests with one being a cantilevered plate and the other one being a simply supported plate under a uniform body load. For the latter one, an examination of the convergence rates for different thicknesses revealed the advantages of the considered high-order eight- and nine-node elements when compared to the four-node fully parametrized high-order ANCF plate element that has been introduced in previous studies.<sup>12</sup>

Furthermore, two large-displacement load cases, namely one large-displacement cantilevered plate in

one-dimensional bending and the so-called Princeton beam experiment involving bidirectional bending, have shown that the proposed elements also behave favorably in more elaborate situations. Finally, the two proposed eight- and nine-node elements that behaved well in the static tests have been applied in an exemplary dynamic benchmark test, showing that they are also functional in simulations over the time domain.

#### Declaration of conflicting interests

The author(s) declared no potential conflicts of interest with respect to the research, authorship, and/or publication of this article.

#### Funding

The author(s) disclosed receipt of the following financial support for the research, authorship, and/or publication of this article: The authors would like to thank the Academy of Finland (Application No. 259543 for the funding of Postdoctoral Researchers and Application No. 285064) for supporting Marko K. Matikainen.

#### References

- Shabana AA. Definition of the slopes and the finite element absolute nodal coordinate formulation. *Multibody Syst Dyn* 1997; 1: 339–348.
- Shabana AA. Definition of ANCF finite elements. *J Comput Nonlin Dyn* 2015; 5: 054506-1–054506-5.
- Mikkola AM and Shabana AA. A non-incremental finite element procedure for the analysis of large deformations of plates and shells in mechanical system applications. *Multibody Syst Dyn* 2003; 9: 283–309.
- Kuhl D and Ramm E. Time integration in the context of energy control and locking free finite elements. *Arch Comput Method E* 2000; 7: 299–332.
- Gerstmayr J and Shabana AA. Efficient integration of the elastic forces and thin three-dimensional beam elements in the absolute nodal coordinate formulation. In: *Proceedings of the ECCOMAS thematic conference on multibody dynamics* (eds Goicolea, Cuadrado and Garcia Orden), Madrid, 21–24 June 2005.
- Matikainen MK, Dmitrochenko O and Mikkola A. Beam elements with trapezoidal cross section deformation modes based on the absolute nodal coordinate formulation. In: *Proceedings of the international conference of numerical analysis and applied mathematics*, Rhodes, 19–25 September 2010, <http://dx.doi.org/10.1063/1.3497930>
- Matikainen MK, Dmitrochenko O and Mikkola A. Higher order beam elements based on the absolute nodal coordinate formulation. In: *Proceedings of the ECCOMAS thematic conference on multibody dynamics* (eds JC Samin and P Fiset), Brussels, 4–7 July 2011.
- Ebel H, Matikainen MK, Hurskainen VV, et al. Higher-order beam elements based on the absolute nodal coordinate formulation for three-dimensional elasticity. *Nonlinear Dynam* 2017; 88: 1075–1091.
- Shen Z, Li P, Liu C, et al. A finite element beam model including cross-section distortion in the absolute nodal coordinate formulation. *Nonlinear Dynam* 2014; 77: 1019–1033.
- Olshevskiy A, Dmitrochenko O, Lee S, et al. A triangular plate element 2343 using second-order absolute-nodal-coordinate slopes: numerical computation of shape functions. *Nonlinear Dynam* 2013; 74: 769–781.
- Olshevskiy A, Dmitrochenko O, Dai MD, et al. The simplest 3-, 6- and 8-noded fully-parameterized ANCF plate elements using only transverse slopes. *Multibody Syst Dyn* 2015; 34: 23–51.
- Matikainen MK, Valkeapää AI, Mikkola AM, et al. A study of moderately thick quadrilateral plate elements based on the absolute nodal coordinate formulation. *Multibody Syst Dyn* 2014; 31: 309–338.
- Dmitrochenko O and Mikkola A. Digital nomenclature code for topology and kinematics of finite elements based on the absolute nodal co-ordinate formulation. *P I Mech Eng K: J Mul* 2011; 225: 34–51.
- Bletzinger KU, Bischoff M and Ramm E. A unified approach for shear-locking-free triangular and rectangular shell finite elements. *Comput Struct* 2000; 75: 321–334.
- Dufva K and Shabana AA. Analysis of thin plate structures using the absolute nodal coordinate formulation. *P I Mech Eng K: J Mul* 2005; 219: 345–355.
- Dowell E and Traybar JJ. *An experimental study of the nonlinear stiffness of a rotor blade undergoing flap, lag and twist deformations*. Technical report, AMS Report no. 1194, 1975, <https://ntrs.nasa.gov/search.jsp?R=19770003067>
- Bauchau OA, Han S, Mikkola A, et al. Experimental validation of flexible multi-body dynamics beam formulations. *Multibody Syst Dyn* 2015; 34: 373–389.

## Publication IV

Wang, J., Hurskainen, V.-V., Matikainen, M.K., Sapanen, J., Mikkola, A.  
**On the dynamic analysis of rotating shafts using nonlinear  
super-element and absolute nodal coordinate formulations**

Reprinted from  
*Advances in Mechanical Engineering*  
Vol. 9(11), November 2017  
© 2017, the authors



# On the dynamic analysis of rotating shafts using nonlinear superelement and absolute nodal coordinate formulations

Advances in Mechanical Engineering  
2017, Vol. 9(11) 1–14  
© The Author(s) 2017  
DOI: 10.1177/1687814017732672  
journals.sagepub.com/home/ade  
SAGE

Jia Wang<sup>1</sup>, Vesa-Ville Hurskainen<sup>2</sup>, Marko K Matikainen<sup>2</sup>,  
Jussi Sopanen<sup>2</sup> and Aki Mikkola<sup>2</sup>

## Abstract

In this article, a superelement formulation and a quadratic beam element based on the absolute nodal coordinate formulation are applied to the simulation of high-speed rotating structures. To this end, these formulations are briefly reviewed by highlighting their distinctive features. The performance of the studied formulations is examined using two numerical examples. The first test is a spinning beam example in which the transient response is examined. An unbalanced rotating shaft is studied in the second example, in which both transient and modal analyses are performed. The results produced using both formulations are compared against those produced in the commercial finite element software ANSYS and those available in literature. The article tests in a rotating machine dynamics context two element types which have not been formulated primarily with rotating applications in mind. This is useful in investigating the versatility of these elements.

## Keywords

Rotordynamics, finite element analysis, gyroscopic effects, modal analysis, multibody dynamics

Date received: 27 June 2017; accepted: 29 August 2017

Handling Editor: Yunn-Lin Hwang

## Introduction

The analysis of rotating machinery dynamics is important in the design of many industrial applications, such as vacuum pumps, compressors, turbines and machine tool systems. The traditional approach to rotor dynamics modelling is to adopt one-dimensional (1D) models, where the shafts are modelled as beams and discs and impellers are modelled as rigid bodies.<sup>1</sup> Correspondingly, the deformation of the shaft cross section is not considered in the classical 1D approach. In some applications, these assumptions may not be acceptable since the compliance of the discs and blades may affect the dynamics of the rotor. Also, the deformation of the shaft cross section may be significant, for example, in the case of tubular shafts commonly used in turbomachinery. The

inclusion of shaft cross-sectional deformation and the flexibility of the discs and blades enables the description of centrifugal stiffening phenomena, where the internal tensional stresses lead to increased stiffness of the rotor.<sup>2</sup> In addition, the thermomechanical effects might lead to residual internal stresses in the rotors that are often constructed of parts with different materials. To address these issues, several authors have proposed and utilised

<sup>1</sup>Harbin Institute of Technology, Harbin, China

<sup>2</sup>Lappeenranta University of Technology, Lappeenranta, Finland

## Corresponding author:

Vesa-Ville Hurskainen, Lappeenranta University of Technology,  
Skinnarilankatu 34, 53851 Lappeenranta, Finland.  
Email: vesa-ville.hurskainen@lut.fi



Creative Commons CC-BY: This article is distributed under the terms of the Creative Commons Attribution 4.0 License (<http://www.creativecommons.org/licenses/by/4.0/>) which permits any use, reproduction and distribution of the work without further permission provided the original work is attributed as specified on the SAGE and Open Access pages (<https://us.sagepub.com/en-us/nam/open-access-at-sage>).

two-dimensional (2D) axisymmetric harmonic elements<sup>3</sup> or three-dimensional (3D) solid elements.<sup>4,5</sup> The 2D approach can describe the gyroscopic effect and the stress stiffening effect caused by the deformation of the shaft cross section or discs. The main assumption in the 2D approach is that the rotor is axisymmetric, which makes it unsuitable for analysing cases where either the rotor or the loading is asymmetric, which can occur, for example, due to blade loss or rubbing between the rotor and stator. On the other hand, the 3D solid element approach does not suffer the drawbacks encountered in 1D and 2D approaches. Nevertheless, the increase in computational effort makes it unpractical in some cases.

As an alternative, the transient analysis of high-speed rotors can be accomplished using a nonlinear finite element (FE) approach targeted for multibody applications. For example, nonlinear beam FEs<sup>6–9</sup> have proven to produce accurate results. However, nonlinear beam element models may also be unable to accurately describe systems with complex geometries.

To summarise, traditional 1D approaches to rotor dynamics might not be capable of reliable dynamic prediction in transient cases or situations where a nonlinear strain–displacement relation is needed. More accurate 2D or 3D formulations suffer from either the drawbacks resulting from the assumption of axisymmetry or high computational costs. It is for these reasons that many authors have utilised model reduction techniques.<sup>10,11</sup> One of these is the substructure method, which makes it possible to reduce an FE model by projecting it onto component modes. Originally, the substructure method (or modal reduction technique) was used to analyse linear dynamics problems such as modal analysis and time integration,<sup>12,13</sup> while later researchers<sup>14,15</sup> came to use the technique in the context of multibody dynamics.

The selection of the component modes is critical in the modal reduction procedure. An often used approach is based on the use of static constraint modes obtained by imposing displacements on the interface nodes, complemented with vibration modes with the interface clamped.<sup>13,16</sup> This is called the Craig–Bampton approach. Another popular method, called MacNeal’s method, uses the free-free vibration modes of the substructure complemented with attachment modes obtained via static loading on the interface. Different variations or combinations of these reduction methods have also been proposed. Cardona<sup>17</sup> and Wu and Tiso<sup>18</sup> combined Craig–Bampton modes with the floating frame concept to reduce the coordinates of flexible structure models. Géradin and Rixen<sup>19</sup> used MacNeal modes to simulate structures with unilateral contacts, such as leaf springs.

Assuming that elastic deformation remains small when the flexible body undergoes large reference motions, the global position of a particle can be defined as a superposition of the reference motion of a local

frame and the elastic deformation with regard to that local frame. This approach is called the floating frame of reference formulation (FFRF) and is often used in practical applications when flexibility needs to be taken into account in multibody dynamics. By combining FFRF and modal reduction, Cardona and colleagues<sup>16,17,20,21</sup> and Bauchau and Rodriguez<sup>22</sup> introduced the so-called superelements. In the earlier publications,<sup>20,21</sup> the reference frame was attached to one node. Later, the reference frame was chosen based on the position of the interface nodes.<sup>17</sup> The latter approach was proven to be more accurate. Although the efficiency and accuracy of the FFRF-based superelement have been reported in many publications, the element is cumbersome to use as the equations of motion include state-dependent non-constant inertia terms, such as the mass matrix and the quadratic velocity vector. This is due to the nonlinear relationship between global and local frame coordinates. To reduce this nonlinearity, a generalised modal reduction method based on the absolute coordinate formulation (ACF) with a constant mass matrix was proposed in Pechstein et al.<sup>23</sup> and Naets and Desmet<sup>24</sup> There, FFRF-based and ACF-based superelements were compared, and it was concluded that the ACF-based element is more efficient and accurate. It was even found that in some cases, the results given by the FFRF-based superelement were not dependable.

In general, beam elements can be derived by using the elastic line concept. This allows accurate modelling of slender structures with uniform cross sections. This approach is, however, less suited for modelling complex-shaped flexible components, for example, rotors with discs or beams with varying cross-sectional properties. As an alternative to the conventional elastic line concept, Jonker and Meijaard<sup>25</sup> described a set of deformation mode formulations for a 3D shear deformable beam element. The reduced linear model is obtained by applying the Craig–Bampton method to the FE model of the complex-shaped component. By relating the constraint modes to the deformation mode formulation, the potential energy of the nonlinear superelement can be determined. The kinetic energy can, in turn, be determined by expressing the absolute velocity vectors in a co-rotational frame. Thus, based on the combination of the model reduction technique and Jonker’s description, an efficient modelling approach allowing arbitrary reference body motions and deformations of complex-shaped flexible components can be obtained.<sup>26</sup> In this approach, it is no longer necessary to use additional degrees of freedom (DOFs), for example, for defining the floating reference frame in FFRF or the generalised modal parameters in ACF. This feature is claimed to lead to improved numerical efficiency. The superelement has been validated with numerical examples, but the performance of

this approach in applications of rotor dynamics where the gyroscopic effect plays a significant role is yet to be properly investigated.

Rotor systems can also be modelled using the absolute nodal coordinate formulation (ANCF). In the ANCF, the nodal coordinates of spatial FEs are defined using global positions and components of the nodal deformation gradients.<sup>27</sup> Because of the linear relationship between nodal and position coordinates, the element mass matrix is constant and can be defined as in the linear FE approach. Contrary to the simple expression of inertial forces, the expression of element elastic forces is highly nonlinear and computationally demanding. However, due to the nonlinear description of strain, the nonlinear geometric stiffening terms encountered in high-speed rotors are automatically included in this formulation.

The objective of this article is to study the performance of the superelement formulation and the ANCF in the analysis of rotating structures. The article will make observations regarding the usability and accuracy of these approaches. In the next section, the Craig–Bampton approach is used to obtain the reduced matrices of the linear superelement. The nonlinear superelement is introduced in the third section by combining the constraint modes with the deformation mode formulation. The formulation of the ANCF-based beam element is reviewed in the fourth section, and in the fifth section, the behaviour of both formulations is studied in numerical tests. The first example is a spinning beam experiment, in which the transient response of the mechanical system is computed using the superelement formulation. The second example case consists of a rotor with an unbalanced rigid disc, in which the transient response and the Campbell diagram of the system are computed using both formulations.

### Component modes and model reduction

This section briefly reviews the concept of modal reduction. In the FE method, the equations of motion for a rotor system can be written in matrix form as

$$\mathbf{M}\ddot{\mathbf{q}} + (\Omega\mathbf{G} + \mathbf{C})\dot{\mathbf{q}} + \mathbf{K}\mathbf{q} = \mathbf{f}_{\text{ext}} \quad (1)$$

where  $\mathbf{M}$  is the mass matrix,  $\mathbf{K}$  is the stiffness matrix,  $\mathbf{G}$  is the gyroscopic matrix,  $\mathbf{C}$  is the damping matrix,  $\mathbf{q}$  is the generalised coordinate vector,  $\mathbf{f}_{\text{ext}}$  is the external force vector and  $\Omega$  is the rotational speed. According to the component mode synthesis approach, a set of component modes can be selected and used for projecting the generalised coordinate vector  $\mathbf{q}$  into a reduced set of coordinates, as follows

$$\mathbf{q} = \Phi\boldsymbol{\xi} \quad (2)$$

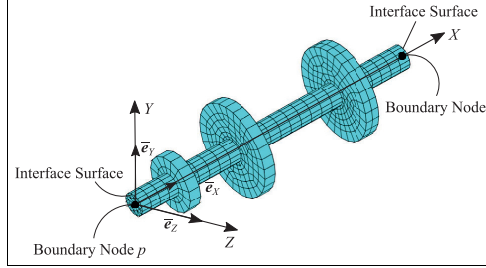


**Figure 1.** Finite element model of a complex-shaped component.

where  $\Phi$  is a matrix representation of the selected modes. In modal reduction, the number of selected modes should be less than the original number of DOFs. In equation (2),  $\boldsymbol{\xi}$  is the reduced set of coordinates, often called modal coordinates, with respect to the selected modes.

The beam-like rotor structure shown in Figure 1 is connected via two interfaces, one at each side of the component. In the case of a slender structure, such as the rotor system, the deformations of the interface can be considered to be negligible. Hence, the DOFs of the nodes on the interface surfaces can be bound with boundary nodes  $p$  and  $q$ . The deformation of the structure can be described with respect to a local reference coordinate frame attached at boundary  $p$  with unit basis  $[\bar{\mathbf{e}}_x \ \bar{\mathbf{e}}_y \ \bar{\mathbf{e}}_z]$ . Each boundary node has three translational ( $\bar{\mathbf{u}}$ ) and three rotational ( $\bar{\boldsymbol{\phi}}$ ) DOFs. Using the Craig–Bampton method, the FE model can be reduced with 12 static constraints plus a set of fixed-interface normal modes whose number depends on the problem. Accordingly, equation (2) can be written as

$$\mathbf{q} = \Phi\boldsymbol{\xi} = [\mathbf{V} \ \mathbf{W}] \begin{Bmatrix} \boldsymbol{\mu} \\ \boldsymbol{\eta} \end{Bmatrix} \quad (3)$$

where  $\mathbf{V}$  is a matrix containing the 12 constraint modes which are illustrated in Figure 2,  $\mathbf{W}$  is a matrix containing the fixed-interface normal modes,  $\boldsymbol{\mu} = \{\bar{\mathbf{u}}^{pT} \bar{\boldsymbol{\phi}}^{pT} \bar{\mathbf{u}}^{qT} \bar{\boldsymbol{\phi}}^{qT}\}^T$  is the reduced boundary coordinate vector related to  $\mathbf{V}$  and  $\boldsymbol{\eta}$  is the vector of reduced internal coordinates related to  $\mathbf{W}$ . The reduced system matrices based on the proposed modes can be obtained as follows

$$\begin{cases} \bar{\mathbf{M}} = \begin{bmatrix} \mathbf{V}^T \\ \mathbf{W}^T \end{bmatrix} \mathbf{M} [\mathbf{V} \ \mathbf{W}] \\ \bar{\mathbf{K}} = \begin{bmatrix} \mathbf{V}^T \\ \mathbf{W}^T \end{bmatrix} \mathbf{K} [\mathbf{V} \ \mathbf{W}] \\ \bar{\mathbf{G}} = \begin{bmatrix} \mathbf{V}^T \\ \mathbf{W}^T \end{bmatrix} \mathbf{G} [\mathbf{V} \ \mathbf{W}] \end{cases} \quad (4)$$

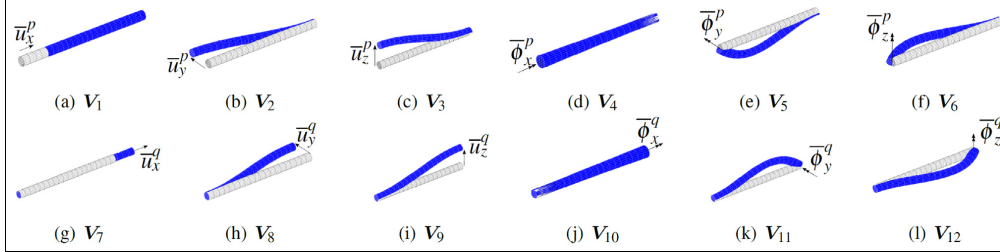


**Figure 2.** The static constraint modes of an FE model

The reduced matrices can be used as a linear superelement. It is worth noting that this approach is only suitable for use in a small-displacement and small-deformation problem. The pure elastic deformation of the component can be described by a six-dimensional subspace of  $V$ . As an example, a possible choice of constraint modes could consist of the elongation mode  $V_7$ , the torsion mode  $V_{10}$  and the four bending modes  $V_5$ ,  $V_{11}$  and  $V_6$ ,  $V_{12}$ . In this example case, equation (3) can be rewritten as

$$q^e = [V^e \quad W] \begin{Bmatrix} \mu^e \\ \eta \end{Bmatrix} \quad (5)$$

where the elastic modes  $V^e$  are as follows

$$V^e = [V_7 \quad V_{10} \quad V_5 \quad V_{11} \quad V_6 \quad V_{12}] \quad (6)$$

The reduced stiffness matrix can be obtained as follows

$$\bar{S} = \begin{bmatrix} V^{eT} \\ W^T \end{bmatrix} K [V^e \quad W] \quad (7)$$

### Non-linear superelement

As mentioned above, the linear superelement is suitable for small-deformation problems only. When the component undergoes large rotation and translation with large deformation, the superelement needs to be described with respect to the global coordinate frame.

The deformed configuration of the superelement is shown in Figure 3. The positions of its boundary nodes can be described using two vectors,  $r^p$  and  $r^q$ , and the orientation of the interface surfaces is defined by two sets of orthogonal base vectors:  $[e_x^p, e_y^p, e_z^p]$  and  $[e_x^q, e_y^q, e_z^q]$ . The two sets of base vectors relate to the undeformed configuration via rotation matrices  $R^p$  and  $R^q$  and the undeformed configuration, in turn, to the global coordinates via rotation matrix  $R^e$ . Therefore, the following definitions can be obtained

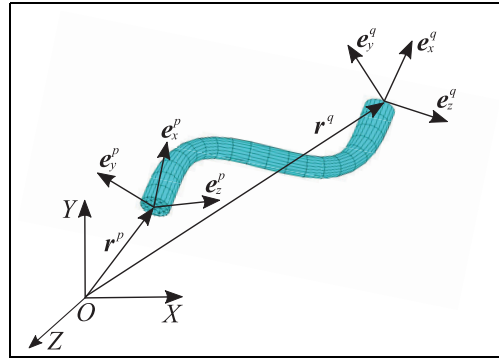


**Figure 3.** Configuration of the superelement undergoing large displacements and deformations.

$$\begin{bmatrix} e_x^p & e_y^p & e_z^p \\ e_x^q & e_y^q & e_z^q \end{bmatrix} = \begin{bmatrix} R^p & R^q \\ R^e & R^e \end{bmatrix} \begin{bmatrix} e_x & e_y & e_z \\ e_x & e_y & e_z \end{bmatrix} \quad (8)$$

where  $e_x$ ,  $e_y$  and  $e_z$  are the unit vectors in the initial reference frame. The rotation matrix can be defined in several ways, such as Euler parameters, Euler angles, Rodrigues parameters or the Cartesian rotation vector.<sup>16</sup> In Boer et al.'s publication,<sup>26</sup> Euler parameters are used to avoid the singularity problems associated with Euler angles. Since Euler parameters are coupled via the constraint  $\lambda^T \lambda = 1$ , efforts have to be made to take the constraint into account in the equations of motion. In this article, the rotation matrix  $R = R_z R_y R_x$  is defined as the product of three successive rotations parametrised by the modified Euler angles  $\{\phi_x, \phi_y, \phi_z\}$ . Using these rotational parameters, the nodal coordinates  $x$  of the non-linear superelement can be written as

$$x = \{x^p \quad y^p \quad z^p \quad \phi_x^p \quad \phi_y^p \quad \phi_z^p \quad x^q \quad y^q \quad z^q \quad \phi_x^q \quad \phi_y^q \quad \phi_z^q\}^T \quad (9)$$

The velocity vector can be obtained by differentiating equation (9) with respect to time, as follows

$$\mathbf{v} = \{ \mathbf{v}^p \mathbf{\omega}^p \mathbf{v}^q \mathbf{\omega}^q \}^T \quad (10)$$

where  $\mathbf{v}^p$  and  $\mathbf{v}^q$  are the absolute nodal translational velocities and  $\mathbf{\omega}^p$  and  $\mathbf{\omega}^q$  are absolute nodal rotational velocities.

### Deformation modes and potential energy

According to Jonker and Meijaard,<sup>25</sup> elastic deformation can be described by a set of deformation coordinates expressed as functions of the nodal coordinates  $\mathbf{x}$ , as follows

$$\boldsymbol{\varepsilon} = \mathcal{D}(\mathbf{x}) \quad (11)$$

and

$$\begin{aligned} \varepsilon_1 &= l - l_0 \\ \varepsilon_2 &= l_0(\mathbf{e}_z^p \mathbf{e}_y^q - \mathbf{e}_y^p \mathbf{e}_z^q)/2 \\ \varepsilon_3 &= -l_0 \mathbf{e}_1 \mathbf{e}_z^p \\ \varepsilon_4 &= l_0 \mathbf{e}_1 \mathbf{e}_z^q \\ \varepsilon_5 &= l_0 \mathbf{e}_1 \mathbf{e}_y^p \\ \varepsilon_6 &= -l_0 \mathbf{e}_1 \mathbf{e}_y^q \end{aligned} \quad (12)$$

where  $l_0$  is the reference length of the superelement,  $\mathbf{l} = \mathbf{r}^q - \mathbf{r}^p$  is a vector from the boundary node  $p$  to  $q$  and  $l = \|\mathbf{l}\|$  is the distance between the boundary nodes. Vector  $\mathbf{e}_1 = (\mathbf{r}^q - \mathbf{r}^p)/(\|\mathbf{r}^q - \mathbf{r}^p\|)$  is unit in length and pointing from  $p$  towards  $q$ . The deformation coordinate  $\varepsilon_1$  describes axial deformation,  $\varepsilon_2$  describes torsion and  $\varepsilon_3$ ,  $\varepsilon_4$ ,  $\varepsilon_5$  and  $\varepsilon_6$  describe bending deformations. These definitions are illustrated in Figure 4.

To determine the elastic forces for the superelement, an energy approach can be used. To this end, the relationship between  $\boldsymbol{\varepsilon}$  and  $\boldsymbol{\mu}^e$  needs to be defined by using the definition of the deformation coordinates (equation (11)) and the elastic deformation of the linear superelement (equation (6)), as follows

$$\boldsymbol{\mu}^e = \mathbf{A} \boldsymbol{\varepsilon} \quad (13)$$

where  $\mathbf{A} = \text{diag}(1, (1/l_0), -(1/l_0), (1/l_0), -(1/l_0), (1/l_0))$ . Here, matrix  $\mathbf{A}$  describes the relationship between the deformation coordinates defined in equation (12) (Figure 4) and their corresponding constraint modes defined in equation (7) (Figure 2). Using equations (7) and (13), the potential energy of the nonlinear superelement can be written as

$$\begin{aligned} P &= \frac{1}{2} \{ \boldsymbol{\mu}^e \mathbf{\eta}^T \} \bar{\mathcal{S}} \left\{ \begin{matrix} \boldsymbol{\mu}^e \\ \boldsymbol{\eta} \end{matrix} \right\} \\ &= \frac{1}{2} \{ \boldsymbol{\varepsilon}^T \mathbf{\eta}^T \} \left[ \begin{matrix} \mathbf{A} \\ \mathbf{I} \end{matrix} \right]^T \bar{\mathcal{S}} \left[ \begin{matrix} \mathbf{A} \\ \mathbf{I} \end{matrix} \right] \left\{ \begin{matrix} \boldsymbol{\varepsilon} \\ \boldsymbol{\eta} \end{matrix} \right\} \\ &= \frac{1}{2} \{ \boldsymbol{\varepsilon}^T \mathbf{\eta}^T \} \tilde{\mathcal{S}} \left\{ \begin{matrix} \boldsymbol{\varepsilon} \\ \boldsymbol{\eta} \end{matrix} \right\} \end{aligned} \quad (14)$$

The equivalent stiffness matrix of the nonlinear superelement is

$$\tilde{\mathcal{S}} = \left[ \begin{matrix} \mathbf{A} & \\ & \mathbf{I} \end{matrix} \right]^T \bar{\mathcal{S}} \left[ \begin{matrix} \mathbf{A} \\ \mathbf{I} \end{matrix} \right] \quad (15)$$

### Kinetic energy

Similarly to the potential energy, the kinetic energy of the nonlinear superelement can be obtained by relating the absolute velocity vector  $\mathbf{v}$  to the velocity vector  $\bar{\mathbf{v}}$ , which is defined with respect to the local reference coordinate frame. This requires relating the derivatives of nodal coordinates  $\dot{\mathbf{x}}$  to the derivatives of reduced coordinates  $\dot{\boldsymbol{\mu}}$ . The relationship between  $\mathbf{v}$  and  $\bar{\mathbf{v}}$  can be written as

$$\bar{\mathbf{v}} = \mathbf{B}_i \mathbf{v} \quad (16)$$

where  $\mathbf{B}_i$  is the velocity transformation matrix. Two approaches can be used for expressing the absolute velocity. In the first approach, the translational and rotational velocities of boundaries  $p$  and  $q$  are both

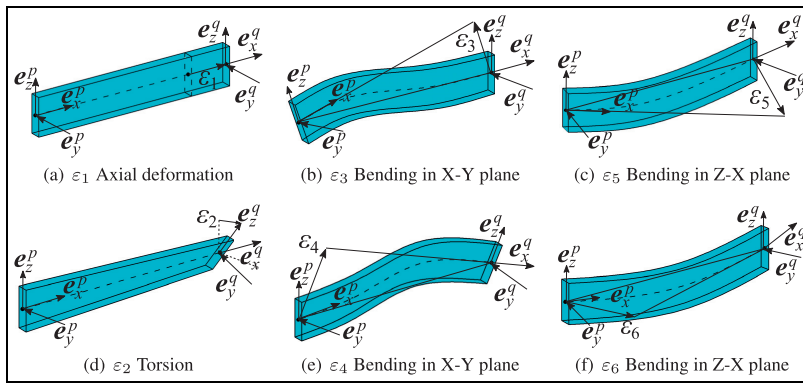


Figure 4. Visualisation of the definition of deformation coordinates.

expressed in a coordinate frame attached to boundary node  $p$ . The transformation matrix in this case is

$$\mathbf{B}_1 = \begin{bmatrix} \mathbf{R}^{eT} \mathbf{R}^{pT} & & & \\ & \mathbf{R}^{eT} \mathbf{R}^{pT} & & \\ & & \mathbf{R}^{eT} \mathbf{R}^{qT} & \\ & & & \mathbf{R}^{eT} \mathbf{R}^{qT} \end{bmatrix} \quad (17)$$

In the second approach, the translational and rotational velocities of boundary  $p$  are expressed in a coordinate frame attached to boundary node  $p$ , while the velocities of boundary  $q$  are expressed in a coordinate frame attached to boundary node  $q$ . The transformation matrix in this scenario is

$$\mathbf{B}_2 = \begin{bmatrix} \mathbf{R}^{eT} \mathbf{R}^{pT} & & & \\ & \mathbf{R}^{eT} \mathbf{R}^{pT} & & \\ & & \mathbf{R}^{eT} \mathbf{R}^{qT} & \\ & & & \mathbf{R}^{eT} \mathbf{R}^{qT} \end{bmatrix} \quad (18)$$

The equivalent kinetic energy of the nonlinear super-element can be rewritten as

$$\begin{aligned} T &= \frac{1}{2} \bar{\mathbf{v}}^T \bar{\mathbf{M}} \bar{\mathbf{v}} \\ &= \frac{1}{2} \{ \dot{\mathbf{x}}^T \quad \dot{\boldsymbol{\eta}}^T \} \begin{bmatrix} \mathbf{B}_i & \mathbf{I} \end{bmatrix}^T \bar{\mathbf{M}} \begin{bmatrix} \mathbf{B}_i & \mathbf{I} \end{bmatrix} \begin{Bmatrix} \dot{\mathbf{x}} \\ \dot{\boldsymbol{\eta}} \end{Bmatrix} \\ &= \frac{1}{2} \{ \dot{\mathbf{x}}^T \quad \dot{\boldsymbol{\eta}}^T \} \tilde{\mathbf{M}} \begin{Bmatrix} \dot{\mathbf{x}} \\ \dot{\boldsymbol{\eta}} \end{Bmatrix} \end{aligned} \quad (19)$$

The mass matrix of the nonlinear super-element can be written as

$$\tilde{\mathbf{M}} = \begin{bmatrix} \mathbf{B}_i & \mathbf{I} \end{bmatrix}^T \bar{\mathbf{M}} \begin{bmatrix} \mathbf{B}_i & \mathbf{I} \end{bmatrix} \quad (20)$$

### Dynamics

The equations of motion for the nonlinear super-element can be written as

$$\tilde{\mathbf{M}} \begin{Bmatrix} \ddot{\mathbf{x}} \\ \ddot{\boldsymbol{\eta}} \end{Bmatrix} + \tilde{\mathbf{G}} \begin{Bmatrix} \dot{\mathbf{x}} \\ \dot{\boldsymbol{\eta}} \end{Bmatrix} = \mathbf{f}_{ext} - \mathbf{f}_{in} \quad (21)$$

where  $\tilde{\mathbf{G}}$  is the velocity-related gyroscopic matrix of the nonlinear super-element and  $\mathbf{f}_{in}$  is the vector of elastic forces. The components can be written as

$$\begin{aligned} \tilde{\mathbf{G}} &= \begin{bmatrix} \dot{\mathbf{B}}_i & \mathbf{0} \end{bmatrix}^T \bar{\mathbf{M}} \begin{bmatrix} \mathbf{B}_i & \mathbf{I} \end{bmatrix} + \begin{bmatrix} \mathbf{B}_i & \mathbf{I} \end{bmatrix}^T \bar{\mathbf{M}} \begin{bmatrix} \dot{\mathbf{B}}_i & \mathbf{0} \end{bmatrix} \\ &\quad + \mathbf{B}_i^T \bar{\mathbf{M}} \begin{bmatrix} \mathbf{B}_i & \mathbf{I} \end{bmatrix} \\ \mathbf{f}_{in} &= \begin{bmatrix} \frac{\partial \varepsilon}{\partial \mathbf{x}} \\ \mathbf{I} \end{bmatrix} \mathbf{S} \boldsymbol{\varepsilon} \end{aligned} \quad (22)$$

where  $\mathbf{B}_i^* = (\partial \bar{\mathbf{v}}) / (\partial (\mathbf{x}, \boldsymbol{\eta}))$ .

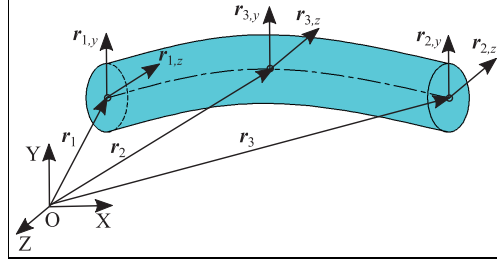


Figure 5. The geometric description of the ANCF beam element.

### Quadratic 3D ANCF beam element

This section briefly reviews the quadratic ANCF beam element used in this article. Subsequently, the gyroscopic matrix, which is necessary for computing the Campbell diagram, is introduced.

The beam element used is a 3D and three-noded element.<sup>28</sup> As shown in Figure 5, the element is defined by one position vector and two slope vectors at each node.

#### Element kinematics

For the quadratic three-node element, the nodal coordinate vector  $\mathbf{q}$  is defined as

$$\begin{aligned} \mathbf{q} &= \{ \mathbf{q}_1^T \quad \mathbf{q}_2^T \quad \mathbf{q}_3^T \}^T \\ \mathbf{q}_i &= \{ r_{i,x}^T \quad r_{i,y}^T \quad r_{i,z}^T \}^T, \quad i = 1, 2, 3 \end{aligned} \quad (23)$$

where  $r_{i,y}$  and  $r_{i,z}$  are the transverse gradient vectors. The element consists of 27 DOFs. Using these nodal coordinates, the position vector of an arbitrary point within the element is described as

$$\mathbf{r}(x, y, z) = \mathbf{S} \mathbf{q} \quad (24)$$

where  $\mathbf{S} = [\mathbf{S}_1 \mathbf{I} \dots \mathbf{S}_9 \mathbf{I}]$  is the shape function matrix, and  $x, y, z$  are the coordinates in the element local coordinate system;  $x \in [-(L/2), (L/2)]$  indicates the lengthwise direction. The element's shape functions  $S_1, \dots, S_9$  can be written as follows

$$\begin{aligned} S_1(x) &= -\frac{2}{L^2} x \left( \frac{L}{2} - x \right) \\ S_2(x, y) &= y S_1, \quad S_3(x, z) = z S_1 \\ S_4(x) &= +\frac{2}{L^2} x \left( \frac{L}{2} + x \right) \\ S_5(x, y) &= y S_4, \quad S_6(x, z) = z S_4 \\ S_7(x) &= -\frac{4}{L^2} \left( x - \frac{L}{2} \right) \left( x + \frac{L}{2} \right) \\ S_8(x, y) &= y S_7, \quad S_9(x, z) = z S_7 \end{aligned} \quad (25)$$

### Element strains: structural mechanics formulation

Using the structural mechanics–based approach, strain energy can be expressed as follows

$$U_{\text{SMF}} = \frac{1}{2} \int_{-L/2}^{L/2} (EA\Gamma_1^2 + GAk_2\Gamma_2^2 + GAk_3\Gamma_3^2 + GJ\kappa_1^2 + EI_2\kappa_2^2 + EI_3\kappa_3^2) dx \quad (26)$$

where  $k_2$  and  $k_3$  are the shear correction factors that are used to obtain the correct shear strain energy.  $\Gamma_1, \dots, \Gamma_3$  and  $\kappa_1, \dots, \kappa_3$  are the generalised strains, which can be defined using a cross-sectional reference frame. The reference frame can, in turn, be defined using the base vectors  $e_1, \dots, e_3$ . The unit vectors are described by Nachbagaueer et al.<sup>28</sup> as follows

$$\begin{aligned} e_1 &= \frac{\bar{e}_1}{|\bar{e}_1|}, & \bar{e}_1 &= r_y \times r_z \\ e_3 &= \frac{\bar{e}_3}{|\bar{e}_3|}, & \bar{e}_3 &= r_z \\ e_2 &= \frac{\bar{e}_2}{|\bar{e}_2|}, & \bar{e}_2 &= \bar{e}_3 \times \bar{e}_1 \end{aligned} \quad (27)$$

The generalised axial strain  $\Gamma_1$  and shear strains  $\Gamma_2$  and  $\Gamma_3$  can now be defined as

$$\begin{aligned} \Gamma_1 &= e_1^T r_x - 1 \\ \Gamma_2 &= e_2^T r_x \\ \Gamma_3 &= e_3^T r_x \end{aligned} \quad (28)$$

where the subscript  $x$  indicates length derivatives. Following this, the vector of twist and curvature  $\mathbf{k}$  can be written as

$$\mathbf{k} = \frac{1}{2} \sum_{i=1}^3 e_i \times e_{i,x} = \frac{1}{2} (e_1 \times e'_{1,x} + e_2 \times e'_{2,x} + e_3 \times e'_{3,x}) \quad (29)$$

The generalised torsion strain  $\kappa_1$  and bending strains  $\kappa_2$  and  $\kappa_3$  are defined as

$$\boldsymbol{\kappa} = \mathbf{A}_e^T \mathbf{k} \quad (30)$$

where  $\mathbf{A}_e = [e_1 \ e_2 \ e_3]$  is an orthogonal rotation matrix describing the local element coordinate system. In addition to equation (26), a second strain energy term can be used to take into account cross-sectional deformation (without the Poisson effect), defined as follows

$$U_{\text{CSD}} = \frac{1}{2} \int_{-L/2}^{L/2} (EA(E_{yy}^2 + E_{zz}^2) + GAE_{yz}^2) dx \quad (31)$$

where the strains  $E_{yy}$ ,  $E_{zz}$  and  $E_{yz}$  are the components of the Green–Lagrange strain tensor, defined as

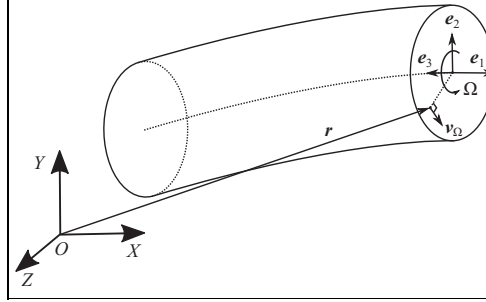


**Figure 6.** The velocity caused by rotation of the ANCF beam element.

$$\begin{aligned} E_{yy} &= \frac{1}{2} (r_y^T r_y - 1) \\ E_{zz} &= \frac{1}{2} (r_z^T r_z - 1) \\ E_{yz} &= \frac{1}{2} r_y^T r_z \end{aligned} \quad (32)$$

### Linear dynamics: gyroscopic matrix

For the purposes of transient analysis, the inertia for the ANCF beam element can be simply calculated from the expression of kinetic energy  $T = (1/2) \int_V |\dot{\mathbf{r}}|^2 dm$ . However, for the linearised eigenvalue solution required in the Campbell diagram computation, a gyroscopic matrix from the system is needed. To this end, small deformations and constant rotational speed  $\Omega$  around the element's longitudinal axis are assumed. The rotation causes a tangential velocity component  $v_\Omega(y, z)$  on each point of the element cross section, which is further illustrated in Figure 6.

Separating the rotational velocity component and using the previously defined orthogonal rotation matrix  $\mathbf{A}_e$ , the velocity of an arbitrary point within the element can be written as

$$\dot{\mathbf{r}}(x, y, z) = \mathbf{v} + \mathbf{v}_\Omega = \mathbf{v} + \Omega \mathbf{A}_e \mathbf{b} \quad (33)$$

where  $\mathbf{v}$  is the velocity of the point without the rotation and vector  $\mathbf{b} = [0 \ -z \ y]^T$  represents the direction of the rotational velocity component in the cross-sectional frame according to the right-hand rule. In this linearised case, the approximation  $\mathbf{A}_e \approx [r_x \ r_y \ r_z]$  is adopted for the rotation matrix. Subsequently, the total kinetic energy of the element (with  $dm = \rho dV$ ) can be written as

$$T = \frac{1}{2} \int_V |\dot{\mathbf{r}}|^2 dm = \frac{1}{2} \int_V \dot{\mathbf{r}}^T \dot{\mathbf{r}} dm \quad (34)$$

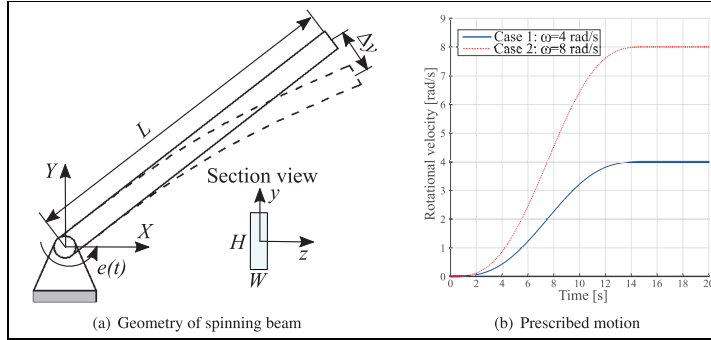


**Figure 7.** Sketch of spinning beam and its prescribed motion.

Substituting equation (33) into equation (34), the kinetic energy can be separated into three terms

$$\begin{aligned} T_1 &= \frac{1}{2} \int_V \mathbf{v}^T \mathbf{v} dm, \\ T_2 &= \Omega \int_V \mathbf{v}^T \mathbf{A}_e \mathbf{b} dm, \\ T_3 &= \frac{1}{2} \Omega^2 \int_V \mathbf{b}^T \mathbf{b} dm \end{aligned} \quad (35)$$

When considering the contributions of these energy terms to the equations of motion, it is apparent that the first term involves translational inertia and results in the mass matrix. The second term involves the gyroscopic effect and results in the gyroscopic matrix. The third and final term, a constant term that represents rotational inertia, does not contribute to the linearised equations of motion used in the eigenvalue analysis. Using the definitions  $\mathbf{v} = \mathbf{S}\dot{\mathbf{q}}$ ,  $\mathbf{r}_y = \mathbf{S}_y \mathbf{q}$  and  $\mathbf{r}_z = \mathbf{S}_z \mathbf{q}$ , the mass matrix and gyroscopic matrix can be written, correspondingly, as follows

$$\mathbf{M} = \int_V \mathbf{S}^T \mathbf{S} dm, \quad \mathbf{G} = 2 \int_V \mathbf{S}^T (y \mathbf{S}_z - z \mathbf{S}_y) dm \quad (36)$$

Taking damping into account, the resulting linearised system of equations of motion is of the form

$$\mathbf{M}\dot{\mathbf{q}} + (\Omega \mathbf{G} + \mathbf{C})\dot{\mathbf{q}} + \mathbf{K}\mathbf{q} = \mathbf{f}_{ext} \quad (37)$$

### Numerical examples

In this section, the two-node superelement and the three-node ANCF beam element are used in numerical simulation examples. The first example case is a spinning beam undergoing large rotations, while the second is a complex-shaped flexible rotor with an unbalanced

disc. In addition to computing the start-up response, which is done in both examples, the critical speeds of the system are analysed in the second example. Reference results for both cases are produced using the commercial FE software ANSYS.

### Spinning beam

In this section, the elements are applied to the simple spinning beam example from.<sup>26</sup> A flexible beam, as shown in Figure 7, is connected to the ground via a revolute joint at one end. The beam accelerates from rest to a constant angular velocity, with the motion described as

$$e(t) = \begin{cases} \frac{\omega}{T} \left[ \frac{1}{2} t^2 - \frac{T^2}{4\pi^2} \left( 1 - \cos\left(\frac{2\pi t}{T}\right) \right) \right], & 0 \leq t \leq T \\ \omega \left( t - \frac{1}{2} T \right), & t > T \end{cases} \quad (38)$$

where  $\omega$  is the final angular velocity and  $T = 15$  s is the spin-up time. As shown in Figure 7, two load cases with different constant angular velocities are considered, case 1 being  $\omega = 4$  rad/s and case 2 being  $\omega = 8$  rad/s. The cross-sectional dimensions and material properties are shown in Table 1. The flexible beam is discretised using four superelements built based on a linear FE model created using 300 SOLID186 elements in ANSYS. This FE model has 1935 nodes in total. A reference solution is provided using ANSYS with 20 BEAM188 elements, which is a nonlinear Timoshenko-based beam element. The total simulation time was 20 s, during which the transverse deformation of the free end was recorded.

The ANCF beam element model was computed in MATLAB using the solver 'radau5' (implicit Runge-Kutta method of order 5) with Newton's method for nonlinear solution. The relative and absolute tolerances



**Table 2.** Parameters of the rotor system.

Physical properties	Parameter	Symbol	Value
Physical properties	Density	$\rho$	7800 kg/m <sup>3</sup>
	Young's modulus	$E$	$2.1 \times 10^{11}$ Pa
	Poisson's ratio	$\nu$	0.3
	Gravity	$g$	9.81 m/s <sup>2</sup>
System geometry	Shaft length	$L$	6 m
	Shaft inner radius	$R_i$	0.045 m
	Shaft outer radius	$R_o$	0.05 m
	Disc radius	$R_d$	0.24 m
	Disc thickness	$t_d$	0.05 m
	Disc offset	$d$	0.05 m
System stiffness	Axial	$S$	313.4 MN
	Shearing	$K_{22}$	60.5 MN
	Shearing	$K_{33}$	60.5 MN
	Torsional	$H_{11}$	272.7 kN m <sup>2</sup>
	Bending	$H_{22}$	354.5 kN m <sup>2</sup>
	Bending	$H_{33}$	354.5 kN m <sup>2</sup>

to the ground by means of a revolte joint. At point T, the shaft is connected to the ground via a cylindrical joint. A rigid disc is attached to the shaft at its mid-span, and the centre of the disc is located above the shaft centre by distance  $d$ , thereby creating an unbalance in the system. The geometric parameters of the rotor system are shown in Table 2. First, the superelement and the ANCF beam element were used in modal analysis. The Campbell diagram, which shows the variation in the rotor's natural frequencies with respect to its rotating speed, was computed. After this phase, a transient simulation was performed. In the transient simulation, the motion of the revolte joint at point R was prescribed as follows

$$\Omega(t) = \begin{cases} A_1\omega \left(1 - \cos\left(\frac{\pi t}{T_1}\right)\right)/2, & 0 \leq t \leq T_1 \\ A_1\omega, & T_1 < t \leq T_2 \\ A_1\omega + (A_2 - A_1)\omega \left[1 - \cos\left(\frac{\pi(t - T_2)}{T_3 - T_2}\right)\right]/2, & T_2 < t \leq T_3 \\ A_2\omega, & t > T_3 \end{cases} \quad (39)$$

where  $A_1 = 0.8$ ,  $A_2 = 1.2$ ,  $T_1 = 0.5$  s,  $T_2 = 1$  s,  $T_3 = 1.25$  s and  $\omega = 60$  rad/s. This prescribed motion is further illustrated in Figure 9(b).

In rotor dynamics applications, the natural frequencies and excitation frequencies of the rotor-bearing system are often dependent on the rotational speed of the rotor. Usually, the natural frequencies are presented as a function of the rotation speed in the so-called Campbell diagram, from which it is possible to detect the critical rotating speeds of the system. To provide a reference solution, the rotor was modelled in ANSYS with a large number of SOLID186 elements, and a modal analysis was performed with gyroscopic effects included. During the analysis, the studied rotational

speed range was from 0 to 10,000 r/min. As it is difficult to exactly model the behaviour of idealised revolte and cylinder joints in a solid element model, all the DOFs on the boundary nodes were constrained in the case of element SOLID186.

First, the natural frequencies of the rotor system were computed using the linear superelement. The mass matrix, stiffness matrix and gyroscopic matrix from the original FE model were reduced by 12 constraint modes and 10 clamped interface normal modes. The Campbell diagram based on the linear superelement was compared with the corresponding original SOLID186 model as well as a traditional beam element model (BEAM188). A comparison between the linear superelement and SOLID186 is shown in Figure 10. It can be observed that the linear superelement agrees with the original model well.

According to the authors' knowledge, only linear theory was used when determining natural frequencies in previous publications. It is questionable whether linear theory is adequate for modal problems. It is also necessary to clarify how to use nonlinear theory in modal analysis and how nonlinear effects affect natural frequencies. For these purposes, the nonlinear superelement and the nonlinear ANCF beam element were used in the computation of the Campbell diagram of the rotor system.

When using the nonlinear superelement, the stiffness matrix was calculated with the finite difference method from the elastic force vector  $f_{in}$  in equation (22). Since the mass matrix and the velocity-related gyroscopic matrix were uncoupled from each other, the modal analysis of the superelement can be taken as a quadratic eigenvalue problem which is similar to linear modal analysis, while the matrices have a nonlinear relationship with the velocity vectors. The rotor was meshed with four nonlinear superelements as shown in

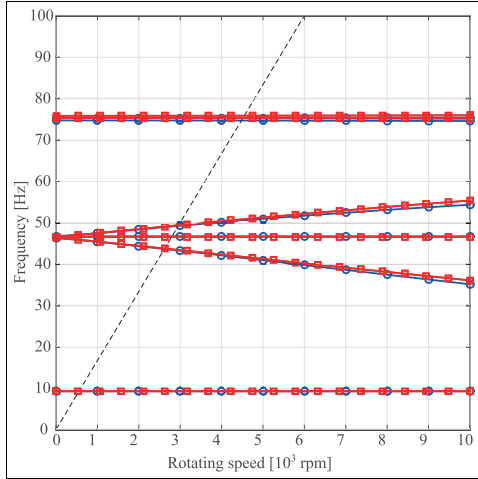


**Figure 10.** Campbell diagram based on SOLID186 and 1 linear superelement, clamped-clamped boundary condition (⊕ large number of SOLID186 elements, ⊕ 1 linear superelement with 10 normal modes). Dashed diagonal line represents spin frequency.

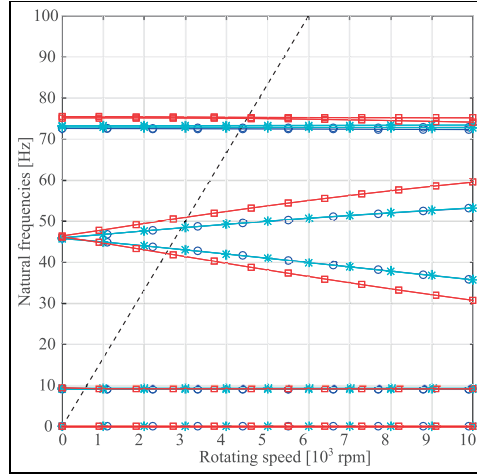


**Figure 12.** Campbell diagram based on nonlinear superelement and ANCF beam element in comparison with ANSYS BEAM188, revolute-cylinder joint boundary condition (⊕ 20 BEAM188 elements, \* 4 ANCF beam elements, ⊕ 4 nonlinear superelements). Dashed diagonal line represents spin frequency.

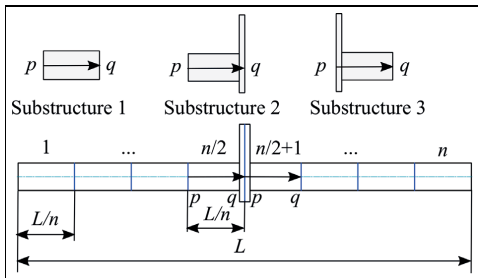


**Figure 11.** Discretisation of the rotor system.

Figure 11. The first and the fourth superelements are built based on substructure 1, while the second and third superelements are built based on substructures 2 and 3, respectively. The stiffness matrix for the ANCF beam element was also calculated using finite differences. Again, the elastic forces were integrated using a two-point Gauss quadrature lengthwise and three-point Lobatto quadratures laterally.

The Campbell diagrams based on the nonlinear superelement and ANCF beam element are shown in Figure 12. Figure 12 shows that the results based on eight ANCF beam elements are nearly identical to the ANSYS results, whereas the nonlinear superelement

does not agree with the reference solution well. The nonlinear superelement only gives the correct solutions for the first bending modes.

Second, the nonlinear superelement and the ANCF beam element were used to simulate the transient response of the system. The rotor shaft starts to rotate from static equilibrium under gravity load. The prescribed angular velocity described in equation (39) is applied and the transient response is analysed in the time range  $t = [0, 2.5]$  s. According to previously presented results, the first  $1 \times$  critical speed of the rotor is approximately 550.6 r/min or 57.66 rad/s. As the shaft accelerates, it passes the first critical speed of the system and the operation goes from sub-critical to super-critical. During the simulation, the displacement of the mid-span point was investigated. The rotor was meshed with four superelements and the velocity transformation matrix  $B2$  was used. The results presented in Bauchau et al.,<sup>29</sup> designated ‘Dymore’, were used as a reference.

The ANCF beam element model was computed in MATLAB using the solver ‘radau5’ (implicit Runge–Kutta method of order 5) with Newton’s method for nonlinear solution, as in the previous example. The relative and absolute tolerances were  $1e-4$  and  $1e-6$ , respectively. The elastic forces were integrated using a two-point Gauss quadrature lengthwise and three-point Lobatto quadratures laterally.

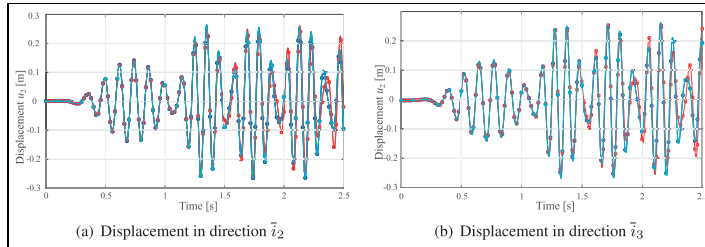


**Figure 13.** Displacement of mid-span point (— Dymore solution,  $\square$  4 nonlinear superelements with velocity transformation matrix  $B2$ ,  $\triangle$  8 ANCF beam elements).

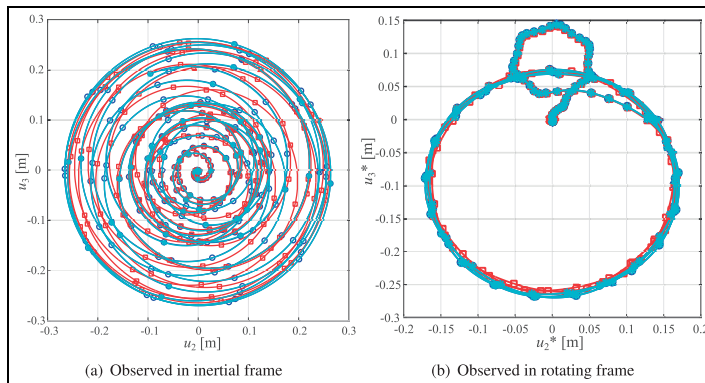


**Figure 14.** Trajectory of shaft's mid-span point (— Dymore solution,  $\square$  4 nonlinear superelements with velocity transformation matrix  $B2$ ,  $\triangle$  8 ANCF beam elements).

The displacements along the directions of  $\bar{i}_2$  and  $\bar{i}_3$  are presented in Figure 13, designated  $u_2$  and  $u_3$ , respectively. As can be seen, the results based on ANCF beam elements agree well with the reference solution. While the results based on the superelement also agree with the reference, they do not follow the reference as accurately as the ANCF beam results. The errors visible in the response given by the superelement solution increase as the rotating speed increases. Especially after  $t = 1.33$  s, when the rotating speed passes the first critical speed of the rotor system, the superelement results fail to follow the reference.

The trajectory of the mid-span point shows the rotor's dynamic response. The trajectory is presented in both the inertial frame  $[\bar{i}_1 \ \bar{i}_2 \ \bar{i}_3]$  and the rotating frame  $[\bar{e}_1 \ \bar{e}_2 \ \bar{e}_3]$  in Figure 14. It is apparent that the shaft becomes self-centring when it passes the critical speed. The ANCF beam element-based results are practically identical to the referenced Dymore results. Although the superelement is not as accurate as the

ANCF beam element, the difference remains within an acceptable range, and only four elements are enough for an acceptable solution. Therefore, computationally speaking, it seems that the superelement has an edge over the studied ANCF beam element.

The transient responses based on different velocity transformation matrices and different numbers of superelements are presented in Figure 15. When using two superelements, the solutions based on velocity transformations  $B1$  and  $B2$  give roughly the same results. However, these results differ considerably from the reference. When the number of superelements increases, the solutions based of  $B1$  and  $B2$  diverge. The formulation based on velocity transformation matrix  $B1$  fails to follow the reference, while the  $B2$  formulation seems to suffer from a convergence problem, as the displacement obtained with eight elements is larger than that obtained with four elements. This may be caused by the sharing of interface modes.

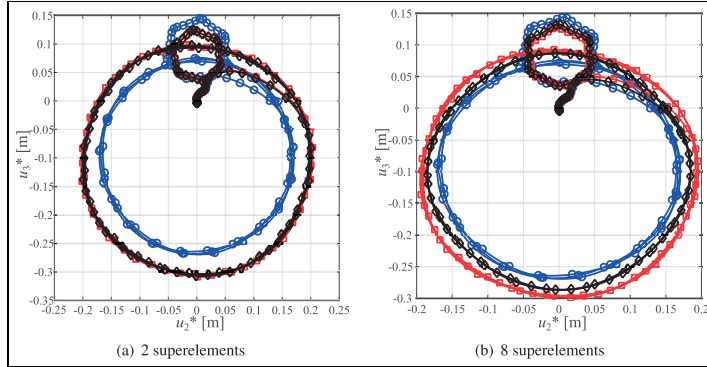


**Figure 15.** Trajectory of shaft's mid-span point, observed in rotating frame ( $\circ$  Dymore solution,<sup>9</sup>  $\square$  nonlinear superelement with velocity transformation matrix B1,  $\diamond$  nonlinear superelement with velocity transformation matrix B2).

## Conclusion

In this article, the superelement formulation as proposed by Boer et al.<sup>26</sup> and the quadratic beam element based on the ANCF as proposed by Nachbagaer et al.<sup>28</sup> were applied to the simulation of high-speed rotating structures. To this end, both element formulations were briefly reviewed by highlighting their distinctive features. The numerical results produced using both formulations were compared against those produced in the commercial FE software ANSYS and those available in literature.

The performance of the studied formulations was examined using two numerical examples in the field of rotating structures. The first test was a spinning beam example in which the transient response was examined using the ANCF-based beam elements and nonlinear superelements. The response was recorded for two rotational speeds. The results show acceptable agreement between all result sets at low speed. Nevertheless, the more pronounced rotational effects cause a divergence at the higher speed.

The second test was an unbalanced rotating shaft example, originally proposed by Bauchau et al.,<sup>29</sup> where both modal analysis and transient analysis were performed. Both nonlinear and linear superelements, in addition to the ANCF-based beam element, were used in this test. In this case, both modal and transient results show agreement between the ANSYS model and the ANCF beam model. However, the superelement results were more unpredictable. Although in certain cases the superelements were able to produce acceptable results with lower element numbers compared to the ANCF beam elements, the results based

on superelements do not agree with ANSYS results consistently in all cases. This is compounded by the observation that the number of superelements has a seemingly unpredictable effect on the results produced.

Two conclusions can be drawn from these outcomes. The first is that the ANCF-based element seems to produce results that agree with conventional beam elements with minor differences. This holds true even in cases where rotational effects are significant, as evidenced by the results. On the other hand, the second conclusion is that the superelement approach seems to be unable to do the same. Especially in the second example, the differences in results are quite significant.

The superelement was expected to improve computational efficiency by producing reliable solutions with just one element since the convergence problem was not discussed in past publications. Generally, when a distributed load is considered, more elements should be meshed to improve the accuracy of the simulation. Accordingly, as shown in the second example, four superelements appear to perform better than two. However, when the element number is increased to eight for more in-depth observation, the convergence problem emerges. One potential reason for this problem is the sharing of deformation at the interface surface of two connected elements. Another is the selection of the reference coordinate frame for calculating the velocity transformation matrix.

## Declaration of Conflicting Interests

The author(s) declared no potential conflicts of interest with respect to the research, authorship, and/or publication of this article.

### Funding

The author(s) disclosed receipt of the following financial support for the research, authorship, and/or publication of this article: The authors would like to thank the Academy of Finland (application no. 299033 for the funding of Academic Research Fellow) for supporting M.K.M.

### References

- Genta G and Silvagni M. On centrifugal softening in finite element method rotordynamics. *J Appl Mech* 2013; 81: 011001.
- Genta G, Feng C and Tonoli A. Dynamics behavior of rotating bladed discs: a finite element formulation for the study of second and higher order harmonics. *J Sound Vib* 2010; 329: 5289–5306.
- Geradin M and Kill N. A new approach to finite element modelling of flexible rotors. *Eng Computation* 1984; 1: 52–64.
- Nandi A and Neogy S. Modelling of rotors with three-dimensional solid finite elements. *J Strain Anal Eng* 2001; 36: 359–371.
- Rao JS. Finite element methods for rotor dynamics. *Hist Rot Mach Dyn* 2011; 20: 269–297.
- Simo JC and Vu-Quoc L. On the dynamics of flexible beams under large overall motions – the plane case: part I and II. *J Appl Mech* 1986; 53: 849–863.
- Berzeri M and Shabana AA. Development of simple models for the elastic forces in the absolute nodal coordinate formulation. *Journal of Sound and Vibration* 2000; 235: 539–565.
- Sonneville V, Cardona A and Bruls O. Geometrically exact beam finite element formulated on the special Euclidean group  $se(3)$ . *Comput Method Appl M* 2014; 268: 451–474.
- Bauchau OA, Han S, Mikkola A, et al. Experimental validation of flexible multibody dynamics beam formulations. *Multibody Syst Dyn* 2015; 34: 373–389.
- Chatelet E, D'Ambrosio F and Jacquet-Richardet G. Toward global modelling approaches for dynamic analyses of rotating assemblies of turbomachines. *J Sound Vib* 2005; 282: 163–178.
- Wagner MB, Younan A, Allaire P, et al. Model reduction methods for rotor dynamic analysis: a survey and review. *Int J Rot Mach* 2010; 2010: 273716 (17 pp.). DOI: 10.1155/2010/273716.
- Hurty WC. Dynamic analysis of structural systems using component modes. *AIAA J* 1965; 3: 678–685.
- Bampton MCC and Craig RR Jr. Coupling of substructures for dynamic analysis. *AIAA J* 1968; 6: 1313–1319.
- Shabana AA and Wehage RA. A coordinate reduction technique for dynamic analysis of spatial substructures with large angular rotations. *J Struct Mech* 1983; 11: 401–431.
- Agrawal OP and Shabana AA. Application of deformable-body mean axis to flexible multibody system dynamics. *Comput Method Appl M* 1986; 56: 217–245.
- Cardona A and Géradin M. *Flexible multibody dynamics: a finite element approach*. Chichester: John Wiley & Sons, 2001.
- Cardona A. Superelements modelling in flexible multibody dynamics. *Multibody Syst Dyn* 2000; 4: 245–266.
- Wu L and Tiso P. Nonlinear model order reduction for flexible multibody dynamics: a modal derivatives approach. *Multibody Syst Dyn* 2016; 36: 405–425.
- Géradin M and Rixen DJ. A 'nodeless' dual superelement formulation for structural and multibody dynamics application to reduction of contact problems. *Int J Numer Meth Eng* 2016; 106: 773–798.
- Cardona A and Géradin M. A beam finite element nonlinear theory with finite rotations. *Int J Numer Meth Eng* 1988; 26: 2403–2438.
- Cardona A and Géradin M. A superelement formulation for mechanism analysis. *Comput Method Appl M* 1992; 100: 1–29.
- Bauchau OA and Rodriguez J. Formulation of modal-based elements in nonlinear, flexible multibody dynamics. *Multibody Syst Dyn* 2003; 1: 161–180.
- Pechstein A, Reischl D and Gerstmayr J. A generalized component mode synthesis approach for flexible multibody systems with a constant mass matrix. *Asme J Comput Nonlin Dyn* 2013; 8: 773–798.
- Naets F and Desmet W. Super-element global modal parameterization for efficient inclusion of highly nonlinear components in multibody simulation. *Multibody Syst Dyn* 2014; 31: 3–25.
- Jonker JB and Meijaard JP. A geometrically non-linear formulation of a three-dimensional beam element for solving large deflection multibody system problems. *Int J Nonlin Mech* 2013; 53: 63–74.
- Boer SE, Aarts RGKM, Meijaard JP, et al. A nonlinear two-node superelement for use in flexible multibody systems. *Multibody Syst Dyn* 2014; 31: 405–431.
- Yakoub RY and Shabana AA. Three dimensional absolute nodal coordinate formulation for beam elements: implementation and applications. *J Mech Design* 2000; 123(4): 614–621.
- Nachbagauer K, Gruber P and Gerstmayr J. A 3D shear deformable finite element based on the absolute nodal coordinate formulation. *Multibody Dyn* 2013; 28: 77–96.
- Bauchau OA, Betsch P, Cardona A, et al. Validation of flexible multibody dynamics beam formulations using benchmark problems. *Multibody Syst Dyn* 2016; 37: 29–48.

## Publication V

Hurskainen, V.-V., Bozorgmehri, B., Matikainen, M.K., Mikkola, A.  
**Dynamic Analysis of High-Speed Rotating Shafts Using the  
Flexible Multibody Approach**

Reprinted with permission from  
*Proceedings of the ASME 2018 International Design Engineering Technical  
Conferences & Computers and Information in Engineering Conference*  
Paper No. DETC2018-86073, August 26-29, 2018, Quebec City, Canada  
© 2018, The American Society of Mechanical Engineers (ASME)



## ACTA UNIVERSITATIS LAPPEENRANTAENSIS

779. KORHONEN, ILKKA. Mobile sensor for measurements inside combustion chamber – preliminary study. 2017. Diss.
780. SIKIÖ, PÄIVI. Dynamical tree models for high Reynolds number turbulence applied in fluid-solid systems of 1D-space and time. 2017. Diss.
781. ROMANENKO, ALEKSEI. Study of inverter-induced bearing damage monitoring in variable-speed-driven motor systems. 2017. Diss.
782. SIIPIÄ, JENNI. The many faces of ambivalence in the decision-making process. 2017. Diss.
783. HAN, MEI. Hydrodynamics and mass transfer in airlift bioreactors; experimental and numerical simulation analysis. 2017. Diss.
784. ESCALANTE, JOHN BRUZZO. Dynamic simulation of cross-country skiing. 2017. Diss.
785. NOKKA, JARKKO. Energy efficiency analyses of hybrid non-road mobile machinery by real-time virtual prototyping. 2018. Diss.
786. VUORIO, ANNA. Opportunity-specific entrepreneurial intentions in sustainable entrepreneurship. 2018. Diss.
787. PULKKINEN, AKI. Towards a better understanding of activity and selectivity trends involving K and O adsorption on selected metal surfaces. 2017. Diss.
788. ZHAO, WENLONG. Reliability based research on design, analysis and control of the remote handling maintenance system for fusion reactor. 2018. Diss.
789. IAKOVLEVA, EVGENIA. Novel sorbents from low-cost materials for water treatment. 2018. Diss.
790. KEDZIORA, DAMIAN. Service offshoring industry: systems engineering approach to its transitional challenges. 2018. Diss.
791. WU, JING. Soft computing methods for performance improvement of EAMA robot in fusion reactor application. 2018. Diss.
792. VOSTATEK, PAVEL. Blood vessel segmentation in the analysis of retinal and diaphragm images. 2018. Diss.
793. AJO, PETRI. Hydroxyl radical behavior in water treatment with gas-phase pulsed corona discharge. 2018. Diss.
794. BANAEIANJAHROMI, NEGIN. On the role of enterprise architecture in enterprise integration. 2018. Diss.
795. HASHEELA-MUFETI, VICTORIA TULIVAYE. Empirical studies on the adoption and implementation of ERP in SMEs in developing countries. 2018. Diss.
796. JANHUNEN, SARI. Determinants of the local acceptability of wind power in Finland. 2018. Diss.
797. TEPLOV, ROMAN. A holistic approach to measuring open innovation: contribution to theory development. 2018. Diss.

798. ALBATS, EKATERINA. Facilitating university-industry collaboration with a multi-level stakeholder perspective. 2018. Diss.
799. TURA, NINA. Value creation for sustainability-oriented innovations: challenges and supporting methods. 2018. Diss.
800. TALIKKA, MARJA. Recognizing required changes to higher education engineering programs' information literacy education as a consequence of research problems becoming more complex. 2018. Diss.
801. MATTSSON, ALEKSI. Design of customer-end converter systems for low voltage DC distribution from a life cycle cost perspective. 2018. Diss.
802. JÄRVI, HENNA. Customer engagement, a friend or a foe? Investigating the relationship between customer engagement and value co-destruction. 2018. Diss.
803. DABROWSKA, JUSTYNA. Organizing for open innovation: adding the human element. 2018. Diss.
804. TIAINEN, JONNA. Losses in low-Reynolds-number centrifugal compressors. 2018. Diss.
805. GYASI, EMMANUEL AFRANE. On adaptive intelligent welding: Technique feasibility in weld quality assurance for advanced steels. 2018. Diss.
806. PROSKURINA, SVETLANA. International trade in biomass for energy production: The local and global context. 2018. Diss.
807. DABIRI, MOHAMMAD. The low-cycle fatigue of S960 MC direct-quenched high-strength steel. 2018. Diss.
808. KOSKELA, VIRPI. Tapping experiences of presence to connect people and organizational creativity. 2018. Diss.
809. HERALA, ANTTI. Benefits from Open Data: barriers to supply and demand of Open Data in private organizations. 2018. Diss.
810. KÄYHKÖ, JORMA. Erityisen tuen toimintaprosessien nykytila ja kehittäminen suomalaisessa oppisopimuskoulutuksessa. 2018. Diss.
811. HAJIKHANI, ARASH. Understanding and leveraging the social network services in innovation ecosystems. 2018. Diss.
812. SKRIKO, TUOMAS. Dependence of manufacturing parameters on the performance quality of welded joints made of direct quenched ultra-high-strength steel. 2018. Diss.
813. KARTTUNEN, ELINA. Management of technological resource dependencies in interorganizational networks. 2018. Diss.
814. CHILD, MICHAEL. Transition towards long-term sustainability of the Finnish energy system. 2018. Diss.
815. NUTAKOR, CHARLES. An experimental and theoretical investigation of power losses in planetary gearboxes. 2018. Diss.
816. KONSTI-LAAKSO, SUVI. Co-creation, brokering and innovation networks: A model for innovating with users. 2018. Diss.



Acta Universitatis  
Lappeenrantaensis  
817



ISBN 978-952-335-277-3

ISBN 978-952-335-278-0 (PDF)

ISSN-L 1456-4491

ISSN 1456-4491

Lappeenranta 2018

---